ENHANCED RADIATION TOLERANCE OF CERAMIC THIN FILMS BY NANO-STRUCTURAL DESIGN

A Dissertation

by

LIANG JIAO

Submitted to the Office of Graduate and Professional Studies of
Texas A&M University
in partial fulfillment of the requirements for the degree of

DOCTOR OF PHILOSOPHY

Chair of Committee,	Haiyan Wang
Committee Members,	Lin Shao
	Tahir Cagin
	Xinghang Zhang
Head of Department,	Ibrahim Karaman

May 2015

Major Subject: Materials Science and Engineering

ABSTRACT

Thin films techniques are widely used in microelectronic devices, optical coatings, batteries and solar cells, which would be applied under harsh environment spanning from outer space to nuclear plant where defects are easily generated, accumulate and eventually degrade the materials properties. Oxide and nitride thin films are widely used and mostly studied in such applications. Moreover, MgO and ZrN have been considered as promising candidates of Inert Matrix materials to reduce hazardous nuclear waste. Therefore, studies on the defects development, and more importantly, the enhanced damage tolerance by microstructural design are of great importance. However, only limited study has been conducted up-to-date.

In this dissertation, interface mitigation effects on radiation damage have been explored in TiN/MgO epitaxial thin films. After ion implantation with He^{+} ions, no hardness variation is observed in the epitaxial multilayers, and high resolution TEM indicates no obvious ion damage in the MgO layers within the epitaxial multilayer samples. However, single layer MgO film shows a significant hardness increase of ~20% and high density point defect clusters are clearly identified. The results suggest that, in this system, epitaxial interfaces could act as effective point defect sinks in reducing the defect density and suppressing the ion-implantation induced hardening in MgO, and thus are responsible for the enhanced radiation tolerance properties.

The grain size dependent response in nanocrystalline (nc) ZrN under high dose heavy ion implantation has been studied with Fe^{2+} ion, and it is found that the ZrN film

with the average grain size of 9 nm shows prominently self-healing effects as evidenced by suppressed grain growth, alleviated radiation softening, as well as reduced variation in electrical resistivity. In contrast, ZrN with the larger average grain size of 31 nm shows prominent softening and resistivity increase after implantation, attributed to the high density of vacancy like defect clusters formed inside the grains. The distinct implantation effects on microstructure, residual stress, grain growth, and electric resistivity of thin films with different grain sizes were discussed, and the influence of grain boundaries on enhanced tolerance to implantation damage in nc-ZrN is demonstrated.

In order to further study the real-time response of the designed microstructures, and their kinetic interactions with defects. *In-situ* irradiation on MgO/ZrN multilayer systems with non-epitaxial interfaces as well as grain boundaries has been conducted, which shows clearly the cyclic process of the defects removal by high angle grain boundaries and effectively absorbed by interfaces. Another *In-situ* study on the MgO/TiN epitaxial films has demonstrated that the implantation induced defects migrate to the interfaces, and annihilate there, that improve the MgO tolerance against amorphization. The comparison has shown that the non-epitaxial interfaces are more effective in absorbing defects manifested by the higher mobility of defects migration towards the MgO/ZrN interfaces. The research findings could provide guidance for microstructural design of functional ceramic thin films for advanced technological applications under extreme conditions from outer space exploration to nuclear energy generation.

DEDICATION

The dissertation is dedicated to my family.

ACKNOWLEDGEMENTS

I would like to thank my committee chair, Dr. Haiyan Wang, her great help lead me through many difficulties in the research and personal life during my graduate study. And I would like to express my genuine gratitude to Dr. Xinghang Zhang. His great guidance deepened my understanding of research, and significantly improved my research quality. Moreover, I thank for my committee member Dr. Lin Shao, for his collaboration contributed a great amount of this work. And my thanks go to Dr. Tahir Cagin, for his guidance and support throughout this research.

Thanks also go to my friends and colleagues, and the department faculty and staff for making my time at Texas A&M University a great experience. I also want to extend my gratitude to the National Science Foundation (NSF-0846504). The Idaho National Laboratory subcontract, and the Center for Integrated Nanotechnologies (CINT) at Los Alamos National Laboratory, Office of Basic Energy Sciences user facility funded by the U.S. Department of Energy (CINT user project-2009A006). Access to the microscopy and imaging center (MIC) at Texas A&M University is also acknowledged. Thanks to Argonne National Lab for the great opportunity of *in-situ* irradiation experiment conducted there.

Finally, thanks to my parents for their unconditional love and to my grandmother for her kindness and influence over my life.

TABLE OF CONTENTS

LIST OF FIGURES

Page

LIST OF TABLES

Page

CHAPTER I

INTRODUCTION AND LITERATURE REVIEW

1.1 Background of the Nuclear Energy and Current Fuel Cycle

Energy is vital to human life, and especially important in economy recovery and growth nowadays. Electricity is one of the most common energy forms in modern human history. The long term projection of electricity consumption will be 5 fold as it is now at year of 2050. Up to date, the energy generated globally is still heavily depending on fossil fuels. It is known, traditional energy sources like coal and oil are not renewable, and the CO_2 associated with the combustion of them causes the severe climate change. Not to mention the pollution caused by combustion of fossil fuels in the rapidly developing countries such as China and India. Seeking new alternative energy sources, more importantly for those clean, safe and economic energy sources are of great interests of every country, in which many means should play a role, such as wind, hydropower, solar energy, and nuclear energy. However, they are way off from meeting our large and rapidly increasing energy demand. Among them, nuclear energy catches most of the attention, and has all the technology required for large scale application. Nuclear energy is greenhouse gases free, and a relatively clean energy form, as well as capable of generate large amount of energy. The current operating nuclear plants in US are only a handful of 104, but produces around 20% of the electricity nationwide. However, safety

issues such as what happened at Three Mile Island and Fukushima, spent fuel disposal and the proliferation problem have raised concerns significantly worldwide.

Spent nuclear fuels are highly toxic, containing many radioactive isotopes with long half-lives. The current fuel cycle employed in the U.S. is incomplete, called the once-through nuclear fuel cycle, which is utilized in the light water reactors (LWR). Fig. 1 schematically shows the fuel cycle. There is a complete front end, where uranium is mined, and U-235 is enriched, and fuel is assembled. After years of service in the plant, where energy is generated, the fuel becomes spent fuel, which requires a reliable storage solution. So far, there is only the high level waste (HLW) management capability in America as the back end of the current fuel cycle.

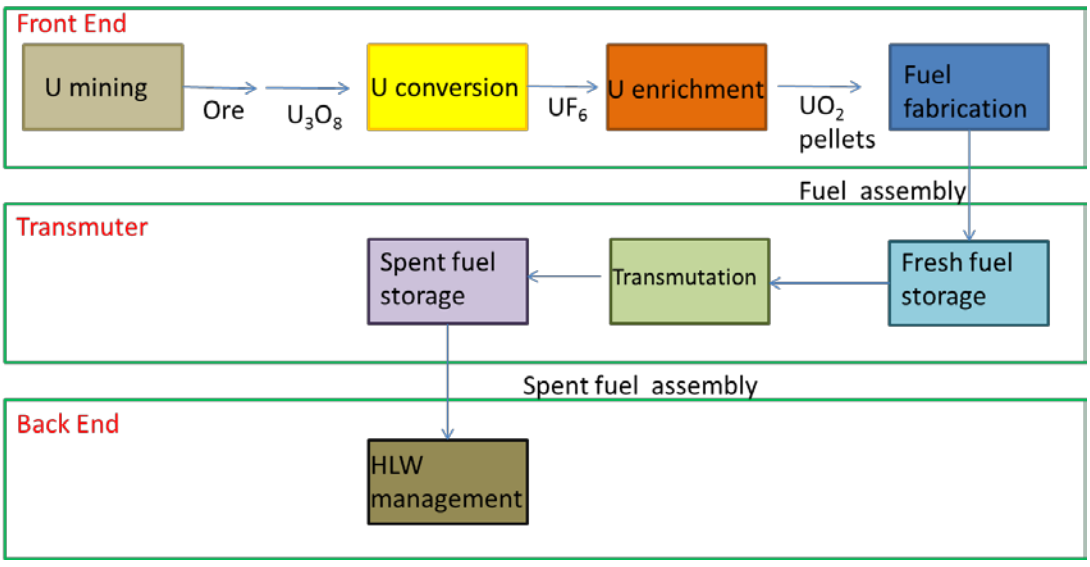

Figure 1 The once-through LWR nuclear fuel cycle

A reliable method of long-term storage of nuclear waste is nowhere close to practical use. Up to date, in America, all the nuclear wastes, over 65,000 tons, are stored

temporarily on site, and the building of permanent underground repository is nowhere close. The reliability of either the temporary storage or the ultimate disposal remains problematic, especially under the attack of natural disaster or terrorists. The proliferation issue of the weapon grade materials generated in the current nuclear fuel form could be another potential hazard. There are two types of conventional fuel forms that are most widely adopted: the low enriched uranium (LEU) and the mixed uranium-plutonium oxide (MOX) fuels. U-238 is used as the diluent in both of the conventional fuels where a critical density (3% ~ 5%) of the fissile part (U-235) allowing the sustainable and controllable nuclear reaction is embedded. However, U-238 could capture one neutron, and then undergoes two beta decay, becomes Pu-239, which is the most common plutonium isotope formed in nuclear plants. Take Pu-239 as an example, the half-life is ~24000 years, the toxicity and long lasting radioactivity raise up the safety concerns on the spent fuel. Although over half of all the plutonium created is burnt in the fuel, there is still over 1% of the spent nuclear fuel are the different isotopes of plutonium. Weapon grade plutonium could be extracted from the spent fuel through reprocessing, and therefore proliferation issue could be serious when the piling up of spent fuel falls into the wrong hands. Therefore, a new fuel form is needed to close the current once-through fuel cycle, from which the spent fuel can be processed and made into new fuel for re-burning to address the piling up of waste, proliferation issue as well as generate more energy.

1.2 Proposed Solutions (New Fuel Forms) and Materials Needed

1.2.1 The Concept of Inert Matrix Fuel (IMF)

Instead of using U-238, some neutron transparent materials are proposed to be the inert matrix materials. The employment of neutron transparent materials as matrix eliminates the plutonium breeding problem associated with the neutron capture of U-238. The fissile phase is either dissolved in the matrix or incorporated as macroscopic or microscopic inclusions. And with reprocessing of the current spent fuel, the transuranics, especially plutonium and the long time radioactive minor actinides such as americium, curium and neptunium will be extracted from the spent fuel, and made into new fuels for future burning on site, instead of bury those nuclear wastes. During the re-burning, the transuranics could decay into less hazardous elements, besides, more energy will be generated with less fissile materials and so as less and even no waste produced. This concept is called the Inert Matrix Fuel (IMF), which has been proposed and studied widely for the past two decades to solve the problems associated with the current fuel form.

1.2.2 Materials Selection

The searching and studying for suitable matrix materials have been widely conducted since the sixties of last century, and such exploration has resumed and

ramping up this century. Many materials are of great interest for scientists, they all share some common properties that meet the criteria of IMF technology:

(a) Low neutron absorption cross section. In other words, the materials are required to be neutron transparent. According to the design, the spent fuel is exposed to neutron irradiation before disposal to transmute the high radiotoxic elements to less harmful one. Moreover, the neutron transparency increases the fission efficiency.

(b) Compatibility with reactor materials, such as with the fissile phase, non-reactivity with the cladding materials and structural materials, and low-solubility with the coolant.

(c) Acceptable thermal conductivity, so that no significant thermal stress is built up inside the fuel.

(d) High melting point, good mechanical properties and high density.

(e) Outstanding radiation tolerance to achieve high burnup and safe operation.

(f) Satisfying the requirements of reprocessing, such as dissolvable in certain chemical, and the fissile phase could be extracted.

Several groups of materials are particularly promising as IMF candidates, including oxides, nitrides, carbides and some metal materials. However, none of them fits perfectly with all the criteria while they qualify some. For example, oxides are the most studied and widely understood one for decades, and most reactor knowledge is based on oxide based fuel, a lot of researches and experience were gained on UO_2, MOX and even thorium oxides for the next generation nuclear reactor. Oxide candidates

provide the possibility of them being applied in the current operating plants. However, most oxides are thermally insulating, that results in poor efficiency and temperature building up in the fuel core. The plutonium segregation to the periphery and pore migration to the fuel core are also resulted from the thermal gradient built up. Nitrides are also of great interest to researcher because of their hardness, optical properties, thermally and electrical conductivity [1]. And many transition metal nitrides are refractory, inert to most chemical environments, and compatible to transuranic nitrides. The solid solution of transuranic-nitrides, including PuN, NpN, AmN, CmN, etc. with ZrN is considered as one of the primary fuel type candidates for the Advanced Accelerator Assisted (AAA) system. Moreover reprocessing can be achieved by using nitric acid. However, the manufacturing is difficult since the high melting points of the nitrides. Metals have good thermal conductivity, but very low melting points, that raises safety concern in plants when accidents occur. And the compatibility with sodium or water further questions the feasibility of metal matrix.

The inert matrix materials must survive the environment of high temperature, and constantly bombarded by neutrons and other fissile products for years. In the oxides and nitrides family, MgO and ZrN poses multi-fold advantages, and they are considered as most promising candidates as inert matrix materials from the oxides and nitrides family respectively, and therefore chosen in this study. Besides, TiN is also used to synthesize different microstructures. Some carbides and metal studies in this field would be reviewed in the following sections as well.

1.3 Background of Radiation Damage in Materials

1.3.1 Fission Products

The fission reaction of a U-235 atom is triggered by the absorption of a neutron, and two fragments as well as three neutrons are produced from the split of the original U-235 atom. Some of the released neutrons are then captured by U-238 as discussed in section 1.1, or by other elements, while others can trigger subsequent fission reactions and produce more neutrons. The multiplication of neutrons, and therefore the continued fission reaction is called the chain reaction.

The fission products include neutron, α and β particles as well as the energetic fission products from fissile element. Both α and β particles are produced by their respective decay cycles: β decay produces electrons or positrons from neutron transferring to proton or vice versa in the atomic nucleus with typical kinetic energy around 1MeV, but can range from a few keV to several tens of MeV, with speeds up close to light speed, however with the low mass of electrons, the momentum of beta particles is small. While α decay produces energetic helium nuclei with energy of about 6 MeV. Neutrons are released usually with a kinetic energy of several MeV, and categorized as fast neutrons, which have low cross sections to induce fissions. The kinetic energy needs to be lowered below 1 MeV, and the neutrons become thermal neutrons to cause fission reactions. Scattering of a neutron may be elastic or inelastic. Elastic scattering is scattering in which no kinetic energy is lost from collision system,

while the momentum is conserved as well. Inelastic scattering transfers some energy and leaves the lattice atom in an excited state, or induces chemical reaction. The excited atom lowers itself to the ground state by emitting sub-particles and photons such as x-ray and gamma ray. Elastic scattering becomes gradually predominant the speed of neutrons is lowered, since the scattering cross-section of nuclei increases with slowing of neutrons. This interaction is simplified as purely ballistic process and the neutron energy is reduced by the subsequent collisions until it stops. Light atoms, such as H, O and C are used as moderators due to their close mass to neutron. They can slow the neutron energy efficiently so that the energy eventually is near equilibrium with the nuclei of the fuel. These moderated, or thermalized, neutrons have a much higher cross section with U-235 to produce fission events [2].

Incredible amount of energy is produced by the fission reaction of the fissile elements. Much of the energy is released in the form of kinetic energy via the expulsion of neutrons and fission products. The kinetic energy of fission products are in the range of approximately 70 to 100 MeV each. The sum of mass and energy of fission products equals to the original fissile element. In the case of UO_2 fuel in a typical LWR, the spectrum of fission products ranges from Ge to Dy in the lanthanum series, and the distribution is similar of transuranics fission products [2].

1.3.2 Fission Product Interaction with Matter

The fission products then move through the matter at high velocity, and cause various type of interactions. The interactions of neutron with matter typically indicating the neutron interacting with nuclease owing to the negligible size of orbiting electrons compared to the nuclease. The interactions include scattering (elastic scattering, inelastic scattering) and absorption. The scattering was discussed previously, and the absorption of neutrons by the nuclease can occur via electric magnetic process where photos are emitted, or via charged particle emission as well as neutral process that another neutron is later emitted. The final absorption of neutron to the nuclease can be fission, where the original nuclease is broke into daughter products as discussed before. The Gamma interaction with matter includes photoelectric effects, Compton scattering, and Pair production. The electron interactions with matter include Bremmstrahlung (braking) radiation, and Cherenkov radiation. And the interactions between alpha particle and fission fragment with matter include radiation damage and electronic excitation. The radiation damage from the fission products is the interest of this research.

1.3.3 Energy Loss and Stopping Power

As an ion is moving through the lattice, it encounters lattice atoms on their lattice sites, and loses energy from the interaction with them, via which process, the implanting ion finally stops. There are two stopping mechanisms: nuclear stopping (S_n) and

electronic stopping (S_e). The stopping of the projectile species are the results of the summation of these two mechanisms. The nuclear stopping is from the interaction of implant ions with nuclei, causing the scattering of ions, and displacement of nuclei. And the electronic stopping is through the interaction of the implant ions with the electrons of the lattice atom. The ion energy is reduced, and transferred to the excitation of electrons, or stripping the electrons off the lattice atom. The Pauli exclusion principle forbids the electrons share the same quantum state, and therefore, the projectile ions' electrons excite the atomic electrons to jump to a higher state. The jump back of the excited electrons to the ground state will emit energy in the form of either photons or phonons, and this process is an inelastic collision event. This effect becomes less efficient, as the ion further slows down.. The target atoms could either be displaced or ionized that causing rapid repulsion, the "fission tracks" in swift ion irradiations are the evidence of these strong destructive forces produced during electronic interaction. At low energy region, the nuclear stopping increases with the kinetic energy of the implant ions, while at high kinetic energy region, due to the insufficient time for energy exchange with nuclei, the nuclear stopping drops. Heavier elements have higher nuclear stopping power than lighter elements. On the other hand, the electron stopping is proportional with the ion velocity, and it's described as:

$$S_e(E) = k_e\sqrt{E}$$

Where E is the energy of the ion at a certain point on its trajectory, and k_e is a coefficient which is weakly related to the target atomic number and mass. For example, the k_e for Si is 10^7 $(eV)^{1/2}$/cm, and GaAs has a k_e around three times greater [3]. For

example, implantations of As^+, P^+, B^+ into Si, have different dominant stopping in the energy range 0 to 1 MeV. The electron stopping is dominant for B^+ implantation in this range, due to the small atomic number, however for As^+ implantation, the nuclear stopping is primary for energy smaller than 700 keV, and electron stopping surpasses the nuclear stopping when energy is greater than 700 keV. And for P^+ implantation, which has the mediate atomic number, the crossover of nuclear stopping and electronic stopping is at 130 keV, below which nuclear stopping is greater than electronic stopping [4]. When the projectile velocity is greater than that of the average electrons in the lattice orbitals, the implant ions are stripped of all of the electrons and become highly positively charged. The stopping in this region is called the Bethe-Bloch stopping. The positively charged ions perturb the electrons around the trajectory and lose energy. As the velocity slows, the time spent near these electrons increases, and thus stopping increases as shown in the Fig. 2:

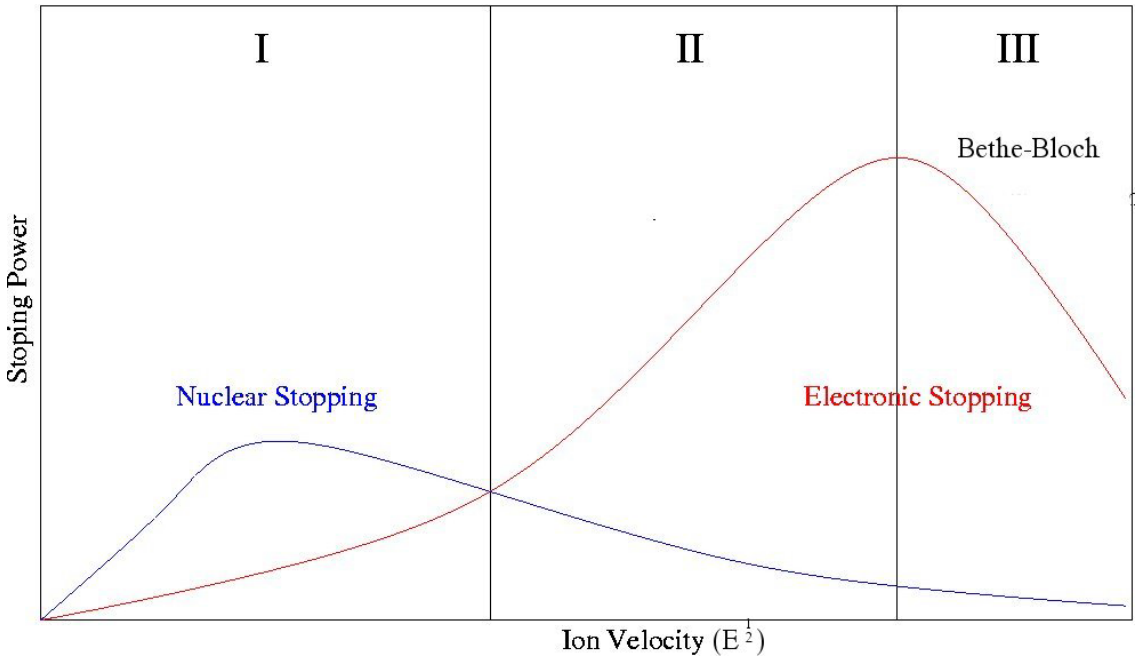

Figure 2 Stopping power of an implant ion in the target lattice. Area I is nuclear stopping dominant region, and area II is the region dominated by electronic stopping, area III is the Bethe-Bloch region [2].

1.3.4 Displacement Threshold Energy (E_d)

As the energetic ions moving through the lattice, they lose energy by exciting electrons, elastic collisions, or by inelastic collisions. Displacement of an atom from its lattice site requires a minimum energy transferred from the collision, which is the displacement energy or displacement threshold energy, E_d. If the energy transferred to the struck atom is smaller than E_d, the struck atom will only vibrate around its equilibrium position instead of being displaced, and pass the vibration to the surrounding lattice via the interaction between their potential fields. The energy transferred in this scenario would dissipate in the form of heat. The struck atom acquiring sufficient energy

from the collision overcome this potential and displace the surrounding lattice, in order to move through the lattice, and ends up in a site which is sufficiently far enough that the displaced atom won't move to its original site immediately. In crystalline materials, the potential is not uniform along all the lattice directions. Different lattice directions have different densities of atoms and as such have different E_d. Along the directions of high symmetry, the displacement energy is relative low. The average displacement energy is generally reported due to the random direction of the recoils, which is very commonly considered to be 20~ 25 eV for metals estimated from the sublimation energy for most metals, which is about 5 eV. Considering about the twice more bonds broke in removing an atom in the interior than from the surface, plus the amount of energy needed for the atom reside in an interstitial site, and no sufficient time for the neighboring lattice relaxation, 4 to 5 times of this sublimation energy is usually used as the displacement energy in metals. The E_d is estimated about 40 eV for ionic ceramics [2]. If the interaction potential between lattice atoms is known, the displacement energy along a certain direction can be determined more accurately by summing the potential energy along the struck atom trajectory When the potential energy reaches a maximum, the corresponding site is called a saddle point, and the displacement energy is determined by the difference of the displaced atom at this saddle point with its original lattice equilibrium position [5]..

In a simplified model, when the energy transferred exceeds E_d, the probability of displacement is 1, otherwise it's 0. This step function is only strictly valid in an amorphous material at 0 K. Because of the influence of thermal energy of the lattice, and

the crystallinity on displacement energy, this function step is blurred with a certain width. The next step is to find the amount of displacements as a function of energy transferred, given this displacement probability. And therefore, a model is developed by Kinchin and Pease [6].

1.3.5 Kinchin-Pease Approximation

In order to obtain a simple method to calculate the average numbers of displacements in a solid material initiated by a primary knock-on atom (PKA) with a certain amount of energy T, several assumptions were made by Kinchin and Pease:

1. Only the elastic collisions between atoms were considered in creation of the cascade.

2. The displacement probability is 1 if $T > E_d$.

3. No energy passes to the lattice in the collision, energy is conserved among the PKA and the recoil.

4. Energy loss of electronic stopping is set with a cut-off energy E_c, below which the electronic stopping is neglected, and only atomic collisions take place and cause displacements. No additional displacements occur for energy greater than E_c, until the energy is reduced to this cut-off energy by electronic stopping.

5. Hard-sphere model is used for the energy loss cross-section.

6. The crystal structure of the target material is not considered, that the arrangement of atoms is assumed as random.

In the hard-sphere model for collisions, electronic stopping is ignored, and the same mass of the atoms is used. This model satisfactorily works for slow ions with close masses. The concept requires that a certain amount of energy (displacement threshold energy) must be obtained by the target atom to be displaced, and the projectile has just enough energy to be a replacement as illustrated as the stage in Fig. 3. Twice as this energy is required for the displacement a second lattice atom, and therefore a linear relation with a slope of $(\frac{1}{2E_d})$ is obtained. The Kinchin-Pease model tends to overestimate the number of vacancies induced by recoils, but provides a fast estimation of the extent of damage expected from a certain amount of energetic particles [2]. This method is used in the SRIM[7] calculation as the quick method, and is widely accepted in the radiation field as an estimation of the displacement per atom (dpa).

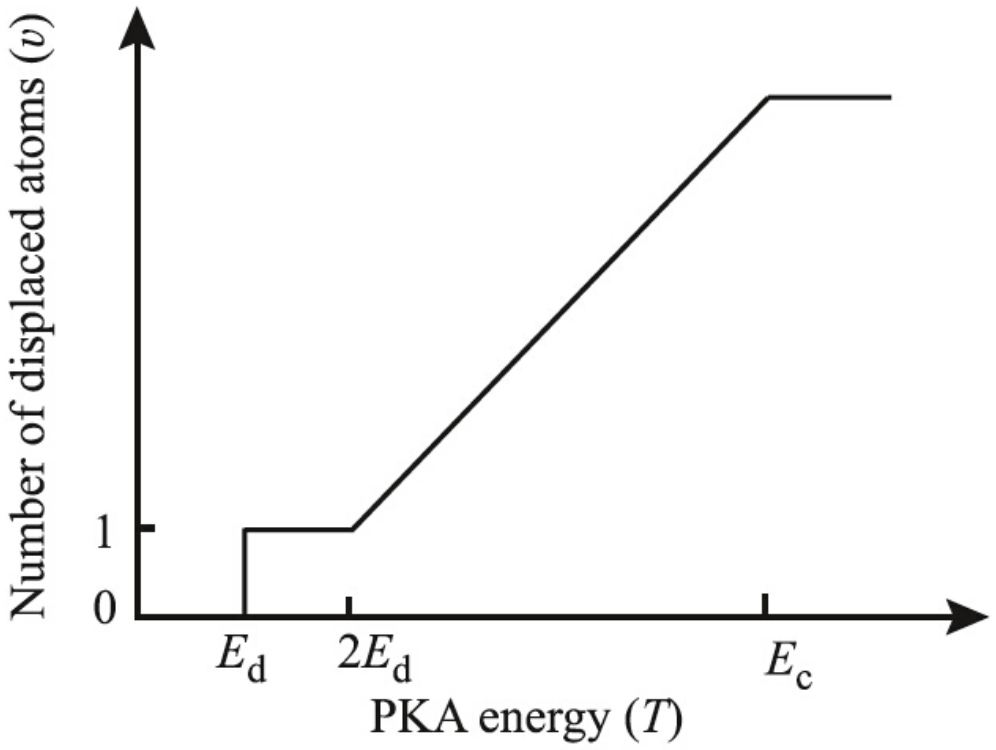

Figure 3 Kinchin-Pease model for the number of displacements as a function of PKA energy beyond E_d [5].

1.3.6 Defects Introduced by Irradiation

Nuclear collisions become the primary stopping as the implant species slowed down. Momentum and kinetic energy are conserved, and the displaced lattice atom becomes another projectile until all projectiles in the cascade no longer have the energy required to displace another atom and rest in the lattice. The Frenkel type defect consists of a vacancy, and the displaced atom as an interstitial, which is the most common initial defect generated under irradiation. Most of the Frenkel pairs immediately recombine via short diffusion path, the rest with large separation become isolated point defects, which

may further grow into clusters with same type of point defects. In ceramics, at room temperature, vacancies are considered immobile, while interstitials is mobile. With increasing temperature, the mobility of vacancies increases, and thus the recombination rate is increased as well. Therefore under annealing, vacancies can move and annihilate either with opposite type defects or on a free surface. The left vacancies may also agglomerate into voids, and if gas species trapped inside the voids, bubbles formation occurs. The difference between a void and a bubble is defined by pressure, a void surface has negative pressure, while the bubble surface has a positive pressure as a result of gas species trapped inside. Moreover, they could also cluster into vacancy loops, although is much less likely, due to the less mobility.

On the other hand, interstitials can grow into dislocation loops more readily, which growth is limited by the stacking-fault energy (SFE) since the lattice sequence is interrupted, and also limited by the dislocation line energy which is related to the strain created around the loops. The movement of dislocation loops is usually very hard. Since the number of the vacancies roughly equals to the number of interstitials (given the number of substitutes is small), once the interstitial dislocation loops are formed, there is a lower drive for the corresponding vacancies to recombine with interstitials. These extra vacancies create vacancy bias, which increases the system energy. As a result, there is a tendency for these extra vacancies to reduce the total system energy by clustering into voids, bubbles, or vacancy loops. In this case, the diffusion barrier or energy required by vacancies to become mobile is relatively lower.

Besides the dislocation, voids and bubble formation, chemistry reaction also takes place under irradiation. Chemically active elements such as I, Nd, Zr, Mo, Pd, and Cs are produced in large quantity [2, 8], and these elements will react profoundly with the surrounding metals or with each other. For example, cesium and iodine are readily to form CsI gas which has corrosive effects on the cladding materials. Proton and α particle are essentially the nucleus of hydrogen and helium, and they pose a deterioration risk to the cladding, as these gas species would result in swelling and embrittlement. On the other hand, xenon, krypton and helium are also common fission products which are in large quantity and deposit large energy into the surrounding materials. However, the noble gases exclude the complex chemical reactions and therefore widely used in displacement damage studies. Kr and He are used for most of the irradiation conducted in this study.

Helium is the most common product of decay and inelastic neutron capture. Helium is produced in large quantity over a very long period, since even if the fission reaction stops, the decay of other radioactive elements continues. The major problems concerning the large amount of helium are swelling. Due to the high temperature in nuclear fuel and the small size, helium diffuses rapidly, which further promote the voids formation and swelling. When considering fuel storage and advanced fuel forms which could achieve very high burnups, the estimated amount of helium produced could be more than five times than in the traditional UO_2 fuel from a LWR. Although the helium produced in the decay has an energy that is much less than the fission products, but the damage (displacement damage and accumulation of helium) could accumulate

significantly over time. The accumulation of helium both in the fuel and in the cladding materials results in bubble formation, and swelling, and as helium accumulates at the grain boundaries of the cladding materials, embrittlement could occur. The importance of study xenon and krypton is because of the heavy atomic mass and the high kinetic energy that causes much tremendous displacement damage. So that, helium is usually used in research for study the bubble formation and behavior, and the displacement damage which related to defects accumulation, stress and crystal structure variation, and physical property degradation is often studies with the krypton irradiation.

1.4 Background on the Key Materials Discussed in the Thesis

1.4.1 MgO and Its Related Radiation Mechanisms Studies

MgO has been widely studies for decades both experimentally and computationally. First of all, MgO is relative simple for study compared to more complex oxides. And it's a well understood classic engineering ceramic. Due to its physicochemical properties, MgO has been of interest in a wide range of applications including protective coating in plasma display panels, catalysis, fuel cells and tunable broadband laser [9]. MgO doping has been reported to inhibit grain growth in ceramics and improve their fracture toughness effectively [10]. MgO thin film can grow epitaxially on multiple substrates including on Ge and GaAs, and on TiN buffer layer, which also make it interesting in many devices applications [11]. For example, MaO thin

film is also used as an oxide barrier in spin-tunneling devices, owing to the crystalline structure. The spin polarization of about 85% has been reported with MgO [12] compared to the 40–60% of the commonly used amorphous Al_2O_3 [13], and MgO is thermally more stable than alumina. The reported value of tunnel magnetoresistance, 600 % at room temperature and 1100 % at 4.2 K [14], is also considerably higher for MgO than that of Al_2O_3 (70% at room temperature [15]). Moreover, MgO also received attention as a material for immobilization and long-term nuclear waste storage, transmutation of high radioactive actinides, inert matrix materials for Advanced Fuel Cycle Initiative (AFCI) and proposed as insulators for fusion reactor diagnostics due to its neutron transparency, high thermal conductivity compared to other oxide materials, high resistance to high-energy particle irradiation [16-19]. The outstanding properties of MgO might also make it interesting for fusion reactor applications in the future.

Compatibility

The compatibility of MgO with fissile materials and actinides is well studied and the results are satisfactory, which provides the application for MgO as a matrix material candidate. An early experimental work [20] has shown that the PuO_2-MgO phase diagram is a simple eutectic one with the eutectic point at around 2260 ^oC, with 40 mol % of PuO_2 in the oxygen atmosphere. Phase diagrams were calculated by Zhang et al. in Pu-Mg-O and Am-Mg-O systems [21]. PuO_2-MgO presents in an oxidizing atmosphere,

while in dry inert atmosphere PuO_2 was reduced to $PuO_{1.6}$. The PuO_2-MgO system has a eutectic point at 40 to 60 mol % ratio at temperature 2503 K, whereas the $PuO_{1.6}$-MgO system has a eutectic point at 2341 K with a mole ratio of 54 – 57 % of $PuO_{1.6}$. In the calculated MgO- $PuO_{1.6}$-PuO_2 system, the author suggested the temperature should be below 2450 K or the ratio between $PuO_{1.6}$ and PuO_2 should be lower than 50% to avoid the presence of liquid phase. The calculated Am-Mg-O system has a low eutectic point at 1930 K at a partial oxygen pressure below 1 bar, and in order to increase the eutectic point, high partial oxygen is required, which would increases the corrosion on cladding. The author suggested MgO is not a good inert matrix material for transmutation of Am. The calculations of MgO-UO_2 were reported to have simple eutectic phase diagram [22, 23]. Epstein and Howland suggested the eutectic point is at 59 mol % of UO_2 at 2159 ^oC, and Budnikov reported the eutectic point is about 2280 ^oC. However, experimental data is scarce to support the calculated results, and the calculated data varied from method to method.

Moreover, there is no indication of chemical interaction between zircaloy and MgO was reported [24]. In inert atmosphere, MgO is reported inert in contact with Zr, and Nb, at 1400 ^oC and 1600 ^oC respectively. At 1800 ^oC, minor reaction is observed with products of ZrO_2 and Nb_2O_5 respectively, and it is attributed to the surface dislocation and penetration [25]. Tolksdorf [26] suggested the presence of Mg in Zr may be beneficial, that the oxidized Zr with 1% MgO alloy shows a better resistance to corrosion and hydriding than Zircaloy-2.

There is a concern with the interaction between MgO and high pressure, high temperature water. $Mg(OH)_2$ is thermodynamically favorable than MgO in the presence of water [27], where the free enthalpy of formation of MgO at 25 ^oC is -601.7 kJ/mol, while $Mg(OH)_2$ is -924.7 kJ/mol at the same temperature. About 117% swelling would occur when $Mg(OH)_2$ is completely formed from MgO, however hydration is not likely to happen in dead burned and pure fused MgO. Water dissociation causes highly hydroxilated surfaces in MgO. According to a theoretical analysis, water dissociation is forbidden on the MgO {100} face [28], and surfaces prior exposed to water inhibits further water dissociation. MgO-base fuel pin were studied in the cases to simulate cladding failure [24], hydride and corrosion were found on the cladding, and swelling, hydroxylation were found from MgO. Kurina et al. [29] suggested the fuel process is vital in the MgO-based fuel performance, sufficient heat treatment addressed the hydroxylation problem, that the MgO-based fuel remained intact after 50 hours in 300 ^oC water, while the insufficiently treated samples broke into (U, Th)O_2 powders, with MgO hydroxylated.

Physical properties

The properties of MgO are summarized in Table 1 below:

Table 1 Physical properties of MgO [30].

Melting point	2827 ^{o}C
Thermal conductivity at 500 ^{o}C 1000 ^{o}C 1500 ^{o}C 2000 ^{o}C	 20 W/K m 13 W/K m 6 W/K m 5 W/K m
Lattice constant	4.212Å
Specific heat [31] at 27 ^{o}C 227 ^{o}C 727 ^{o}C 1727 ^{o}C 2727 ^{o}C	 0.929 kJ/(kg K) 1.126 kJ/(kg K) 1.272 kJ/(kg K) 1.339 kJ/(kg K) 1.360 kJ/(kg K)
Chemical reactivity towards Iron Liquid sodium Water Nitric acid	 No reaction below 1100 ^{o}C No reaction Hydroxylation Low rate of dissolution

Crystal structure

Magnesium oxide with ionic bonding between Mg^{2+} and O^{2-} ions, has a NaCl structure. And the cations and anions occupy the sites as if in a face centered cubic (FCC) lattice respectively. The structure consists of two FCC sublattice, with one made from Mg^{2+} and another from O^{2-}, interpenetrating with each other. MgO has a high melting point of ~2800 ^{o}C, and a density of 3.58g/cm^{3}.

Slip system

The major slip systems of NaCl structures are: {111}<1$\bar{\mathbf{1}}$**0**>, {110}<1$\bar{\mathbf{1}}$**0**>, and {001}<1$\bar{\mathbf{1}}$**0**> systems [32].

The {111} planes are the closet packed planes, and are the primary glide planes for FCC lattice, however, in the ionic case, like MgO, the strong columbic repulsion inhibit such glide. Due to the energy barrier for gliding from columbic repulsion, some half-slip systems are preferred in some cases. The possible half-slip systems are as illustrated in Fig. 4, below. Even {100} planes are more densely packed than {110} planes, deformation via gliding along {100} is not preferred at room temperature. The deformation of MgO occurs via slip along {110} at room temperature. But at high temperature slip along {100} plane becomes possible for MgO. The reason is the high repulsion between Mg^{2+} ions when gliding along {100} plane at room temperature.

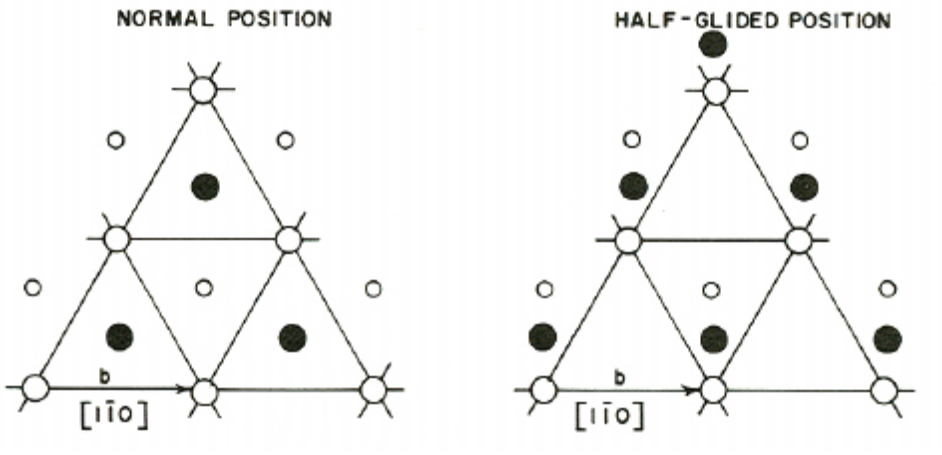

(a) The half {111} <1$\bar{\mathbf{1}}$**0**> slip system

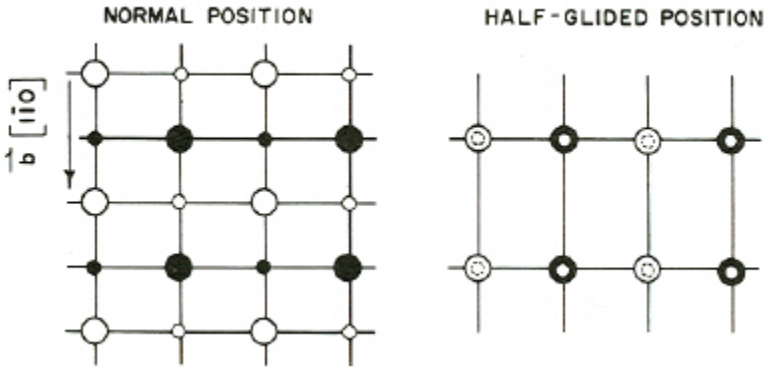

(b) The half {110} <1$\bar{\mathbf{1}}$**0**> slip system

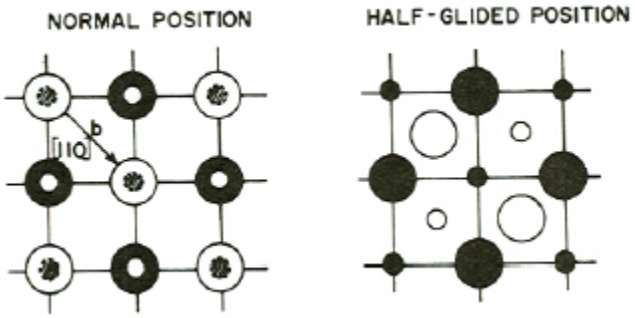

(c) The half {001}<1$\bar{\mathbf{1}}$**0**> slip system

Figure 4 Illustration of half slip on the major slip planes of NaCl structure [32]

Physical properties compared with UO_2

According to [33], the heat capacity of MgO can be expressed as:

$$C_P = 47.26 + 5.68T - 0.87T^2 + 0.1T^3 - \frac{1.05}{T^2}$$

Where C_p is in J/mol-K, the temperature range is 298 ~ 3105 K. The heat capacity of MgO increases with temperature. MgO has higher heat capacity than that of UO_2 [34], which is beneficial especially in reactivity initiated accidents, when MgO can operate in lower temperature under a certain amount of energy deposited per unit mass compared to other materials with low heat capacity.

Generally, the thermal conductivity of MgO is much higher than that of UO_2 and MOX, according to Kirk et al. [35], it's 2.7 times greater than that of UO_2. The published values [34] indicate the single crystalline MgO possess the highest thermal conductivity, and the values decreases with increasing temperature. MgO has a superior thermal conductivity to most of the refractory ceramics proposed as IMF candidates, such as ZrO_2, $MgAlO_4$, and Al_2O_3. One exception is the SiC, that SiC has higher thermal conductivity. However, considering other properties, MgO stands out as one of the most promising IMF potential materials.

MgO has higher thermal expansion coefficients than UO_2 [34], which could possibly lead to separation with fissile phase, enhanced gas release, temperature building up in the fissile phase, and stress on cladding. The thermal expansion of MgO is isotropic due to the cubic crystal structure.

MgO has higher Young's modulus than UO_2 from room temperature up to 1250 K [34], the values decreases linearly with increasing temperature. For example, the reported values are around 300 GPa [36] at room temperature, while UO_2 is around 190 GPa [37]. And the values are not influenced by grain sized reported by Nishida et al. from studying high purity polycrystalline MgO [38].

The fracture strength data [39, 40] have shown that below 600 ^{o}C, the fully dense MgO has greater fracture strength than UO_2 while the studied UO_2 with a 97% of theoretical density has higher values above 600 ^{o}C.

The expected rate of weight loss of MgO under various atmospheres were examined by Lively and Murray [27]. A complete weight loss can occur rapidly at temperatures as high as 1600 ^{o}C in a reducing atmosphere and under vacuum, while it's moderate in inert atmosphere, and insignificant in oxidizing atmosphere containing water vapor.

Radiation damage study

MgO will be subject to fast neutrons with kinetic energy greater than 1 MeV, various energetic fission products, and high temperature if used as the matrix materials for IMF. Estimations have shown that the fuel center can be heated up to 700 ± 140 ^{o}C at a linear power of 590 W/cm in an MgO-PuO_2 fuel form [41]. The radiation damage study of MgO is particularly crucial to examine the feasibility of its application as inert matrix material.

There are two irradiation damage mechanisms, i.e. radiolysis damage and displacement damage. Radiolysis damage arises from the decay of electronic excitations formed during the irradiation (non-impact), but displacement damage from the elastic collision of incident particles and target atoms (impact). Radiolysis damage was extensively revealed in alkali-halides, but was not suspected in MgO because the displacement energies for both ionic species are significant larger than the energy available from the excitation states. Displacement damage occurs only when the energy transferred from an incident particle is larger than the threshold displacement energy of either ionic species. For an incident particle of mass M_1 and kinetic energy E, the maximum energy E_{max} transferred to a target atom (mass M_2) is [9]:

$$E_{max} = 4M_1M_2E(1 + \frac{E}{2M_1c^2})/(M_1 + M_2)^2$$

Where c is the speed of light, and E is in MeV and E_{max} is in eV. For example in the electron irradiation, the maximum kinetic energy transferred to O is about 52% higher than that of Mg atoms. The displacement energy for Mg and O varied, Zhang suggested the value of 60 eV for both [9], and Park et al. recommended 65 eV for Mg and 60 eV for O by using molecular dynamics simulation on different directions and take compared to the experimental values [42]. Groves and Kelly used 25 eV for both Mg and O species [43].

Electron irradiation

The color centers were introduced to MgO nanocubes by electron irradiation with 100 and 300 keV under TEM [9]. Squared nanoholes were observed on the electron-exit face, and the mechanism was attributed to the removal of MgO molecules as well as stoichiometric Mg and O species. Bulk O-vacancies (F type color centers) were confirmed by valence-electron energy-loss spectroscopy (VEELS). It is concluded that even when the incident-electron energy is smaller than the knock-on displacement threshold energy, MgO still can be sputtered in stoichiometric proportion.

Neutron irradiation

Fewer F^+ centers were detected from annealed MgO in hydrogen prior to neutron irradiation [44]. The lenticular cavities formed under annealing could be the vacancy traps.

Numerous studies have been conducted on the irradiation of MgO by neutron with various fluence and different temperatures [43, 45-48]. However, most of the fluences and temperatures used were lower than that in the light water reactor. The general damage of the neutron irradiated MgO studies are listed below:

Generally, under energetic particle bombardment, atoms in the lattice would be displaced off their lattice sites, leaving vacancies behind, and the displaced atoms could be trapped in some relative empty space between other atoms, and form interstitials

there. More specifically, in MgO, either Mg ions or O ions could be displaced, and created vacancies and interstitials. Under further irradiation, or upon annealing, the point defects could coalesce to form extended defects, such as loops or even dislocation network. Isolated point defects (interstitials and vacancies) are first created under low fluences neutron irradiation. And interstitials loops are formed by coalesce of interstitials with increased fluences or upon annealing. Vacancies are considered immobile in MgO, and therefore remain in the isolated status. The nature of interstitials loops were reported to be perfect loops on {110} planes, with a burgers vector b = ½ <110>, the damage is black dots like, and most likely to be the glissile dislocation loops, and the dpa calculated was 0.075, and a slight lattice parameter increase was observed, it's suggested that most of the interstitials annihilated immediately under irradiation [43]. The annealing coarsened the loops at higher than 800 ^{o}C, and at 1210 ^{o}C, no loops were seen [43]. Upon increasing temperatures or fluences, the size of loops grows, while the density of loops decreases. Stevanovic and Elston [46] have reported that, the size of loops were smaller than 5 nm in MgO after the irradiation with fast neutron fluence of 4×10^{21} n/cm^2 at 473 K, while the size were identified as 5 ~ 30 nm when irradiated with 6×10^{21} n/cm^2 at 923 K. Clinard et al. has reported loops elongation along <110> occurs under a higher fluence of 3×10^{22} n/cm^2, and dislocation networks were identified upon further irradiation [45].

Besides the defects created by neutron irradiation, gaseous fission products are generated since the MgO is subject to transmutation by fast neutron bombardment. Helium and neon are reported to be produced by such transmutation [48]. Annealing

studies have found the bubble formation in the neutron irradiated MgO [47]. The mechanism was attributed to the vacancy condensation, and the cavities formed act as sinks for the helium and neon produced from the transmutation of Mg and O atoms. The vacancy condensation requires a threshold density of mobile vacancies, and therefore, the fluence and temperature should reach certain values to guarantee the amount of vacancies produced and the mobility of vacancies. According to Morgan and Bowen [47], the fluence should be above 10^{20} n/cm^2, and the annealing temperature should be above 1500 ^{o}C. The bubbles were reported to have {100} surfaces.

Volumetric swelling is found in fast neutron irradiated MgO, both in single crystal and polycrystalline cases. The expansion is isotropic, due to its crystal structure. And the trends are swelling increases with fluence [45, 49], but increasing the irradiation temperature prohibits swelling [34]. Recovery by annealing to some extent is reported, and the complete recovery is achieved in samples irradiated at low temperature and low fluences, while only partial recovery is achieved in samples irradiated at high temperature and high fluences. The coarse dislocations formed at high temperature and high fluences might prevent the recovery [50].

Thermal conductivity is reduced after fast neutron irradiation, and only partial recovery is reported by a post-irradiation annealing study [46]. The irradiation was conducted under a fluence of 0.8×10^{20} n/cm^2, and the measured thermal conductivity is 44% less than its pre-irradiation counterpart at 300 ^{o}C. Annealing at 1000 ^{o}C for 24 hours results in 15% reduction of thermal conductivity compared to un-irradiated sample. Besides, the neutron irradiation results in increase in hardness [43, 46, 51],

fracture strength [52], critical resolved shear stress [53], and decrease in Young's modulus [46]. The interstitials loops formed might inhibit slip in neutron irradiated MgO, resulting in the hardening and fracture strength, critical resolved shear stress increase. Lattice parameters were reported to be increased after neutron irradiation, due to the interstitials formed. And annealed sample under hydrogen prior to irradiation showed higher lattice expansion, which could be explained by the excess amount of interstitials resulted from the vacancies trapped in cavities formed under annealing [44].

Effects of other fission products irradiation

Elleman et al. have studied in the in-reactor performance of various ceramic materials which considered the candidates for inert matrix in IMF, and concluded the fission-fragment induced expansion in these materials follow this order [54]:

MgO < SiO2 < BeO < Graphite < Al2O3 < ZrO2 < Pyrolitic Carbon < SiC

The neutron fluence was less than 10^{17} n/cm^2, where the dominant effects were made by the fission fragments. The irradiation was done at 45 ^{o}C in the Battelle research reactor. The stresses were calculated, and compared to their estimated failure values. According to Elleman, after irradiation, the tensile stress induced in MgO is only 13.1 GPa, while the estimated failure stress is 103.4 GPa, and the compressive stress induced by irradiation is 101.4 GPa, compared to the approximate failure stress 1379 GPa. The study showed positive results for MgO subject to fission fragment irradiation.

Beauvy et al. [55] suggested that MgO-AnO_2 based composites have the best performance irradiated by Kr or Cd with energy from 100 MeV to 1 GeV at room temperature, compared to other inert matrix candidates, Al_2O_3, $MgAl_2O_4$ and $Y_3Al_5O_{12}$. The heavy ions used with swift energy as a way to simulate the fission product or recoil ion damage.

When implanted with high dose metallic species, metallic precipitates or compounds could be formed in MgO, especially after annealing. The formation of alkali metal precipitates has been reported before [56]. Perez et al. [57] have reported the high dose iron implantation effects on single crystal MgO. Large concentration of defects is observed via optical absorption after irradiation with a fluence of 6×10^{16} ions cm^{-2} at room temperature. The defects are identified as color centers in both anionic sublattice as well as in cationic sublattice. Iron precipitates with diameter up to 2 nm with superparamagnetism and Fe^{2+} ions either as interstitials or substitional in the perturbed lattice are observed. An extensive dislocation network in the implanted area is observed under Transmission electron microscopy (TEM). Annealing at 700 ^oC completely removed the point defects, and the iron species is mainly aggregated into Fe_2O_3 particles, with a minor portion locate in the MgO matrix substitutionally. TEM reveals large spinel ferrite around 20 nm formed ($MgFe_2O_4$ or Fe_3O_4) when annealed at 800 ^oC, and further annealing up to 900 ^oC increases the ferrite particle size up to 30 nm.

The hardening of MgO from ion irradiation is also reported as it in the neutron irradiated case. Burnett and Page [58] have reported the surface hardening of MgO after Ti^+ irradiation ~ 10^{14} and 3.33×10^{15} /cm^2. The irradiation also results in a more

chemically inert surface. A previous study of Burnett and Page has suggested that amorphization occurs when the Ti^+ fluence is greater than 7×10^{16} /cm^2. Aoki et al. [59] have reported similar phenomenon, that the hardening in the surface is found in MgO irradiated with 130 keV Ar^+, 400 keV Xe^{2+} and 1.8 MeV Ar^+ ions. The Vickers hardness is measured in this study, and the softening is found when increasing dose. The hardening mechanism is speculated to be similar to that induced by fast neutron irradiation, that effective defects production by atomic and electronic processes. The further softening upon higher dose is explained by the gas elements and vacancies produced.

Dislocation TEM results of Horton et al. [60] reveal the damage in single crystal MgO induced by 2 MeV oxygen and 4 MeV iron ion irradiations is primarily consisting of dislocations. The damaged depth reaches well beyond the calculated value. The damaged profiles are peaked by two dislocation zones in both cases, where in between the density of dislocations is less compared to the rest of the profile. In the iron irradiated case, the lower dislocation peak zone is coincident with the peak implanted iron ions, while no such coincidence is found in the oxygen irradiated case. It is indicated that charged defects might influence the dislocation evolution. Zinkle et al. [61, 62] have studied the microstructural changes induced by irradiation in various ceramic inert matrix candidates, including Al_2O_3, MgO, Si_3N_4, SiC, and $MgAl_2O_4$ with variety of energetic ion species. The study concludes that dislocation loops nucleation is very difficult under light ion irradiation, and the defects evolution is strongly affected by the irradiation spectrum. The microstructure of MgO irradiated by 2.4 MeV Mg^+ at room

temperature up to 10 displacements per atom (dpa) consists of mixture of dislocation loops and networks. And Zinkle suggests that the dislocation networks indicating a high point defect mobility, that amorphization would not be possible even under further irradiation at this situation without the assistance of impurity atoms. The concluded sequence of resistance to amorphization of the studied ceramics is:

$$SiC < Si_3N_4 < Al_2O_3 < MgAl_2O_4 < MgO$$

The nature of dislocations formed in MgO under irradiation is less studied. Sonoda et al. [63] reported the observation of interstitial type dislocation loops on {110} planes with a burger's vector b=1/2<110> under various particle irradiations. It is claimed that upon increasing the mass of the irradiation ions, formation rate of the loops increases while the growth rate decreases.

Moreover, MgO is also studied in some large scale global in-reactor programs, either with or without fissile materials added [17-19].

Simulation

Molecular dynamics [42] have shown the displacement energy threshold is very high for MgO, that it's about 65 eV for an oxygen primary knock-on atom and about 90 eV for magnesium. And other studies used the averaged value for both of Mg and O as 60 eV. Park et al. recommended 65 eV for Mg and 60 eV for O by molecular dynamics simulation on different lattice directions and compared to other experimental works [42].

Uberuaga et al. [64] have investigated the collision cascades in MgO at energies from 400 eV to 5 keV, via combining simulations from molecular dynamics, molecular statics, temperature accelerated dynamics, and density functional theory. The computational time scale was made capable to compare to experimental data. It revealed, at the lowest energy, lattice remained mostly intact with only isolated interstitials, vacancies, charge-neutral di-vacancies and di-interstitials. At 5 keV cascades, the most common defects were found to be isolated interstitials and di-interstitials. More vacancy clusters were found at this energy, and they were formed at the collisional phase, no vacancies were detected mobile in this study, while separated interstitials can form di-interstitials by electrostatic attraction. The binding energy per atom of the interstitial clusters was found to increase from 3.6 to 5 eV when cluster size increased from 2 to 16 atoms, the clusters became more stable with increasing size. While vacancies were found immobile, some interstitials clusters can diffuse quickly, there was a long-lived metastable state of hexa-interstitial diffuses one dimensionally on the nano-second scale at room temperature. The charging transfer effect was not considered due to the limitation of model used, which might overestimate the electrostatic force between opposite charged defects. The number of surviving Frenkel pairs was found to be about 45% of the calculated value using Kinchin-Pease method, similar to the metal cases.

The vacancy migration energy (likely oxygen vacancy) was found to be 2.1 eV, which is close to an experimental data 1.9 eV. Other simulation works have found the activation energy for the annealing of F centers in MgO, corresponding to the diffusion

of F centers was up to 3.4 eV [65]. Despite of the discrepancy of data, the immobility of vacancies in MgO at room temperature is confirmed.

The long-time evolution of irradiation damage in MgO has been obtained by a variety of simulation methods [66]. It is concluded that point defects and small defect clusters were formed under low energy, on the order of 1 keV, collision cascades, while over long times, interstitials annihilate with vacancies and aggregate with other interstitials to form large clusters. And a type of cluster consists of six atoms was found to have extremely high mobility. For example the diffusion barrier for isolated Mg interstitial is 0.32 eV, and 0.40 eV for O interstitials, the trend was found that the mobility decreases with increasing the size of clusters. However, a hexa-interstitial has an extremely low diffusion barrier even lower than half of that of the isolated interstitials.

When grain boundaries absorb defects, the interaction between the grain boundary with other defects will be altered significantly [67]. Excess interstitials were placed in the grain boundaries to simulate the radiation damage, and the interaction between vacancies with grain boundaries were studied. The results suggested the interaction is changed considerably and sensitive to the atomic structure of the grain boundaries. In a case, the formation energy of vacancies is significantly reduced on and close to the boundaries, indicating the annihilation would be more effective.

1.4.2 ZrN and Its Related Radiation Mechanisms Studies

ZrN has many good properties that make them as inter matrix candidate materials, and moreover, they can be used in research as surrogate to study the transuranic-nitrides. The radiation response of ZrN serves as indicators of the radiation tolerance of transuranic-nitrides, due to their similarities in atomic radii and physical-chemical properties [30, 68, 69]. ZrN has many physical properties even better than required by the Advanced Fuel Cycle Initiative (AFCI), and it's chemically compatible with transuranic-nitrides. ZrN is strong, has a very high melting point, thermally conductive, and have similar thermal expansion coefficient with transuranic-nitrides. Moreover, it meets the requirement for processing. The density of ZrN is 7.09 g/cm^3.

Physical properties

Many physical properties of ZrN is reviewed below and also compared to other transuranic-nitrides. The physical properties of ZrN are listed in Table 2 below [2]:

Table 2 Physical properties of ZrN

Lattice constant	4.57
Melting point	2953 ^{o}C
Heat capacity (300 K)	40.4 J/(mol K)
Thermal conductivity (300 K)	20 W/m-K [70]
Young's Modulus	~400 GPa
Hardness	~20 GPa
Coefficient of thermal expansion (α_l, 300 K)	6 ~ 7 (× 10^{-6})/K [71]

Crystal structure

Stoichiometric ZrN with Zr:N = 1:1, has the NaCl crystal structure, the same as MgO. However, the difference is the ionic radius of zirconium is much larger than that of nitrogen, that the cubic ZrN crystal can be considered at cubic zirconium stabilized by the nitrogen interstitials. Zirconium ions can still bound with each other, while nitrogen ions are too small and far from each. The coordination number for zirconium and nitrogen are both 12, with nitrogen locates in the octahedral interstitials of zirconium FCC sublattice, with the Zr ions colored in green and nitrogen in blue, the radii were not pictured according to ratio. The cystal lattice is compatible with UN and other transuranic mononitrides, the comparison is listed in Table 3 below:

Table 3 Comparison of ZrN with transuranic nitrides.

Nitride	Crystal structure	Lattice constant (angstrom)	Melting point (K)
ZrN	Cubic-NaCl	4.537	3253
PuN	Cubic-NaCl	4.906	3023
NpN	Cubic-NaCl	4.8979	3103
UN	Cubic-NaCl	4.89	3123

Slip system

The slip systems are similar with MgO, and TiN was reported to slip on the {110} planes with burger's vector b = $<1\bar{\mathbf{1}}\mathbf{0}>$ [72]. Since the similarity with TiN, ZrN is also expected to have the same slip system at room temperature. Other slip systems were also reported, for example the $\{111\}<1\bar{\mathbf{1}}\mathbf{0}>$ system is demonstrated before [73], due to the stoichiometric difference from zirconium nitride samples. ZrN allows a wide range of nitrogen deficiency, and it is usually denoted as ZrN_{1-x}. In an under stoichiometry case, the lots of vacancies exists in the anion sublattice, which might explain other lip systems.

Physical properties compared with transuranic nitrides

The values and equations used are selected as recommended from [74], the most updated and assessed one. Since a considerable variety exists in the ZrN property values, the reason is attributed to the various stoichiometry. Kogel et al. developed a model to calculate the heat capacity of ZrN, and the correlation can be represented by the following equation:

$$C_P = 45.86 + 6.82 \times 10^{-3}T - \frac{5.54 \times 10^5}{T^2}$$

Where Cp is the heat capacity with unit of J/mol K, and T in K. The heat capacity of PuN calculated by Kubaschewski [75] is:

$$C_P = 44.89 + 1.548 \times 10^{-2}T$$

The heat capacity data of ZrN and PuN solid solution, (Pu, Zr)N, is estimated by using the Neumann-Kopp rule, since no such data is available. The correlation is expressed as:

$$C_P = a_{ZrN}C_{P,ZrN} + a_{PuN}C_{P,PuN}$$

Where a is the molecular fraction of PuN and ZrN of the solid solution. According to this rule, the heat capacity of (Pu, Zr)N solid solution lies between the values of PuN and ZrN, with PuN having higher values than ZrN. Other capacity of transuranic nitrides with ZrN solid solution can only be estimated from (Pu, Zr)N values, due to the lacking of data reported.

The thermal conductivity data reported from Hedge et al is mostly recommended, and a parabolic correlation to fit the data is expressed as [74]:

$$k_{ZrN} = 1.423 + 2.042 \times 10^{-2}T - 6.404 \times 10^{-6}T^2$$

Where k is the thermal conductivity in W/m-K and T in K. The data of PuN is selected from the values reported by Arai [76], and a fitted expression is as:

$$k_{PuN} = 6.906 + 7.653 \times 10^{-3}T - 2.011 \times 10^{-6}T^2$$

Arai has also reported the thermal conductivity of NpN, and the correlation is as:

$$k_{NpN} = 7.89 + 1.27 \times 10^{-2}T - 4.32 \times 10^{-6}T^2$$

No data of (Pu, Zr)N solid solution thermal conductivity is available, and an estimation has been adopted from the similarities between UN and ZrN in terms of crystal structure, and lattice parameters [74]. The effect of UN content in the (Pu, U)N is measured before [76]. The accordingly effect of ZrN content in (Pu, Zr)N solid solution is expressed as:

$$k_{(Pu,Zr)N} = (1 - \sqrt{1 - x_{ZrN}})k_{ZrN} + \sqrt{1 - x_{ZrN}}\{x_{ZrN}k_m + (1 - x_{ZrN})k_{PuN}$$

$$k_m = -8.432 + 14.438x_{ZrN} + 0.014T - 1.957 \times 10^{-6}T^2 - 1.549 \times 10^{-3}x_{ZrN}T$$

Where X_{ZrN} is the molecular fraction of ZrN in the solid solution. Other transuranic-nitride and ZrN thermal conductivities can be estimated by using this method, since no literature data is available for these values.

Radiation tolerance

Displacement energy threshold

There is no direct report on the displacement threshold energy of ZrN, but by comparing with other similar ceramics, the reasonable range could be obtained. In GaN, the average displacement energy of N is 32.4 eV, while it's 73.2 eV for Ga, with the minimum E_d is 17 eV and 39 eV respectively both along $< \bar{1}010 >$. In 3C-SiC, the minimum displacement energies are 20 eV and 49 eV along <100> for C and Si respectively [77]. Yang et al. used the value of 35 eV for Zr and 25 eV for N based on the estimation of ZrC [78].

Radiation damage studies on ZrN

Despite its great potential, there are only handful studies [78-81] exploring the radiation response of ZrN, with mostly promising results. Some of the available studies are reviewed below:

High doses of argon were implanted into ZrN thin films with residual stress measurements made by GIXRD. Up to 4×10^{16} Ar/cm^2 at 100 keV was implanted, which produced up to 12 atomic % argon in the lattice. The result was that, at the 1% atomic concentration of implanted Ar area, both of the lattice parameter and the

compressive residual stress were reduced, and it's concluded that the implanted Ar resided at the substitutional sites and softening was found attributed to the energy accompanying the implantation process. While at the 12 atomic % Ar implanted area, the residual stress was barely affected, where the lattice parameter reduction continues but less rapidly. It's suggested that at the area, Ar bubbles were formed [82].

Another study on zirconium nitride was performed to assess the effect of radiation damage by heavy ions at cryogenic and elevated temperatures. Xenon and krypton were used as heavy ions at 300 keV to displacement damage up to 200 dpa. Implantations were conducted at cryogenic, 350 ^{o}C, 580 ^{o}C , and 800 ^{o}C . Amorphization was not observed at low temperatures nor was bubble formation observed at elevated temperatures, however, defect migration was observed at elevated temperatures. Nanoindenter results showed the onset of defect saturation. Helium release studies were performed to show the effect of increasing damage by Xe to 40 dpa [80].

Nanocrystalline (nc)-ZrN remained intact after various types of swift heavy ion irradiations, such as 167 MeV Xe, 250 MeV Kr, and 695 MeV Bi [83]. Blistering tends to occur in annealed nc-ZrN irradiated with hydrogen or helium, but is suppressed by swift heavy ion irradiation of Xe at 167 MeV following the helium irradiation, the mechanism is attributed to swift heavy ion induced epitaxial crystallization [79].

ZrN films were synthesized by sputtering, and later subject to cobalt implantation reported by Zanghi et al., with a very high fluence to reach a concentration of 10 ~ 30% in the doped zone at room temperature [84]. No amorphization was observed, and Co coalesced into Co clusters were found. The reason was attributed to the high stability of

the matrix and the Co-N bonds are not favored chemically. Similar precipitation was found in Cu and Ni implanted AlN.

Slight electrical resistivity decrease was reported in neutron irradiation performed at moderate flux. While the decrease was seen in ZrN, electrical resistivity increase was observed in ZrC and NbC [2].

Irradiation under 2.6 MeV proton at 800 ^{o}C showed no amorphization or precipitates, and no voids or bubble formation were detected at a dose of 0.75 dpa. The irradiated microstructure mainly consisted of a high density of dislocation loops and point defects, and some of the loops were of vacancy-type in nature [78].

1.4.3 TiN and Its Related Radiation Mechanisms Studies

Titanium nitride (TiN) is a common material for abrasive and hard tool coating , and also used as decorative coating for its gold-tone appearance, which is seen on coated drill bits and other machining tools [85, 86]. It is proven to be very affordable for common tasks as titanium is plentiful. The nitriding of Ti is easy and the technique is very mature and often used. Despites some difference, TiN is very similar with respect to ZrN, and TiN has been the subject of much research for its outstand chemical-physical properties. TiN also has the NaCl cubic structure, which is common for most transition metal nitrides as well as MgO studied in thesis. And similar with other cubic metal nitrides, the intrinsic anion sublattice vacancies exist and are difficult to characterize. Moreover, the phase diagram of TiN is similar to that of ZrN. However, there are some

differences. First, there is a line compound of a N to Ti ratio about 0.36 with ε crystal structure. And there are both sub- and super-stoichiometric phases of titanium nitride. Pulsed laser deposition (PLD) technique has been commonly used for synthesis of TiN films due to its capability of allowing for a precise control of crystallinity, stoichiometry, and defects concentration [87, 88].

Physical properties

TiN has a high hardness (20 ~ 35 GPa), and very hard TiN films were synthesized by PLD at 300 ^{O}C [89], another study by the same author reported a hardness up to 40 GPa[90]. Moreover, TiN has a very high melting point (close to 3000 ^{o}C), refractory material with good wear resistance, very low electric resistivity, and good thermal conductivity and stability [90]. TiN is also a superconductor with a reasonably high T_c. Table 4 summaries some of the properties of TiN.

Table 4 physical properties of TiN

Lattice constant	4.26
Melting point	2950 ^{o}C
Heat capacity (300 K)	37.4 J/(mol K) [33]
Thermal conductivity (300 K)	110 W/m-K
Young's Modulus	~590 GPa
Hardness	20~40 GPa [90]
Coefficient of thermal expansion (α_l, 300 K)	9.36 (× 10^{-6})/K

Radiation tolerance

The radiation study on non-metals were mostly focused on electronic or magnetic properties [91, 92]. However, the radiation tolerance of TiN has not well studied besides its heavy use in industry [93]. Perry has shown the gas and metal implantation into monolithic TiN has the effect on the residual stress and strain distribution by grazing incidence angle X-ray diffraction (GIXRD) [94-96]. [94]Perry also conducted Ar and Kr implantation into TiN, and found little effects on the lattice parameter and residual stress with either of the gas implantation of 1%, but precipitate into bubbles at 4% implantation, and Ar slightly reduces the lattice parameter and made the residual stress more tensile, while Kr had the opposite effects [97]. Transmission electron microscope (TEM) studies together with the GIXRD depth profiles showed that, wlarge doses of a heavy ion implantation generated a damage profile far beyond the calculated distribution of displacement damage and implant ion range, which reached up to 10 times greater than the calculated depth [2].

1.5 Key Defects Mitigation Mechanisms and Approaches for Materials

1.5.1 Grain Boundary and Interface Related Approaches

In general nc metallic and ceramic materials have abundant grain boundaries (GBs), which are effective defect sinks for radiation induced point defects. Molecular

dynamics (MD) simulations show that GBs in Cu can absorb and then reemit interstitials in to grain interior to combine with vacancies in close proximity to high angle GBs [98]. The GB sink strength appears to increase with increasing misorientation angle in Cu as revealed by the change in width of GB denuded zones [99]. Wang et al. shows that nc-TiN with an average grain size of 8~100 nm showed greater radiation tolerance than its coarse grained counterpart, as evidenced by the diminishing damage zone subjected to He ion irradiations [93]. Similarly nc metals [100-102] have shown enhanced radiation tolerance. *In situ* studies on nc-Ni show that high angle GBs can effectively capture and annihilate defect clusters and dislocation segments [100].

Other defect sinks, such as layer interfaces, have been increasingly investigated to absorb radiation induced point defects and their clusters [103-106]. There are limited studies on radiation response of nitride based multilayers. In a He ion irradiated study on MgO/TiN multilayer, the suppression of defect accumulation was shown in the MgO layers, whereas a high-density of defect clusters were identified in the single layer MgO film. In parallel, in AlN/TiN systems, no amorphization was seen in AlN layers of the AlN/TiN multilayers, while an obvious amorphized layer was identified in the single layer AlN film [107, 108], which actually result in higher amount of interfaces and thus better radiation tolerance properties.

1.5.2 The Major Approaches Taken in the Thesis Work

In this study, both grain boundaries effects and interfaces effects on the radiation damage accumulation and annihilation were explored, as well as compositional effects were also discussed. MgO thin films were synthesized into epitaxial film via the epitaxial growth on single crystalline TiN film as a buffer layer by domain matching. Besides, polycrystalline MgO films were grown on the polycrystalline ZrN, and non-epitaxial interfaces between MgO and ZrN were also incorporated. Different grain sizes of MgO were achieved by the confinement effects of the MgO layer thicknesses between ZrN layers, and by varying the deposition temperature. Moreover, ZrN thin films with different grain sizes were synthesized by the pulsed laser deposition (PLD) at different temperatures.

Therefore the grain size effects, and the different interface (epitaxial interfaces as in MgO/TiN and no-epitaxial interfaces as in MgO/ZrN) in nature effects on the radiation induced defects evolution and annihilation was explored by combining *ex-situ* ion irradiation and *in-situ* ion-irradiation techniques. The radiation tolerance was measured by the variation of nano-hardness (softening or hardening), crystallinity (amorphization), microstructure (defects density, grain growth), and electric resistivity before and after radiation.

CHAPTER II

EXPERIMENTAL

2.1 Pulsed Laser Deposition (PLD)

Lasers are of great interest in many areas, for both scientific and industrial purposes due to their high energy, coherency and monochromatic charasristics. Monochromaticity allows the control of the depth of heat treatment and selectivity. The high energy of the laser beam and its directionality permit a high spatial resolution on the materials exposed. . The applications include laser annealing of semiconductors, surface cleaning by desorption and ablation, improved surface hardening with laser-induced rapid quenching, and pulsed laser deposition for growing thin films. The pulsed laser deposition technique is used for deposition of the MgO, and metal nitrides studied in this thesis.

The PLD system consists of the laser source, optical components, vacuum chamber, and the pumping system as shown in Fig. 5. The laser is generated by a KrF excimer gas with a wavelength of 248 nm. The pulse duration is 20 to 25 ns. Via the aperture, reflective mirror, and focus lens, the beam is directed and focused on to the target surface inside the vacuum chamber. The chamber houses a rotating target mount and substrate stage which is directly facing the target with a distance of 5 cm. Heating stage is connected with the substrate mount, and a temperature range from room temperature up to 800 ^{o}C can be adjusted, and monitored. The vacuum is achieved by a two stage pumping system, which includes a scroll mechanical pump and a

turbomolecular pump, and the vacuum is obtained below 10^{-8} mbarr. A compact pressure gauge is assembled with the chamber, which utilizing a Pirani gauge in the low vacuum (ambient to 10^{-2} mbarr), and an ionizing gauge at the high vacuum range (below 10^{-4} mbarr).

The interaction between the laser and the target consists of three stages. First, the electro-magnetic energy of the beam is transferred to the target as electric excitation, and later chemical energy, thermal energy, causing local melting, and target materials evaporation. The second stage involves the interaction between laser beam and the evaporated target materials, forming plasma. Plasma is a hot gas-like phase of materials, which is quasi-electric neutral, consisting electrons, ions, as well as atoms and molecules. In the third stage, the plasma expands and eventually condenses on the substrate surface. Because of the high kinetic energy of the ad-atoms on substrate surface, impinge species would reside at nucleate sites via random walk, and growing as grains or epitaxial film.

The advantages of pulsed laser deposition include reproduction of the target stoichiometry, high kinetic energy provided to the ad-atoms, little contamination, and a good control of thin film properties.

Figure 5 Picture of PLD system where the laser source, optical path, vacuum chamber, and pumping system are shown.

By choosing the appropriate parameters such as target materials, laser energy density, partial gas pressure, pulse repetition rate, and deposition temperature, thin films of many materials with various microstructures can be deposited.

2.2 Ion Implantation

2.2.1 Ex-situ Irradiation Technique

Ion implantation is a powerful technique for surface analysis, material property modification, which is widely used in micro-electronics fabrication, via which energetic ions are implanted into substrates such as Si, the energy of implants varies from 1 keV to 1 MeV, and the average implant depth ranges from 10 nm ~ 10 μm. The dose ranges

from 1012 / cm2 to 1018 / cm2, depending on the different applications. And this technique is also employed to improve surface properties of materials or to create new phases, due to its capability of controlling doping with chosen impurities. For example, metal nanoparticles synthesis in silica glasses [109, 110], and doping of lithium niobate in rare earth [111] have been reported by using ion implantation for production of materials with interesting optical properties. Ion implantation is also a primary tool for study of the fission-products radiation-damage including defects generation, crystal structure change (such as amorphization), and chemical-physical properties change etc. Rate, dose, incident angle and implantation temperature can be manipulated during the implantation to achieve a desired implant concentration, depth and damage level. Different elements with various energies can be selected for the implantation to simulate damage in a nuclear reactor or to modify the properties of the implanted materials, such as surface structure of a thin film, dope in the semiconductor, alter the chemistry, and etc. For example, Xe and Kr are the common fission products, and released with sufficiently high energy to produce large damage cascades, which may displace many more lattice atoms per each implanted atom and eventually cause defects and deterioration in the implanted materials. Ion-implantations with these noble gases into materials of interest can provide valuable data regarding the damage produced, and how to mitigate such damage. The implantation temperature is controlled to study different defect mechanism, for example, implantations at cryogenic temperatures provides information of the defects accumulation since the recombination rate of defects is low at such temperature, and high temperature implantation demonstrate how defects interact

with each other and with the microstructure. It is a commonly used approach in the research of radiation damage on metals, and increasingly used in the studies in ceramics. The ex-situ irradiation conducted in this study is done by the ion implantation. He+ and Fe2+ ions were used for the implantation, after which other characterization techniques were used to study the variation due to radiation damage. And it is specified as ex-situ irradiation because of the difference of this technique with the in-situ irradiation one.

2.2.2 In-situ Irradiation Technique

TEM is a powerful tool for the characterization of defects (dislocation loops, voids, and bubbles) in solids induced by ion or electron irradiations. For example, bright-field and dark-field imaging, electron diffraction, and chemical analysis, such as energy dispersive X-ray spectroscopy (EDS), have been widely utilized to characterize irradiation induced defects, structural change, as well as chemical variation [112]. *In-situ* irradiation technique incorporates the conventional TEM with ion implantation that allows recording of the microstructural evolution under well-controlled irradiation conditions, which provides critical information for understanding the defects generation, development and annihilation processes when they take place. *In-situ* irradiation technique was first originated from the utilization of the energetic electrons to produce point defects in conventional TEM sample under high voltage electron microscopy. With decades of development, this technique has been used to study the microstructural change under radiation in metals, ceramics, and semiconductors. *In-situ* irradiation

technique can bridge the gap of length and time scales between the simulations and *ex-situ* experiments [113].

2.3 Hardness by Nanoindentation

Nanoindentation is a surface sensitive technique that the penetration depth is controlled to be in the nanometer scale. Usually a very small diamond indenter tip with certain geometry is used to measure the hardness and elastic modulus of the sample. A precise control is done by a computer of navigating the nanoindenter across the sample surface, and the load force as well as displacement was tracked by the software. Hardness and modulus data is later calculated based on the loading-unloading curve recorded. The accuracy of the measurement is highly dependent on the sample surface, such as smoothness, orientation, and chemistry (whether surface oxide layer exists), and error may also come from the tip not being perfectly sharp. Usually, the measurement is taken at a depth below 50 nm from the sample surface, and within 10% of the thin film thickness to avoid the surface as well as the substrate influence on the hardness measurement.

2.4 X-ray Diffraction

X-ray diffraction (XRD) is a commonly used non-destructive analytical technique to identify the structure (crystal orientation, crystallite size, stress) and

chemical composition of crystalline materials. Constructive interference occurs when the Bragg's condition is satisfied by the interaction of x-ray with the crystal structure, shown in Fig. 6. As an incident x-ray beam with wavelength λ at an incident angle θ illuminates on the crystal planes, the difference of path length between diffracted beams from consecutive planes with interplanar spacing d is calculated as $2d \sin\theta$. For constructive interference, this value must equal to an integral multiples of wavelength, i.e. $n\lambda$, where n is a whole number, as given by the equation below:

$$n\lambda = 2d \sin\theta$$

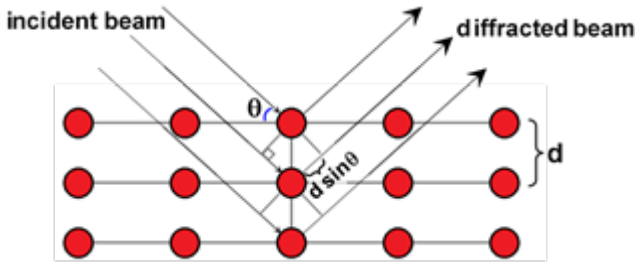

Figure 6 Illustration of Bragg's diffraction.

As the incident angle θ is varied, the Bragg diffraction is satisfied for certain crystallite orientations in a polycrystalline sample. For an x-ray source of known wavelength, the angle of the diffracted beam is measured and recorded, and from the interplanar spacing d of reflections can be calculated. This is the most basic form of XRD measurement and analysis, referred to as powder diffraction, that the polycrystalline sample with random orientation distribution is measured. Thin film

analysis requires a set of advanced XRD techniques, such as grazing incidence angle XRD, rocking-curve analysis, reciprocal space mapping, and pole figure measurement, for characterizing epitaxy, texture, determining lattice constant, defects, and surface roughness.

2.5 Transmission Electron Microscopy

TEM is a very powerful tool for the characterizations of materials that offers information of sample crystallography, defects, and chemistry with a sub-nanometer resolution. The imaging is formed via the interaction of transmission high energy electron beam with an ultra-thin sample foil (thinned below 100 nm to ensure electron transparency). The resolving power of TEM is much higher of the optical microscope due to the high energy and thus small wavelength of electrons. The resolution is given by the Rayleigh criterion as:

$$R = \frac{0.61\lambda}{n\,sin\alpha}$$

where λ is the wavelength of the illumination electron beam, n is the refractive index of the lens, and α is the half angle of the maximum cone of beam. The wavelength λ in nm of an electron beam at an accelerating voltage V is calculated as:

$$\lambda = \frac{1.22}{\sqrt{V}}$$

The accelerating voltage of 200 kV is used in this study, and therefore resulting in a λ value of 0.0027 nm, and therefore the resolution of TEM can reach to a sub-nanometer scale.

Shown in Fig. 7. are the components of a typical TEM, consisting of four main parts: the electron source, several sets of electromagnetic lenses, the sample stage, and the image acquisition systems, all of which are contained under a high vacuum column. There are two basic modes of operation: the imaging mode and the diffraction mode, which provide information of the sample image with contrast and electron diffraction pattern respectively. The mode can be changed by adjusting the focal length of the intermediate lens.

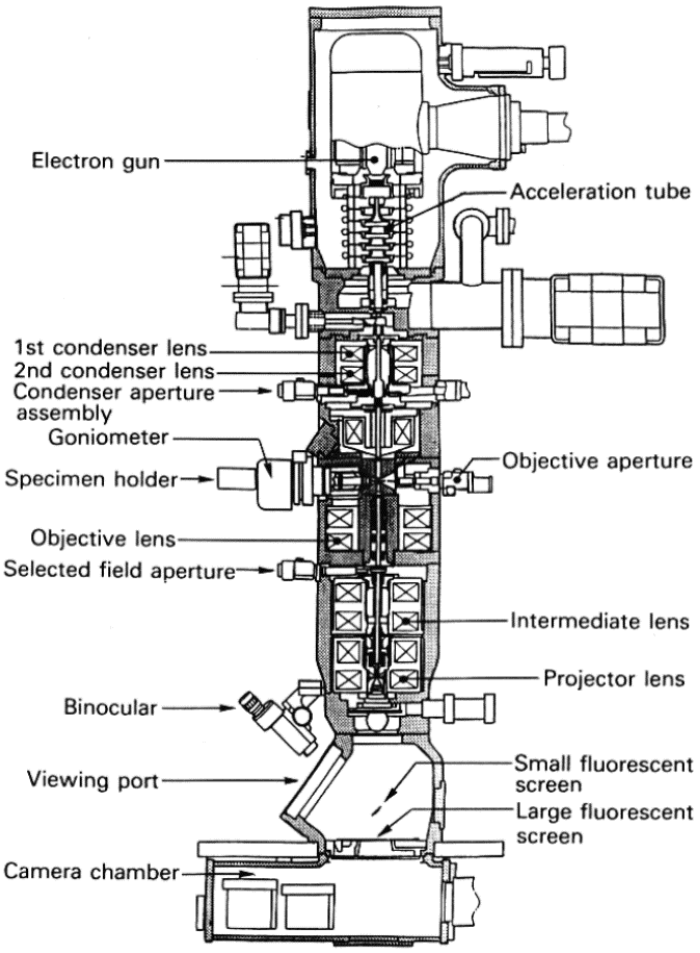

Figure 7 Block diagram showing the layout and major components of a TEM [114].

Inserting appropriate objective apertures could improve the contrast of the imaging, allowing only certain diffraction beam coming from the interested regions to pass through, which is often used to obtain the dark-field image from a certain diffracted orientation.

Specific information can be obtained by additional imaging techniques in TEM, such as the atomic scale crystallography can be imaged by high-resolution TEM (HRTEM). And elemental mapping is possible with the technique of electron dispersive x-ray spectroscopy (EDS) and electron energy loss spectroscopy. The electron beam, in this case is a focused beam rastering across the sample, and the signal such as characteristic x-ray is generated. STEM imaging provides contrast related to the atomic mass since it uses a high angle annular dark-field (HAADF) detector to collect elastically scattered electrons.

CHAPTER III

ENHANCED ION IRRADIATION TOLERANCE PROPERTIES IN TIN/MGO NANOLAYER FILMS[*]

3.1 Overview

Interface mitigation effects on ion irradiation induced damage are explored in TiN/MgO nanolayer thin films with nanolayer thickness varied from 10 nm to 50 nm. After ion irradiation with He ions to a fluence of 4×10^{16} cm^{-2} at 50 keV, no hardness variation is observed in the nanolayer samples based on the nano-indentation measurement, and high resolution TEM indicates no obvious ion damage in the MgO layers in the nanolayered samples. However, single layer MgO film shows a significant hardness increase of ~20% and high density point defect clusters (~5 nm) are clearly identified. These results suggest that, in this system, nanolayer interfaces could act as effective point defect sinks and be responsible for the enhanced radiation tolerance properties.

[*] This chapter is reprinted from Journal of Nuclear Materials, 434 (2013), L. Jiao, et al, *Enhanced ion irradiation tolerance properties in TiN/MgO nanolayer films*, 217-222, Copyright (2012), with permission from Elsevier.

3.2 Introduction

Ion irradiation damage mechanisms in MgO have been extensively studied for decades [115]. MgO has a simple rock salt structure, high melting temperature, relatively high thermal conductivity compared with other well-studied refractory ceramics, such as ZrO_2, $MgAlO_4$, and Al_2O_3 [24]. Moreover, it's compatible with reactor materials and has a low thermal neutron absorption cross-section [25]. These features make MgO an envisioned candidate for Inert Matrix Fuel (IMF) application, which could deal with the proliferation problems associated with the current fuel forms [24]. However, MgO is sensitive to radiation damage, and irradiation hardening has been widely observed [116]. It is the result of hampered dislocation slip and solid-solution hardening. More specifically, in MgO, isolated point defect clusters are commonly formed under light ion irradiations as well as some heavy ion implantations at low temperatures. At elevated temperatures, the density of point defect clusters reduced either by annihilation of opposite point defects or formation of obvious interstitial loops. In some cases, secondary phases such as metal precipitates were identified. Under certain high damage circumstances, eventually amorphization started, and the hardness decreased to a lower value than that of the unimplanted one [63, 117, 118]. Very few work has been conducted to enhance the radiation tolerance properties of MgO, e.g., Chen and Abraham reported the suppression of radiation damage of MgO through Li doping [119]. However, the question remains on whether extended defect clusters and accumulation can be suppressed by this approach.

Recently, radiation tolerance properties of nanostructured materials have attracted significant research interests owing to the observed enhanced radiation tolerance properties in various nanomaterials including metals and ceramics. For example, Zhang et al. reported that the immiscible interface acts effectively in reducing radiation damage, such as swelling, helium bubbles formation, and radiation hardening in several metallic multilayer systems, including Cu/Nb, Cu/V, Al/Nb, and Fe/W [120-123]. The defects annihilation effects of grain boundaries in nanocrystalline ceramic materials was first demonstrated in TiN films [93]. Moreover, Shen et al. provided a thermodynamic explanation of the grain boundary effects which could either enhance or harm the radiation tolerance depending on the grain sizes and the system chosen [124]. Atomic-scale simulations have been carried out for several metal multilayer cases. For example, Misra et al. reported that the greatly reduced formation energy of interfacial point defects drastically drives the vacancies and interstitials formed in radiation cascade into the interface, where they get recombined [125]. These simulation studies provide a guide to understand the mechanism of interface mitigation effect in metallic nanolayer systems. Nevertheless, although plenty of irradiation studies have been carried out on various bulk ceramics, as well as bulk and thin film metallic systems both experimentally and theoretically, similar studies on nanostructured or nanolayered ceramics were scarce [126].

In this work, MgO-based nanolayer thin films have been synthesized to explore the interface-mitigation mechanism in MgO, one of the well-studied ceramic materials for ion irradiation tolerance properties. For this study, a transition metal nitride, TiN, is

chosen as the interlayer material based on the following considerations: (1) TiN is considered as a good radiation tolerant material, in addition to its outstanding mechanical properties and thermal stability [58]; (2) More importantly, decent epitaxial growth of MgO can be achieved with TiN as they are both face centered cubic with very closely matched lattice parameters (a_{TiN} = 0.426 nm and a_{MgO} = 0.419 nm measured by XRD). The epitaxial MgO/TiN nanolayers synthesized in this study minimize the contributions from grain boundaries and other defects, and therefore provide a relatively clean model system to illustrate the interfacial effects on irradiation damage. This study could provide a design guideline for ceramic nanomaterials with enhanced radiation tolerance properties.

3.3 Experimental Details

TiN/MgO nanolayer thin films were deposited by a pulsed laser deposition technique in a high vacuum chamber with a KrF excimer laser (Lambda Physik Compex Pro 205, λ = 248 nm, 10 Hz). Laser beam was focused to obtain an energy density of approximately 5 J cm^{-2} at 45° angle of incidence. Targets were hot-pressed stoichiometric TiN and MgO obtained from Plasma Materials, Inc. The nanolayer films were deposited at a typical growth rate of 0.3 Å/pulse for TiN and for 0.25 Å/pulse for MgO with a base pressure of approximately 10^{-7} Torr and deposition temperature of 700 ° C. Prior to film deposition, Si (0 0 1) substrates were cleaned in acetone and

methanol followed by etching in buffered hydrofluoric acid to remove native silicon oxide layer on surface.

A TiN seed layer of about 100 nm was first deposited on silicon substrate to grow epitaxial cubic TiN/MgO nanolayers for all samples. Four different sets of TiN/MgO nanolayer films with various individual layer thicknesses of 5 nm, 10 nm, 20 nm and 50 nm were deposited. For comparison, samples of single layer TiN and MgO films were deposited as well. The total thickness was controlled to be 500 nm including the TiN seed layer for all sets. X-ray diffraction was used to measure the lattice parameters. The samples were then irradiated at room temperature with He ions to a fluence of 4×10^{16} cm^{-2} at 50 keV. Microstructural evolution was characterized by high resolution TEM (HRTEM) using a JEOL 2010 analytical electron microscope with a point-to-point resolution of 0.23 nm and an accelerating voltage of 200 kV. All TEM samples were prepared under the same conditions (including a final ion polishing step with 3 keV Ar^{+} beam for less than 1 h). Ion milling damage induced by the TEM sample preparation is minimal as seen from the minimal amorphous edge from the TEM sample and the amount of damage is comparable in all the samples.

Hardness of all films was measured by a Hysitron Tribo-nanoindenter. The measurements were performed using a standard Berkovich diamond tip under a constant load mode with the load varied from 2500 to 4000 μN. In order to minimize any substrate effect on hardness measurements, the penetration depth was controlled to be less than 20% (~100 nm) of total film thickness. Hardness was calculated based on the average of at least 60 indentation experiments per sample.

3.4 Results and Discussion

SRIM 2008 [127] was used to simulate the damage profile in single layer TiN and MgO caused by He ion irradiation for planning the ion implantation experiments. The peak displacements per atom (dpa) are 3.1 and 2.1 at the depth of 190 nm and 230 nm from film surface for TiN and MgO, respectively, both are within the film layers. He ions were chosen here to simulate the impact of alpha particles generated from the nuclear reactions and to compare with previous studies using the He irradiation effects on both metals and ceramics [93, 120, 128]. Room temperature ion irradiation is selected for this work to allow defects accumulate rapidly at relative low dosage and avoid the complexities of interlayer mixing for the nanolayer samples. The overall dpa was estimated by averaging the displacements of the two sublattices, even though there is a difference in the displacement energy for the sublattices, and light gas ions are likely to produce defects in anion sublattice [118]. The dpa range selected for this study is comparable to a previous report on ion irradiation damage of MgO where obvious defect clusters and small dislocation loops were clearly observed at doses up to 10 dpa (including the displacements of both Mg and O sublattices) [62]. In addition, the damage peaks in the nanolayer sets are expected to be within the film layers if no interface effect is taken into consideration.

TiN single layer sample shows no obvious variation in microstructure based on the TEM images (not shown here) after ion irradiation, which was attributed to its robust ion-irradiation tolerance properties. For the as-deposited MgO single layer samples, the

MgO layer appears clear with a sharp interface with the TiN seed layer, as shown in Fig. 8 (a). However, after the He ion irradiation, an obvious damaged layer with a high density of small defect clusters, 200 nm to 400 nm away from the top surface can be identified by the dark contrast, which is consistent with the SRIM simulation result, i.e., the peak displacement damage and the peak implanted ion area both located within 200 – 400 nm, as illustrated in Fig. 8 (b). Moreover, the interface between MgO and the TiN seed layer is not as clear as the as-deposit one, which indicates possible radiation induced intermixing. Based on the corresponding SAED patterns for both the samples before and after ion irradiation, the epitaxial quality of the MgO layer is maintained after ion irradiation, only with slightly broadened (0 0 2) diffraction spots as indicated in the SAED pattern. This might be caused by the defect clusters formed in the MgO layer due to ion irradiation.

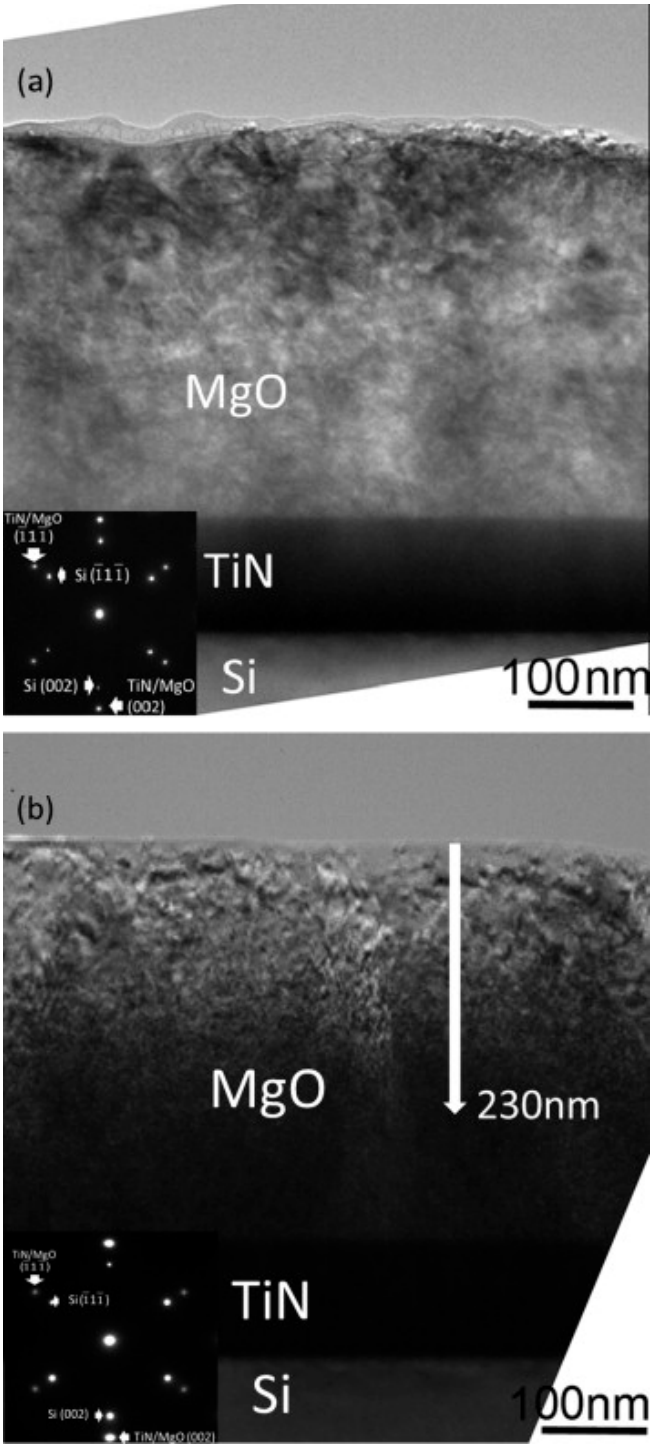

Figure 8 Low magnification bright field XTEM micrographs and selected area diffraction (SAD) patterns of 400 nm MgO single layer films with 100 nm TiN seed layer on Si (0 0 1) substrate, (a) as-deposited and (b) ion-irradiated with He^{+} 50 keV at a dose of 4×10^{16} cm^{-2}.

Fig. 9 (a) and (b) show the low magnification cross-sectional TEM images of the ion irradiated MgO single layer film under bright field (BF) and dark field (DF), respectively. High density defect clusters are clearly observed in both BF and DF modes and shown as opposite contrast in the two imaging modes. The average cluster size is around 5 nm, as circled in the enlarged images (inset in Fig. 9 (a) and (b)). Similar defect clusters with similar sizes were reported in previous studies of ion irradiated MgO [129]. Irradiation damage evolution in MgO with various energetic particles has been well documented, such as studies with light gas ions (Ne, Xe, He, and H) alkali (Li, Na, K, and Rb), iron, indium, or gold ions. Point defects accumulation under room temperature irradiations was widely reported [118]. Those damages have been identified as point defect clusters mainly based on these studies [118, 130]. After irradiation, interstitials and vacancies are created. At room temperature, the vacancies are immobile and remain isolated. Whereas for interstitials, they can aggregate to from clusters, and gradually form interstitial loops [66]. Previous reports have argued that those defect clusters which are around several nanometers, are interstitial clusters, and even some interstitial loops. For example, Groves and Kelly concluded these loops are unfaulted interstitial dislocation loops with Burgers vectors $b = \frac{1}{2}\langle 1\ 1\ 0\rangle$ approximately on {1 0 0} planes in fast neutron irradiation [43]. Similar observation was reported for He irradiated cases as well as other irradiation with various implant species [60, 131, 132]. Moreover, multiple computational methods revealed the high mobility of interstitial clusters especially the metastable hexa-interstitial clusters, and the immobility of isolated vacancies formed in collision cascades at room temperature in MgO.

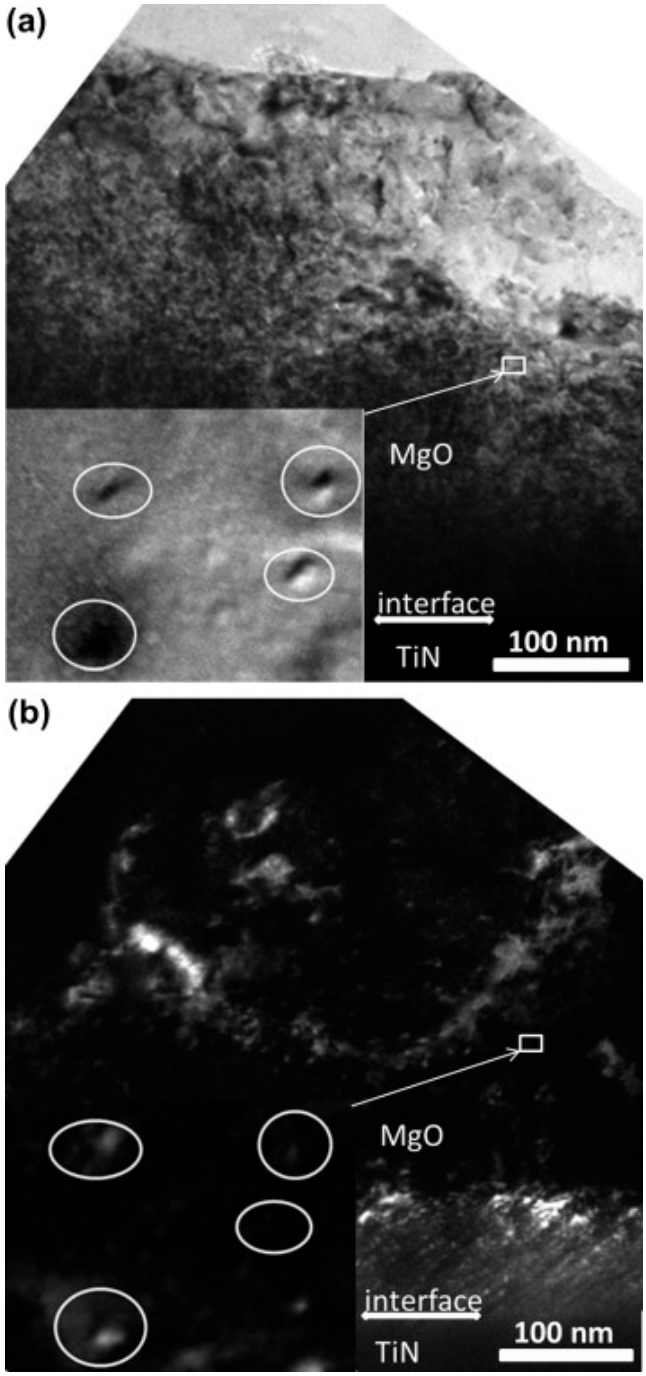

Figure 9 low magnification XTEM micrographs of the ion-irradiated MgO single layer films with He^{+} 50 keV ions at a dose of 4×10^{16} cm^{-2}, (a) bright field and (b) dark field images taken in the area about 230 nm from the surface showing the defects clusters with sizes around 5 nm. The insets in (a and b) are the enlarged TEM images to show the nature of the small point defect clusters.

The immobile tetra-interstitial and larger interstitial clusters could be the nucleus of interstitial dislocation loops [66]. However, no obvious dislocation loops or He bubbles were identified in the ion irradiated MgO single layer sample. Since the dose of implanted He is relatively low (the peak concentration of He is 0.62 cm^{-3} at 250 nm in MgO), it’s difficult to trace the exact locations of He ions in the film. It is highly possible that the He ions are trapped in the isolated vacancies in the film, and further stabilized the vacancies formed there [128]. Vacancies are considered immobile under current experiment condition in the first place, and after stabilized by the implanted helium, the tendency to aggregate to form voids and eventually bubbles is further reduced. Voids were not observed for the case of MgO after various kinds of irradiation even up to very high damage level [45]. At room temperature, the mobility of point defects could be relatively low [133]. Thus only small localized defect clusters are formed and no observable voids or helium bubbles were observed. Dislocation loops and dislocation networks have been previously reported in certain irradiated MgO samples after annealing [118].

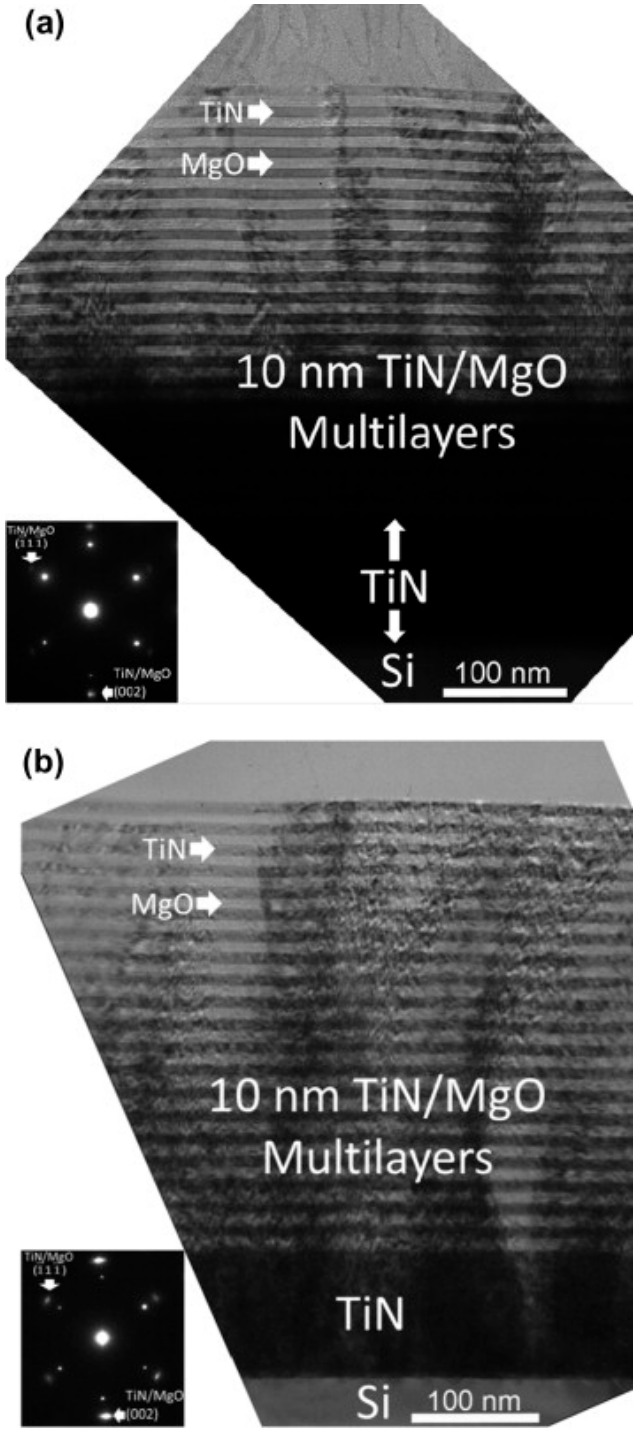

Figure 10 Low magnification bright field XTEM micrographs and selected area diffraction (SAD) patterns of 400 nm TiN/MgO nanolayer films, each individual layer is 10 nm, with 100 nm TiN seed layer on Si (0 0 1) substrate, (a) as-deposited and (b) ion-irradiated with He^{+} 50 keV at a dose of 4×10^{16} cm^{-2}.

Compared with the single layer MgO case, no such obvious point defect clusters and other related damage were found in all the nanolayer samples. Taking the 10 nm TiN/MgO nanolayer sample as an example, as shown in Fig. 10, the interfaces between the TiN layers and MgO layers are distinguishable and clean with some minor local intermixing for the irradiated sample. Cross-section high resolution TEM images of both the as-deposit one (Fig. 11 (a)) and the irradiated one (Fig. 11 (b)), taken from the middle range of the nanolayers where the peak damage was observed in the MgO single layer case, show clear lattice fringes in TiN and MgO layers and sharp interfaces with no visible defect clusters. Moreover, the diffraction pattern shows no obvious variation after irradiation. Similar to the 10 nm sample, the 20 nm/ 20 nm and 50 nm/ 50 nm samples also show no or very minor microstructure variation based on TEM studies (not shown here). The enhanced ion irradiation tolerance properties in the nanolayer samples are evident compared to the MgO single layer ones.

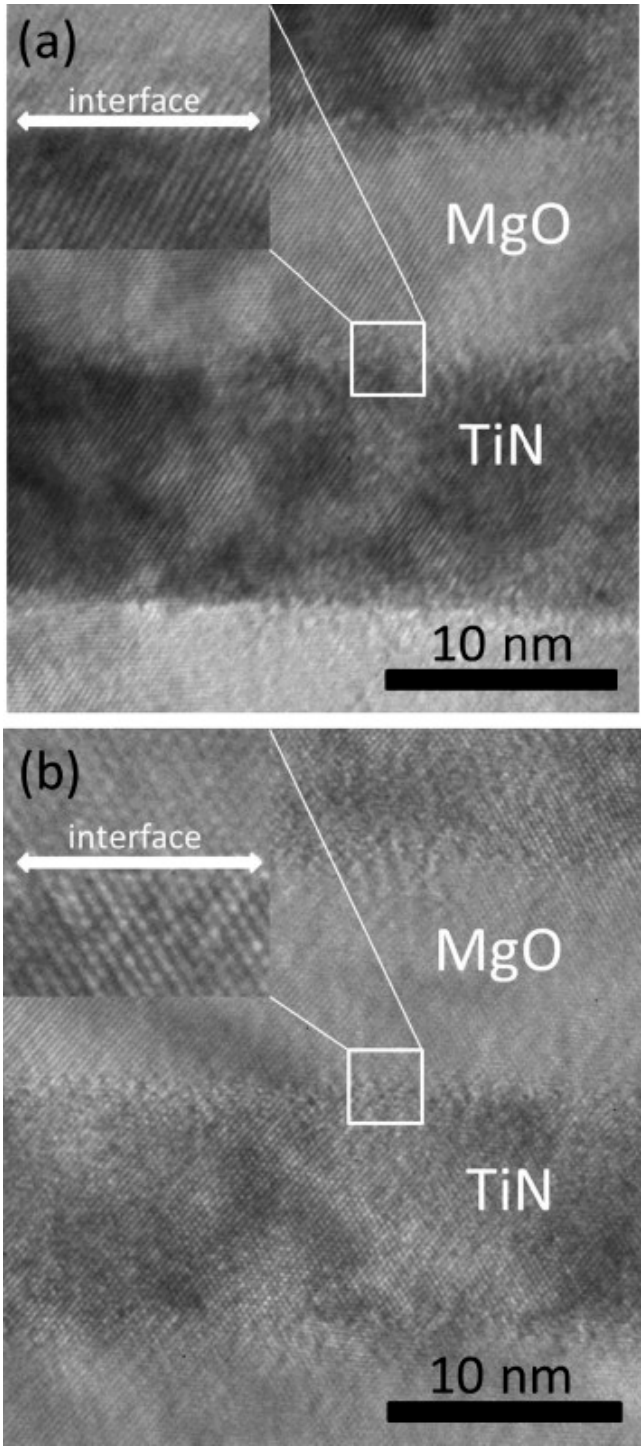

Figure 11 HRTEM micrographs of TiN/MgO 10 nm nanolayer sample taken from the depth of 200 nm with insets are the zoomed in images from which lattices are clearly shown: (a) as-deposited and (b) ion-irradiated with He^{+} 50 keV ions at a dose of 4×10^{16} cm^{-2}.

Besides the systematic microstructural analysis, a detailed mechanical properties measurement was conducted for all the samples. Hardness values before and after ion irradiation as a function of nanolayer thickness are plotted in Fig. 12. For each sample, more than 60 data points were collected and averaged. The error estimation was based on the standard derivation as well as the equipment errors. Regardless of the errors for the measurements, the hardness variation is obvious for both the as-deposited and the ion implanted films. There is a minor hardness reduction (~5%) in the single layer TiN film after irradiation, whereas a ~20% hardness enhancement was observed in the single layer MgO film. However, for all the nanolayer cases, no obvious hardness variation was found between the before and after ion irradiation samples. This is consistent with the TEM observation where no obvious microstructure variation (e.g., the formation of point defect clusters) was observed in all the nanolayer samples after ion irradiation in contrast to the high density defect clusters observed in the single layer MgO samples. Both of the hardness values for the nanolayer samples before and after irradiation follow the same trend, i.e. the hardness increases with decreasing the nanolayer thickness. Based on the model by Chu et al, when the individual layer thickness is relatively large, similar to the thickness range in this study, the mechanical behavior of multilayer films follow a similar trend as the Hall-Petch relationship, i.e., the nanolayer thickness decreases, the yield strength or hardness increases [134]. A minor hardness reduction could be seen for the 10 nm and 20 nm samples after irradiation. However, the reduction is still within the standard deviation of the hardness data.

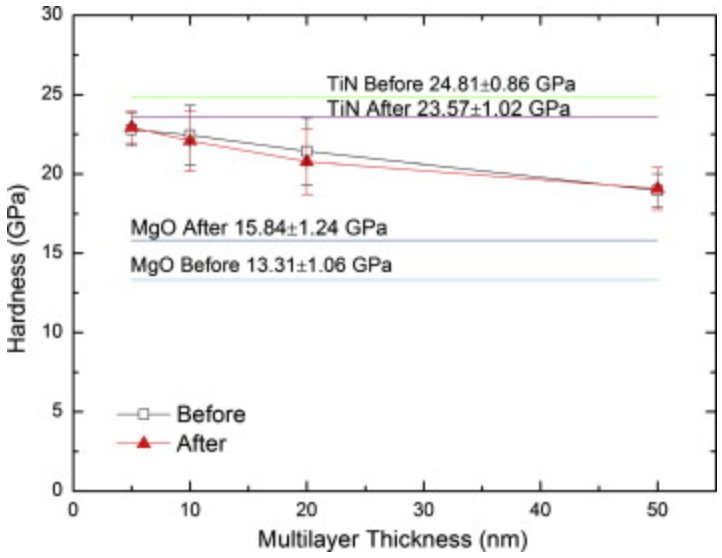

Figure 12 Averaged hardness vs. nanolayer thickness for as-deposited and ion-irradiated TiN/MgO nanolayer films. Hardness variation of single layer of TiN and MgO is plotted for comparison as well.

Enhanced ion irradiation tolerance properties in these nanolayer sets are evident based on the above microstructure and mechanical studies. Defect clusters are clearly shown in the irradiated single layer MgO, and the density of defects increases with the implantation depth. A similar phenomenon in various bulk ceramics was observed and reviewed by Zinkle [61], where a nominal defect free zone exists near the surface and defect sinks, and defect clusters with moderate to high density were only found around the peak ion implanted region. The irradiation induced hardening in MgO was commonly observed, and the mechanism was based on defect hampered slip [43, 58, 63]. One possible mechanism for the helium irradiation induced damage in ceramics is that the implanted He ions stabilize the immobile vacancies and prevent their annihilation with interstitials, and therefore the mobile interstitials aggregate to form defect clusters. This possibly leads to that those clusters were only found around the regions with the

highest concentration of implanted ions. For the nanolayer cases, TiN and MgO are quite different materials, provided they both possess NaCl structure and close lattice constants. The lattice parameters are: a_{TiN}=0.426nm and a_{MgO}=0.419nm in this as-deposited film measured by XRD, the measurement form the high resolution TEM is consistent with this value. Therefore, the lattice mismatch is 1.7%, and the nominal mismatch dislocation spacing is around 6nm along the interface. The dislocations along interfaces could be sinks to trap those point defects as well as those implanted He ions. It was reported that the bubbles prefer to aggregate along grain boundaries and interfaces [135]. With the lower concentration near interfaces, vacancies cannot be stabilized, and therefore the annihilation with interstitials increases. In addition, interstitials are attracted towards interfaces so that the accumulation is hindered. Therefore the nanolayered samples show obvious enhanced ion irradiation tolerance properties than their bulk counter parts, e.g., single layer MgO layer for this study. A concern may be raised on the effect of TiN layers since TiN itself is considered as a robust radiation tolerance material. However, the contribution from TiN is considered to be minor compared with the dominant interfacial effect. This is because that no hardness variation was observed in all the nanolayer samples with various nanolayer thicknesses, i.e., the sample with thinner TiN nanolayers show a similar enhanced radiation tolerance effect as the samples with thicker TiN nanolayers. Further experiment is ongoing to differentiate the contributions from the TiN layers and the heterogeneous interfaces. Another question remains is on which type of interfaces is more effective for mitigating ion irradiation damages. In this study, MgO and TiN nanolayer system with small lattice

mismatch is selected for this study based on the excellent epitaxial growth of the MgO/TiN nanolayers to minimize the possible contribution from high angle grain boundaries. Even with high quality epitaxial growth of MgO and TiN nanolayers, various heterogeneous interfacial defects including misfit dislocations and associated interfacial strains still exist and all contribute to the mitigation of the ion irradiation induced damages that leads to the enhanced radiation tolerance properties. Another possibility is the interfacial charge redistribution and differences in mobility and chemical potential might attract the point defects towards the interfaces, and therefore those defects could be annihilated there [136, 137]. More detailed studies are undergoing to explore the interface induced mitigation effects. Nevertheless, this work gains important fundamental understanding of interface behavior under ion irradiation in MgO-based ceramics, enlightens future nanostructured ceramic design, and shows a great potential to enhance the ion irradiation tolerance properties of MgO-based ceramic materials with nanostructure designs for future nuclear applications.

3.5 Conclusion

The radiation tolerance properties of MgO can be enhanced by introducing nanolayer interfaces, e.g., TiN nanolayers. The nanolayer thickness ranging from 5 nm to 50 nm is tested for radiation tolerance properties for this typical system. No hardness reduction or increase due to ion irradiation induced damage was observed in all nanolayered samples, compared to the obvious hardening in single layer MgO film. High

resolution TEM study shows no obvious damages in all the nanolayer samples, i.e., high epitaxial quality and clear interfaces remain after ion irradiation. These results strongly support that, interface effect could be a dominant factor in enhancing the ion irradiation tolerance properties of the MgO/TiN system in this study.

CHAPTER IV

RADIATION TOLERANT NANOCRYSTALLINE ZRN FILMS UNDER HEAVY IONS IRRADIATION[*]

4.1 Overview

ZrN, a refractory ceramic material, finds many potential applications in advanced nuclear reactors. However the grain size dependent radiation response in nanocrystalline (nc) ZrN under high dose heavy ion irradiation has not yet been studied to date. Here we compare the radiation response of nc-ZrN films (with a respective average grain size of ~9 and 31 nm) to Fe^{2+} ion irradiations up to a damage level of 10 displacements-per-atom (dpa). The ZrN film with the average grain size of 9 nm shows prominently enhanced radiation tolerance as evidenced by suppressed grain growth, alleviated radiation softening, as well as reduced variation in electrical resistivity. In contrast, ZrN with the larger average grain size of 31 nm shows prominent radiation softening and resistivity increase, attributed to the high density of defect cluster formed inside the grains. The influence of grain boundaries on enhanced irradiation tolerance in nc-ZrN is discussed.

---

[*] This chapter is reprinted with permission from Jiao, L., et al., *Radiation tolerant nanocrystalline ZrN films under high dose heavy-ion irradiations.* Journal of Applied Physics, 2015. **117**(14): p. 145901. Copyright (2015), AIP Publishing LLC.

4.2 Introduction

Nitride-based nuclear fuels have been proposed for next generation nuclear energy systems, owing to their high thermal conductivity compared to actinide oxides, high actinide density, and simple phase equilibria [138]. Among most nitrides, ZrN is one promising candidate for inert fuel matrices because of its high melting point, superior hardness, low vapor pressure, high thermal conductivity and excellent compatibility with nitride based nuclear fuels and zirconium cladding alloys. In addition, ZrN forms a solid solution with the fuels and act as the inert matrix to lower the high fission density [30]. In addition, nitride-based fuels with inert fuel matrices have the potential of proliferation resistance, and the idea of recycling of actinides is well established by reprocessing this form of nuclear fuel because of the solubility of ZrN in nitric acid. Thus the environmental impact could also be alleviated by reducing the long-lived radiation sources [78]. ZrN has also been used as a model material to evaluate and characterize the irradiation response of nitride based nuclear fuels because of its similarity in crystal structure (NaCl-type) and chemistry to many actinide mono-nitrides [2].

Despite its great potential, there are only handful studies [78-81] exploring the radiation response of ZrN, with mostly promising results. For example, bulk ZrN has demonstrated promising tolerance to low-energy, light or heavy ion irradiations:

Irradiation under 2.6 MeV proton at 800 ^{o}C showed no amorphization or precipitates, and no voids or bubble formation were detected at a dose of 0.75 dpa. The irradiated microstructure mainly consisted of a high density of dislocation loops and point defects, and some of the loops were of vacancy-type in nature [78]. Xenon and krypton were used in another radiation study at 300 keV up to 200 dpa under cryogenic and elevated temperatures. No amorphization was observed at low temperatures, and nor was bubble formation detected at elevated temperatures [80]. Nanocrystalline (nc)-ZrN remained intact after various types of swift heavy ion irradiations, such as 167 MeV Xe, 250 MeV Kr, and 695 MeV Bi [83]. Blistering tends to occur in annealed nc-ZrN irradiated with hydrogen or helium, but is suppressed by swift heavy ion irradiation of Xe at 167 MeV following the helium irradiation, the mechanism is attributed to swift heavy ion induced epitaxial crystallisation [79]. There is little systematic, in-depth study on grain size dependent radiation damage in nc-ZrN.

In general nc metallic and ceramic materials have abundant grain boundaries (GBs), which are effective defect sinks for radiation induced point defects. Molecular dynamics (MD) simulations show that GBs in Cu can absorb and then reemit interstitials in to grain interior to combine with vacancies in close proximity to high angle GBs [98]. The GB sink strength appears to increase with increasing misorientation angle in Cu as revealed by the change in width of GB denuded zones [99]. Wang et al. shows that nc-TiN with an average grain size of 8~100 nm showed greater radiation tolerance than its coarse grained counterpart, as evidenced by the diminishing damage zone subjected to He ion irradiations [93]. Similarly nc metals [100-102] have shown enhanced radiation

tolerance. *In situ* studies on nc-Ni show that high angle GBs can effectively capture and annihilate defect clusters and dislocation segments [100].

Other defect sinks, such as layer interfaces, have been increasingly investigated to absorb radiation induced point defects and their clusters [103-106]. There are limited studies on radiation response of nitride based multilayers. In a He ion irradiated study on MgO/TiN multilayer, the suppression of defect accumulation was shown in the MgO layers, whereas a high-density of defect clusters were identified in the single layer MgO film. In parallel, in AlN/TiN systems, no amorphization was seen in AlN layers of the AlN/TiN multilayers, while an obvious amorphized layer was identified in the single layer AlN film [107, 108], which actually result in higher amount of interfaces and thus better radiation tolerance properties.

In this study, 900 keV Fe^{2+} ions up to a fluence of 6×10^{15} cm^{-2} were implanted in nc-ZrN films with selected grain sizes. The influences of grain boundary on radiation response were carefully studied by exploring in detail the evolution of microstructures, mechanical and electrical properties. Mechanisms of enhanced radiation tolerance in nc-ZrN are discussed.

4.3 Experimental

Pulsed laser depositions of nc-ZrN thin films were performed in a high vacuum chamber with a KrF excimer laser (Lambda Physik 210 with wavelength of 248 nm, at a frequency of 10 Hz). ZrN target was a hot-pressed stoichiometric target obtained from

Plasmaterials Inc. ZrN films with thickness of 500 nm were deposited at room temperature (RT), 200, 500 and 700 ^{o}C on Si (100) substrates, and are referred to as RT-dep, 200-dep, 500-dep, and 700-dep ZrN films, respectively, throughout the text. Before deposition, the Si substrates were cleaned using acetone, methanol, and etched in a diluted HF solution to remove the oxidation surface layer. RT-dep and 500-dep films were then irradiated at room temperature with 900 keV Fe^{2+} ions at a 40^{o} incidence angle to a fluence of 6×10^{15} ions/cm^2, and the irradiated samples are referred as RT-dep/rad and 500-dep/rad hereafter. A depth dependent damage profile was provided by the stopping and range of ions in matters (SRIM) simulation [7] by using Kinch-Pease method. Following ion irradiation, microstructural evolution of the as-deposited and post-irradiated films was characterized by transmission electron microcopy (TEM) using an FEI Tecnai G2 F20 ST analytical transmission electron microscope with a point-to-point resolution of 0.24 nm. Lattice parameters, strain and stress were analyzed by grazing incidence X-ray diffraction (GIXRD) scan with a grazing angle of 1^{o} using a PANalytical Empyrean facility.

Hardness of all the as-deposited and irradiated films was measured with Hysitron Tribo-nanoindenter. The measurement was performed using a standard Berkovich diamond tip using a quasi-static approach under a constant peak load mode with the load varied from 4000 to 7000 μN. Different contact depth was chosen for each sample to avoid surface and substrate effects. The contact depth was strictly controlled to less than 20% (~100 nm) of the total film thickness. A plateau of hardness is typically observed around contact depth of 60 nm, and these values were chosen as the average hardness of

the films for future discussion. Each hardness data point and its standard deviation are calculated based on at least sixteen indentation experiments per indentation depth. Calibration was done by using a standard fused quartz sample. An area function was obtained and applied in the measurements. Electrical resistivity of all the as-deposited and post-irradiated samples was measured by a four point probe method.

4.4 Results

The depth dependent Fe ion concentration and damage profile for 500 nm thick ZrN at an ion energy of 900 keV is calculated using the SRIM code [7]. As shown in Fig. 13, the peak damage reaches 10 dpa at a depth ~ 160 nm from the surface, whereas the maximum Fe^{2+} ion concentration is only ~ 0.45 at.% at 350 nm underneath film surface. The major of film is subject to a damage level above 5 dpa throughout the film. GIXRD scans of RT-dep/rad and 500-dep/rad in Fig. 14 show that irradiated films have a better crystallinity than as-deposited ones, as indicated by increasing peak intensity and narrower full width at half maximum (FWHM) of diffraction peaks. All of the as-deposited films have shown an out-of-plane lattice expansion, indicated by the left shift of peak positions from the standard bulk reflection positions (marked by the vertical dash lines). After irradiation, diffraction peaks in both films have migrated towards the dash lines. Furthermore the peak position in RT-dep/rad sample almost returns to the bulk value.

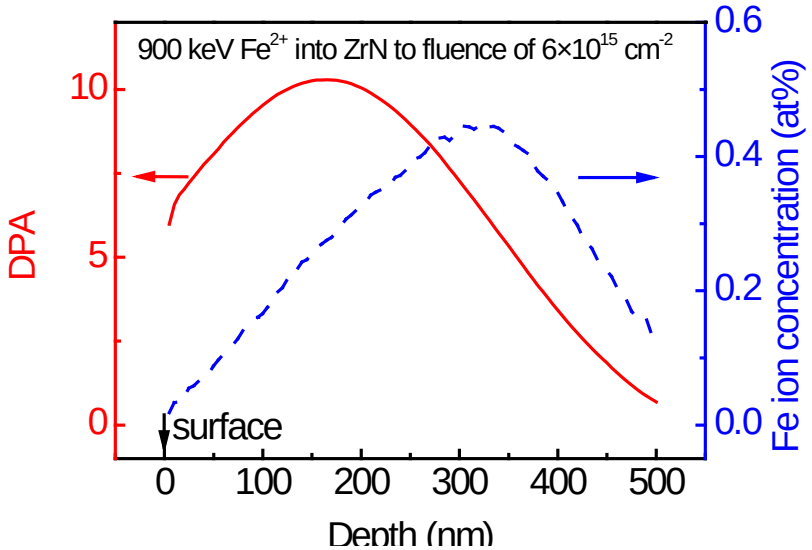

Figure 13 SRIM simulation of depth dependent damage profile (solid line) and Fe concentration (dash line) of ZrN subjected to 900 keV Fe^{2+} ions to the fluence of $6\times10^{15}cm^{-2}$ at an incident angle of 40^{o}. Peak damage (10 dpa) occurs at 160 nm from the surface, whereas the peak Fe concentration (0.45 at. %) is at the depth of 350 nm.

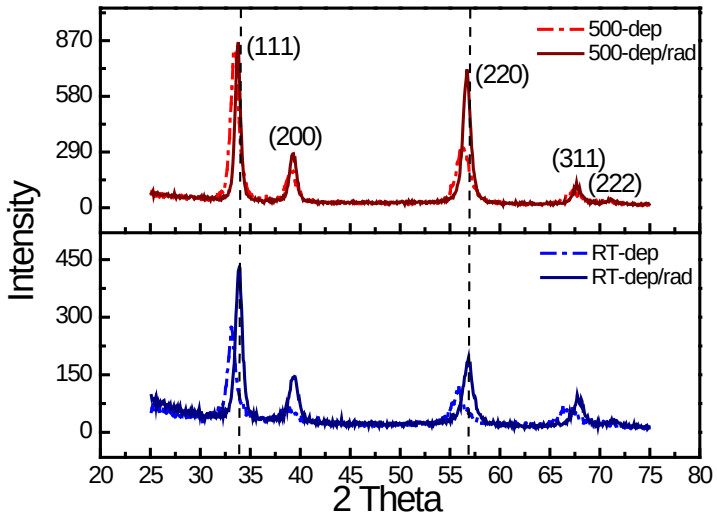

Figure 14 GIXRD profiles of as-deposited ZrN specimens at room temperature (RT-dep) and 500 ^{o}C (500-dep), and the corresponding irradiated specimens (RT-dep/rad and 500-dep/rad). The peaks of irradiated specimens (solid line) shift right as compared to the as-deposited films (dash line). The dotted lines show the standard reflections, indicating the existence of compressive stress in the as-deposited films and the reduction of the stress in the irradiated films.

Comparison of plan-view dark field (DF) TEM images in Fig. 15 a-b show that radiation has led to insignificant grain growth in RT-dep ZrN film, and the inserted selected area diffraction (SAD) patterns in both specimens contain continuous diffraction rings. However, a prominent grain coarsening is in 500-dep/rad specimen (Fig. 15 c-d). The significant grain growth has led to the dotted SAD pattern in Fig. 15 d. Grain size distribution statistics have been obtained by measuring at least 100 grains from each DF image, and the results are plotted in Fig. 15 e-h. The average grain size has grown from 9 nm (Fig. 15 e) in RT-dep film to 12 nm (Fig. 15 f) in RT-dep/rad film, whereas the grain size increases from 31 nm (Fig. 15 g) in 500-dep film to 62 nm (Fig. 15 h) in 500-dep/rad film. The standard deviation increases as the grain size increases.

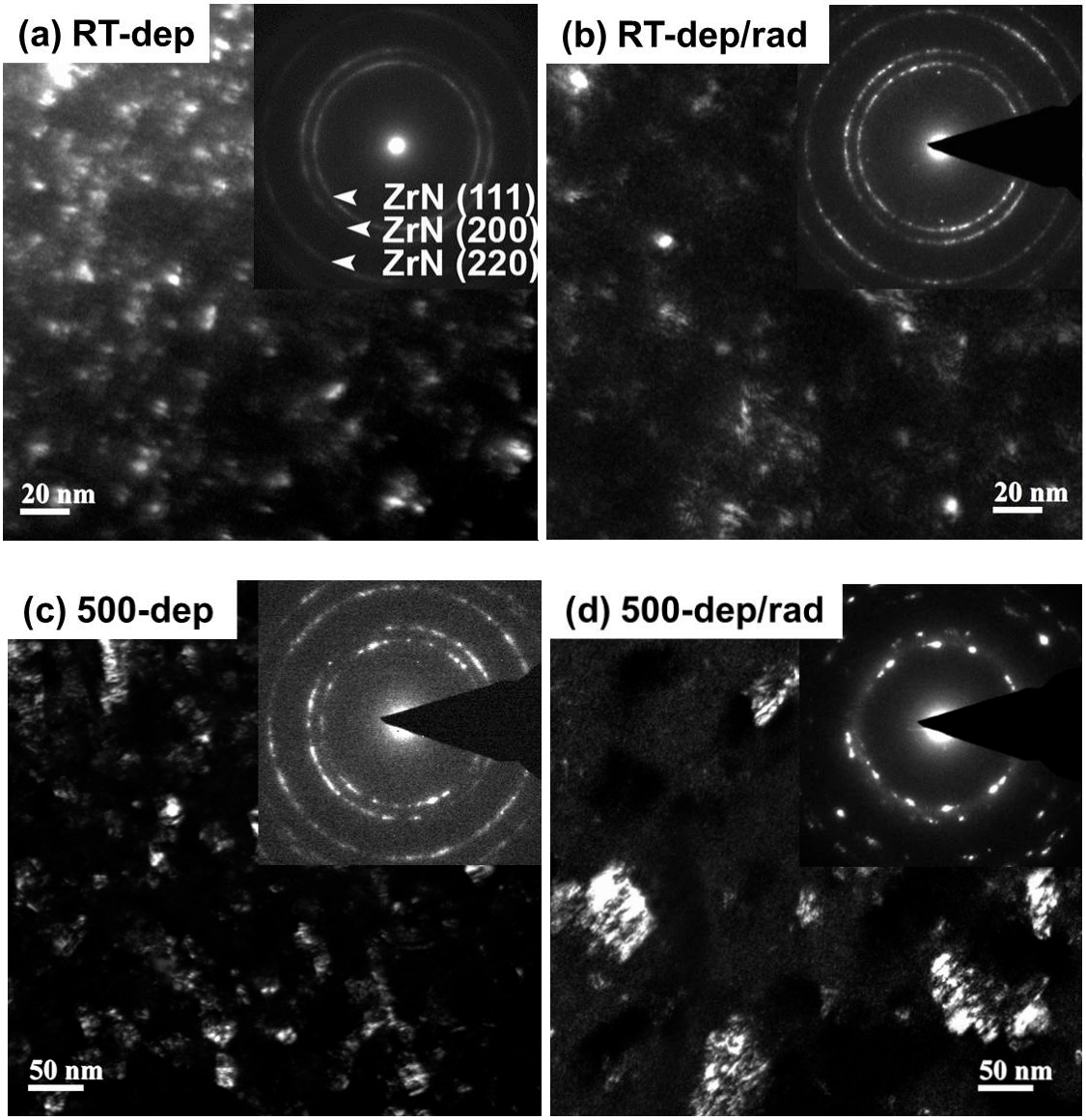

Figure 15 Plan-view dark field TEM images illustrating radiation induced grain growth in ZrN films. (a) RT-dep ZrN film had nano-grains and the inserted selected area diffraction (SAD) pattern shows continuous ring. (b) RT-dep/rad ZrN film had slight increase in grain size and insignificant variation of diffraction pattern. (c) 500-dep ZrN had larger grain size and discontinuous arcs in SAD pattern. (d) 500-dep/rad ZrN had prominent grain coarsening and dotted diffraction pattern. Grain size frequency distribution charts clearly show the gran size and standard deviation statistics in (e) RT-dep ZrN film, (f) RT-dep/rad ZrN film, (g) 500-dep ZrN film, (h) 500-dep/rad ZrN film.

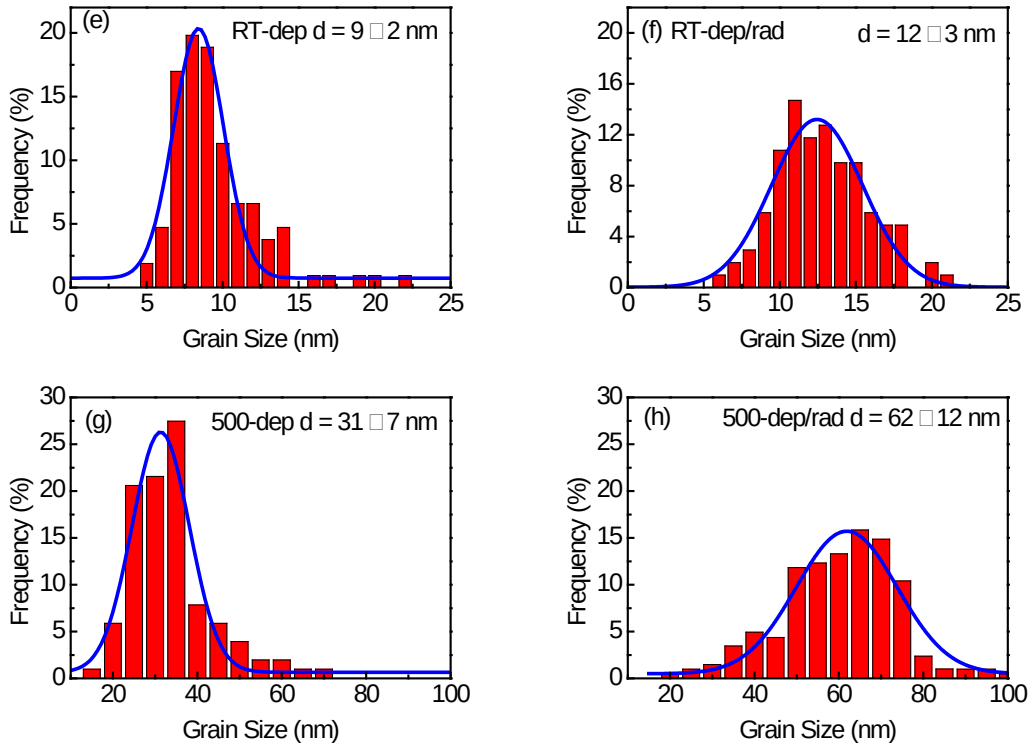

Figure 15 Continued.

Defect clusters have been identified in both irradiated films. A very low density of defect clusters was observed in RT-dep/rad ZrN film, and they are mixed with Moiré fringes (due to overlapping of nanograins), as shown in Fig. 16 (a1) and high resolution TEM (HRTEM) micrograph in Fig. 16 (a2). Whereas a higher density of defect clusters have been observed within the grains of 500-dep/rad film. The columnar grain/domain boundaries are labeled in Fig. 16 (b1). The density of defect clusters increases with

depth into the film. HRTEM micrograph revealed two types of typical regions, with and without defect clusters. The inverse fast Fourier transformed (IFFT) filtered image for the box in clear lattice region shows little distortion. In contrast, the IFFT of defected regions shows the highly distorted (200) planes containing various types of defect clusters (including vacancy (red) and interstitial (yellow) loops and other types of defect clusters (circled in green).

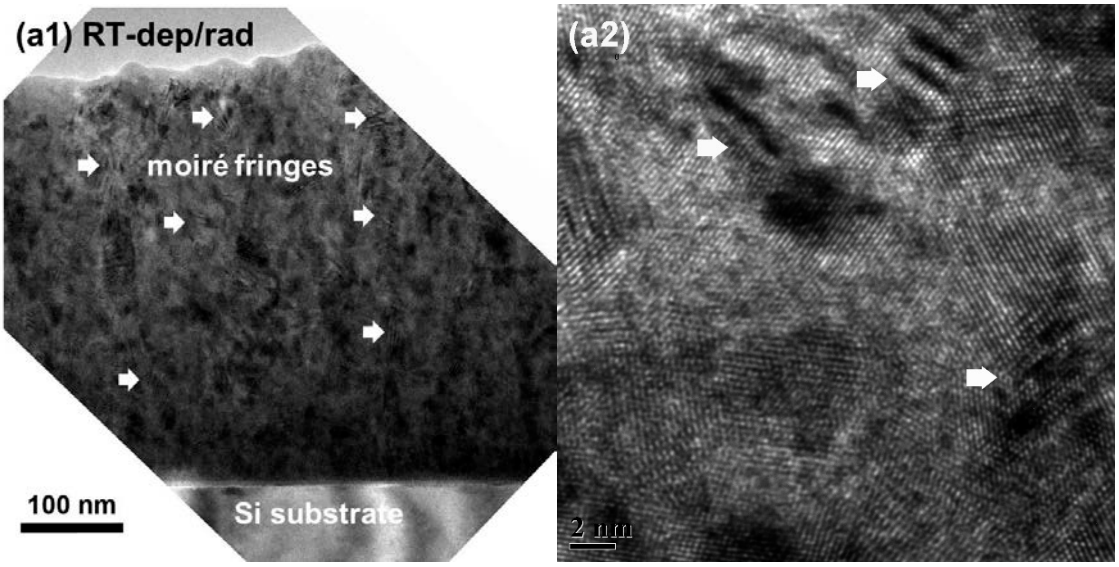

Figure 16 (a1) Bright field TEM image of RT-dep/rad ZrN with arrows indicating moiré fringes generated by overlapped grains, (a2) HRTEM of RT-dep/rad ZrN, showing the low density of defect clusters mixed with moiré fringes, (b1) TEM image of 500-dep/rad ZrN. The dashed white lines are columnar grain boundaries, and the high density of defect clusters inside grains is shown. (b2) HRTEM image of 500-dep/rad ZrN showing the high density of defect clusters. Inverse FFT of the boxed areas of a clear lattice position showing clear (200) displacing (up box and IFFT), and another position around a defect cluster (down box and IFFT) showing highly distorted (200) planes with mask applied on (200) diffraction spots, both interstitial and vacancy type loops as well as many other dislocations can be found as marked out.

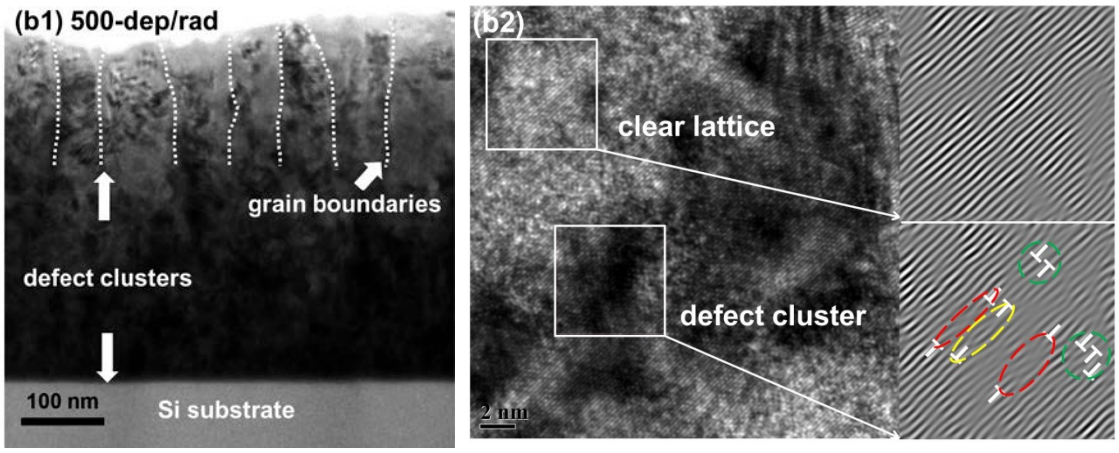

Figure 16 Continued.

The hardness of all the as-deposited and irradiated samples vs. the inverse square root of grain size d is plotted in Fig. 17. The dashed line indicates a clear inverse Hall-Petch relationship for all as-deposited films before irradiation. Among all the as-deposited films, RT-dep and 500-dep films were irradiated. Radiation induced softening for RT-dep/rad is, 1.5 GPa, less significant than that of 500-dep/rad film, 5.5 GPa).

The evolution of electrical resistivity showed a contrary behavior of RT-dep/rad and 500-dep/rad films compared with their unirradiated counterparts. Specifically radiation leads to the decrease of the resistivity of RT-dep films by 26%, whereas the

resistivity of 500-dep/rad film is 78% greater than its unirradiated counterparts as plotted in Fig. 18.

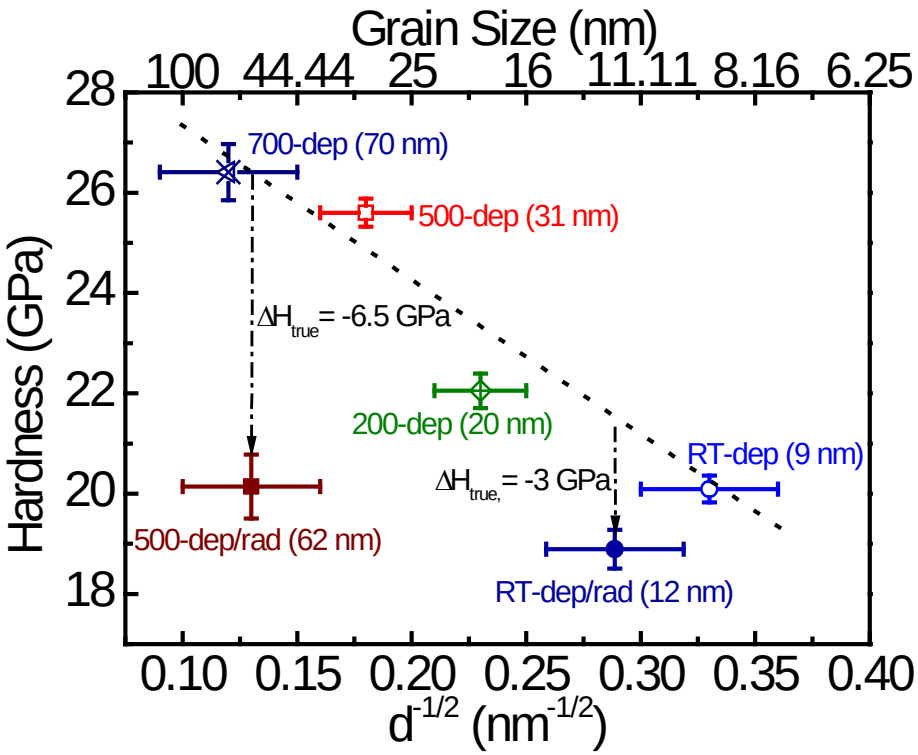

Figure 17 Hardness vs. the inverse of square root of grain size *d*, showing the inverse Hall-Petch effect of nc-ZrN before irradiation (data points with open symbols, the inverse Hall-Petch effect is outlined by the dashed line), and the true softening, ΔH_{true}, of samples after irradiation (data points with closed symbols).

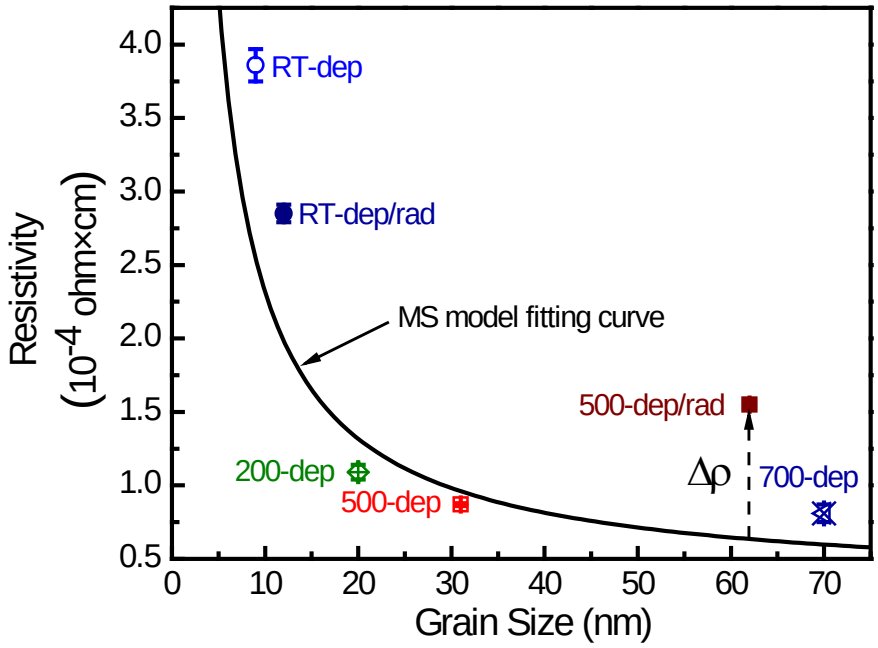

Figure 18 Correlation between average grain size and resistivity of ZrN films before and after irradiation. The scattered data was obtained by a four point probe measurement. And the curve was calculated by MS model.

4.5 Discussion

4.5.1 Microstructural Evolution

Radiation induced defects and their grain size dependence

No amorphization was observed in either of the irradiated films, while better crystallinity was shown in both films after irradiation. In irradiated coarse grained 500-

dep/rad ZrN films, various types of defect clusters have been observed. FFT filtered images of the films showed clear difference between the highly distorted (200) planes of the defective area and the straight (200) planes of the defect-free zone in Fig. 16 (b2). The lattice distortion can be attributed to the localized point defect clusters. Both interstitial- and vacancy-type loops can be identified. Additionally there are other types of defect clusters identified in the irradiated specimen, marked in green dashed circles, wherein clusters of dislocations with opposite signs are identified. Similar defect clusters were reported by Yong et al. in bulk ZrN with large grains (several microns) irradiated by 2.6 MeV protons at 800 ^{o}C, and were speculated as vacancy-type pyramidal dislocation loops [78]. Since the HRTEM images in the current study only provide the 2D projection of these defect clusters, future research is needed to further identify the nature of these defects.

In comparison to coarse grained ZrN films, the defect cluster density in RT-dep/rad film with smaller grain sizes is much lower. There are several mechanisms that may lead to enhanced size dependent radiation tolerance. First, it is likely that a large number of nitrogen interstitials and vacancies are attracted to grain boundaries whereby they annihilate with one another. Although at room temperature vacancies are considered less mobile in ZrN, they may have much higher mobility in the vicinity of grain boundaries [93]. Second, a recent simulation study has suggested that, in irradiated polycrystalline MgO, the interaction between defects and grain boundaries are very strong, and became even stronger when the boundaries were damaged. When the MgO grain boundaries were loaded with excess interstitials to mimic the damage in irradiated

polycrystalline MgO, depending on the atomic structure of boundary, in some cases, the vacancies formation energy at or close to the grain boundaries were drastically decreased, that the vacancies can be spontaneously annihilated with the interstitials at the grain boundaries or at sites close to the grain boundaries [67]. This interstitial emission mechanism is similar to the one reported in metal [98, 139]. Such mechanisms might be applicable in ZrN in this study as ZrN and MgO has similar crystal structure. Third, it is likely that some defect clusters are absorbed by grain boundaries. A recent *In-situ* radiation studies on nanocrystalline Ni shows that defect clusters, ~ several nm in diameter, can be captured by high angle grain boundaries.

Radiation induced grain growth

Radiation induced grain growth has been studied in nanocrystalline metals, such as FeZr [140]. In general the smaller grains are vulnerable to grain growth as the density of high angle grain boundaries and hence driving force for grain coarsening is much greater than counterparts with larger grains. Hence it is natural to anticipate more prominent grain growth in RT-dep/rad ZrN film than in the 500-dep/rad film. Surprisingly, the average grain size in the RT-dep/rad film,only increased from 9 to 12 nm, by 33%, while the grain size grew significantly in the 500-dep/rad film, from 31 to 62 nm, by 100%. Radiation induced grain growth is in general related to the density of radiation induced defect clusters. A higher density of defect clusters, observed in 500-dep/rad film may accelerate grain coarsening.

4.5.2 Size Dependent Alleviation of Irradiation Softening

Irradiation induced hardening is a universal phenomenon in metallic materials and is typically attributed to increasing resistance to the propagation of dislocations by irradiation induced defect clusters [78, 80]. Irradiation induced hardening is also frequently reported. For instance the hardness of MgO thin films irradiated by helium ions was found to increase by 20% [107]. However, in this study, radiation induced prominent softening in ZrN films as shown in Figure 17 and Table 5. Irradiation softening has also been reported in TiN irradiated with He^+ ion [107]. The softening could be related to the generation of nitrogen vacancy since the displacement energy is lower in the anion sublattice, and nitrogen interstitials are mobile under irradiation. Additionally the magnitude of irradiation softening is ~ 1.5 GPa for RT-dep/rad, much lower than that in 500-dep/rad films, ~ 5.5 GPa.

Table 5 Residual stresses of various ZrN films measured using XRD profiles.

	out of plane strain ε_z	Modulus E (GPa)	In-plane residual stress relaxation ($\sigma_{res}^{irradiatted} - \sigma_{res}^{as\text{-}deposited}$) $\Delta\sigma_{res}$ (GPa)	Softening from relaxation ΔH_{relax} (GPa)	True softening ΔH_{true} (GPa)
RT-dep	2.08%	170 ± 10	6.64	-4.44	-3.0
RT-dep/rad	0.16%	170 ± 10			
500-dep	0.96%	200 ± 10	2.49	-1.65	-6.5
500-dep/rad	0.39%	170 +/- 10			

In order to better understand grain size dependent variation of irradiation softening, two complexities shall be taken into consideration, including grain growth and residual stress. First, grain growth may contribute to the hardness change. An inverse Hall-Petch effect was outlined by the dash line in Fig. 17, that is the smaller the grain size, the lower the film hardness. Such effect has also been reported in nc-ZrN previously [141]. As radiation induces grain coarsening in nc-ZrN films, the true softening in irradiated specimens should be estimated by comparing with as-deposited specimens with similar grain size. Given there is a linear dependence between film hardness and $d^{-1/2}$, the magnitude of true irradiation softening (ΔH_{true}) for RT-dep/rad specimen was estimated to be ~ 3 GPa, still much lower than that in 500-dep/rad ZrN films, ~ 6.5 GPa.

Second, residual stress in films could also change the measured film hardness. In general a compressive (tensile) residual stress would increase (decrease) film hardness [142-144]. XRD studies show that as-deposited films have compressive stress, whereas radiation leads to alleviation of residual compressive stress. Compressive stress is commonly observed in nanocrystalline films [81]. Relaxation of compressive stress will also result in softening. The in-plane residual stress, σ_{res} can be calculated using a biaxial stress model:

$$\sigma_{res} = -(E/2\,\nu) \times \varepsilon_Z$$

where, E is the Young's modulus, ν is the Poisson's ratio, and ε_z is the out-of-plane strain that can be measured from XRD experiments by using the (111) diffraction. Young's modulus of films is measured from nanoindentation experiments. The measured

values of E and ε_z, and calculated residual stresses are listed in Table 5. The in-plane compressive stress is commonly seen in PVD deposited nanocrystalline films [81].

The equibiaxial residual stress consists of a plastic-deformation independent hydrostatic stress component σ_H and a plastic-deformation sensitive shear deviatoric stress σ_D [142]:

$$\sigma_{res} = \sigma_H + \sigma_D$$

and the corresponding 3D expression in matrix would be:

$$\begin{Bmatrix} \sigma_{res} & & \\ & \sigma_{res} & \\ & & 0 \end{Bmatrix} = \begin{Bmatrix} \frac{2}{3}\sigma_{res} & & \\ & \frac{2}{3}\sigma_{res} & \\ & & \frac{2}{3}\sigma_{res} \end{Bmatrix} + \begin{Bmatrix} \frac{1}{3}\sigma_{res} & & \\ & \frac{1}{3}\sigma_{res} & \\ & & \frac{-2}{3}\sigma_{res} \end{Bmatrix}$$

The term σ_D has a component along the out-of-plane direction, $-2/3\sigma_{res}$, which directly results in the hardness increment [142]. The hardness increase induced by residual compressive stress could thus be estimated as:

$$\Delta H_{res} = -\frac{2}{3}\sigma_{res}$$

Consequently irradiation softening due to the relaxation of residual compressive stress can be estimated from the variation in residual stresses of the films before and after irradiation:

$$\Delta H_{relax} = -\frac{2}{3}\Delta\sigma_{res} = -\frac{2}{3}(\sigma_{res}^{irradiated} - \sigma_{res}^{as-deposited})$$

The calculated results are listed in Table 5, and the true softening, ΔH_{true}, is also listed for comparison. For RT-dep/rad film the estimated ΔH_{relax} is -4.44 GPa, which is

comparable to the measured ΔH_{true} (-3.0 GPa). Therefore the irradiation softening in RT-dep/rad ZrN film may be primarily caused by the significant stress relaxation. On the other hand, for the 500-dep/rad film ΔH_{relax} is estimated as -1.65 GPa, much lower than the ΔH_{true}, ~6.5 GPa. Hence the relaxation of residual stress alone cannot completely account for the measured radiation softening. Such prominent irradiation softening in 500-dep/rad ZrN films with larger grain size could be attributed to the much higher density of defects induced by radiation. The accumulation of vacancies and their clusters could significantly reduce the bonding strength between Zr and N and lead to substantial irradiation softening, as reflected by the reduction of the Young's modulus from 200 to 170 GPa.

4.5.3 Size Dependent Variation of Electrical Resistivity in Irradiated ZrN Films

Electrical resistivity of materials is sensitive to defects density. The electrical resistivity of irradiated metallic materials is typically greater than their unirradiated counterparts as radiation often significantly increase the density of point defect and their clusters. Radiation leads to anticipated prominent increase in electrical resistivity in the 500-dep/rad ZrN films. However the opposite phenomenon is observed in RT-dep/rad ZrN film irradiated at the same condition: that is radiation induces a decrease in electrical resistivity. To understand this unusual phenomenon, we need to first understand the influence of grain size on electrical resistivity of solid materials.

The model proposed by Mayadas and Shatzkes (M-S model) [145] correlates average grain size to electric resistivity of solid materials. This model has been successful applied to explain size effect on electrical resistivity of various metallic materials [146, 147]. Here the model is adopted as ZrN has high conductivity (comparing to most ceramic materials) and metallic type of electrical transport properties. In the M-S model, grain boundaries are considered as major obstacles that scatter charge carriers, and thus increase the overall resistivity. The enhanced resistivity ρ can be described as follow:

$$\rho = \rho_o \left[1 - \frac{3}{2}\alpha + 3\alpha^2 - 3a^3 \ln\left(1 + \frac{1}{\alpha}\right) \right]^{-1}$$

where, ρ_o is the intrinsic resistivity, ~30 μΩ • cm for ZrN. α is the scattering parameter, and can be calculated by:

$$\alpha = \frac{\lambda}{d} \frac{R}{1-R}$$

where λ is the electron mean free path, d is the average grain size, and R is the reflection coefficient for carriers striking a grain boundary, which is typically in the range of 0.2 – 0.5. [148]. λ is chosen as 50 nm, similar to TiN, as the ZrN and TiN has very similar chemical and physical properties [149].

By using R = 0.5, a solid line generated by the M-S model is generated in Fig. 18, which captures the major trend for a majority of data for as-deposited and irradiated ZrN films. The comparison (between experimental results) and modeling implies that the

reduction of electrical resistivity in RT-dep/rad ZrN film is mainly due to radiation-induced grain coarsening. However it's worth noting that the resistivity of 500-dep/rad sample has a significant deviation from the M-S model, that is radiation induces an increase of resistivity by ~ 78%, although the grain size of the films has doubled. Such prominent increase in resistivity of 500-dep/rad Zr film could be attributed to the high density of defect clusters in these irradiated films. These defect clusters and lattice distortion scatter electrons more frequently [150]. Therefore, the relation for estimation of electron scattering parameter, α, could be revised as follows:

$$\alpha = \frac{\beta\lambda}{d}\frac{R}{1-R}$$

where, a new factor, β, is introduced to describe how many times electrons are scattered by defect clusters or lattice distortions within a grain. And from the measured resistivity for 500-dep/rad ZrN films, β is estimated to be ~ 5. This simplified estimation implies that the distortion caused by defects and their clusters, regardless of the dramatic grain growth in 500-dep/rad sample, scatter electrons ~5 times more frequently than that in unirradiated films.

4.6 Conclusion

The heavy ion irradiation response of nc-ZrN films, with an average grain size of 9 nm and 31 nm show clear grain size dependences. The RT-dep/rad ZrN film with a

smaller average grain size has much lower density of defect clusters than that in the 500-dep/rad ZrN with a larger grain size. Furthermore smaller grains appear to effectively curtail grain growth, mitigate irradiation softening and irradiation induced variation of electrical resistivity. This study suggests the abundant high angle grain boundaries in ZrN can significantly boost the radiation tolerance of irradiated ZrN as manifested by stability of microstructure and mechanical and electrical properties, and hence increase the odds for applications of nc ZrN as promising fuel clads for advanced nuclear reactors.

CHAPTER V

IN-SITU IRRADIATION STUDY OF MGO BASED MULTILAYERS: GRAIN BOUNDARY AND INTERFACE EFFECTS ON RADIATION DAMAGE DEVELOPMENT

5.1 Overview

The mitigation effect of grain boundaries and interfaces were investigated via *in-situ* Kr^{2+} irradiation. The results are that both epitaxial interfaces and non-epitaxial interfaces were identified as defect sinks, with the polycrystalline like non-epitaxial interfaces acting more efficiently. Grain boundaries were found to be both the initiation site and annihilation site of defects, and a cyclic accumulation and removal of defects by grain boundaries were first observed. The mechanisms were attributed to the kinetic evolution of grain boundaries and their influence on different type of defect clusters. Grain growth was observed as the results of radiation enhanced diffusivity, and high mobility of the charge-neutral interstitials.

5.2 Introduction

MgO has been widely studies for decades both experimentally and computationally. First of all, MgO is relative simple for study compared to more complex oxides, i.e., MgO has a simple rock salt structure, high melting temperature

close to 3000 ^{o}C, relatively high thermal conductivity compared with other well-studied refractory ceramics, such as ZrO_2, $MgAlO_4$, and Al_2O_3 [24]. And it's a well understood classic engineering ceramic. Due to its outstanding physicochemical properties, MgO has been of interest in a wide range of applications including protective coating in plasma display panels, catalysis, fuel cells and tunable broadband laser [9]. Moreover, it's compatible with reactor materials and has a low thermal neutron absorption cross-section [25], which make MgO an envisioned candidate for Inert Matrix Fuel (IMF) application, which could deal with the proliferation problems associated with the current fuel forms [24]. MgO also received attention as a material for immobilization and long-term nuclear waste storage, transmutation of high radioactive actinides, and proposed as insulators for fusion reactor diagnostics due to its neutron transparency, high thermal conductivity compared to other oxide materials, high resistance to high-energy particle irradiation [16-19]. Therefore the radiation tolerance of MgO is of significant importance, especially how the radiation induced damage accumulation in MgO, and how they interact with microstructure will provide guidance the microstructural design for applications mentioned above.

Ion irradiation damage in MgO has been extensively explored for decades [115]. However, MgO is sensitive to radiation damage, e.g., the irradiation hardening in MgO has been widely observed [116]. It is the result of hampered dislocation slip and solid-solution hardening. Very few work has been conducted to enhance the radiation tolerance of MgO. For example, the suppression of radiation damage of MgO has been reported by *Chen and Abraham* through Li doping [119]. However, the question remains

on whether extended defect clusters and accumulation can be suppressed by this approach.

Recently, radiation response of nanostructured materials have gained significant research interests due to the observed enhanced radiation tolerance properties in various nanomaterials including metals and ceramics. In general nano-crystalline (nc) metallic and ceramic materials have abundant grain boundaries (GBs), which are demonstrated as effective sinks for radiation induced point defects. Molecular dynamics (MD) simulations have shown that GBs in Cu can absorb and then re-emit interstitials into grain interior to combine with vacancies in close proximity to high angle GBs [98], and the sink strength increases with misorientation angle as revealed by the change in width of defects denuded zones close to GBs [99]. Wang et al. has reported that nc-TiN showed greater radiation tolerance than its coarse grained counterpart, as evidenced by the diminishing damage zone subjected to He ion irradiations [93]. Similarly nc-metals [100-102] have shown enhanced radiation tolerance. Moreover, Shen et al. provided a thermodynamic explanation of the grain boundary effects which could either enhance or harm the radiation tolerance depending on the grain sizes and the system chosen [124].

Other defect sinks, such as layer interfaces, have been increasingly investigated both experimentally and computationally, in absorption of radiation induced point defects and their clusters [103-106]. For example, Zhang et al. have reported that the immiscible interface acts effectively in reducing radiation damage, such as swelling, helium bubbles formation, and radiation hardening in several metallic multilayer systems, including Cu/Nb, Cu/V, Al/Nb, and Fe/W [120-123]. And Misra et al. reported

that the greatly reduced formation energy of interfacial point defects drastically drives the vacancies and interstitials formed in radiation cascade into the interface where they recombined in an atomic-scale simulation [125].

Nevertheless, similar studies on nanostructured or nanolayered ceramics were scarce [126]. There are limited studies on radiation response of nitride based multilayers. In a He ion irradiated study on MgO/TiN multilayer, the suppression of defect accumulation was shown in the MgO layers epitaxially grown between TiN layers, whereas a high-density of defect clusters were identified in the single layer MgO film counterpart. In parallel, in a He ion implanted AlN/TiN systems, no amorphization was identified in AlN layers of the AlN/TiN multilayers, while an obvious amorphized layer was observed in the single layer AlN film [107, 108], which are attributed to the higher amount of interfaces acting as defect sinks that prevent the defects accumulation or amorphization, and thus improve the radiation tolerance properties.

In this work, MgO-based nanolayered thin films with different layer thickness as well as different grain sizes have been synthesized to explore the grain boundary as well as interface mitigation mechanism on radiation induced defects accumulation in MgO. For this study, transition metal nitrides, ZrN and TiN, are chosen as the interlayer material due to their good radiation tolerance in addition to the outstanding mechanical properties and thermal stability and decent epitaxial growth of MgO can be achieved on TiN as the same crystal structure and close lattice parameter. Moreover, non-epitaxial MgO/ZrN multilayers were synthesized as they have bigger lattice constant difference (a_{ZrN} = 0.457 nm, a_{MgO} = 0.419 nm), and polycrystalline MgO layers with different grain

sizes were deposited by PLD via varying deposition temperature. The epitaxial MgO/TiN nanolayers synthesized in this study minimize the contributions from grain boundaries, and therefore provide a relatively clean model system to illustrate the epitaxial interfacial effects on irradiation damage. And the radiation response of polycrystalline MgO between ZrN layers is only influenced by the grain boundaries. And the damage behavior is affected both by grain boundaries and non-epitaxial interfaces in the thin MgO layers between ZrN. A preliminary comparison is made between the MgO/TiN epitaxial interface with the MgO/ZrN non-epitaxial interface in terms of the absorption speed of radiation induced defects.

5.3 Experiments

MgO based multilayer thin films were deposited by a pulsed laser deposition technique in a high vacuum chamber with a KrF excimer laser (Lambda Physik Compex Pro 205, λ = 248 nm). Laser beam was focused with an energy density of approximately 5 J cm^{-2} at an incident angle of 45^{o}. Targets were hot-pressed stoichiometric ZrN, TiN and MgO obtained from Plasma Materials, Inc. The nanolayer films were deposited at a typical growth rate of 0.3 Å/pulse for TiN and ZrN and for 0.25 Å/pulse for MgO with a base pressure of approximately 10^{-7} Torr and deposition temperature ranging from room temperature up to 700 ^{o}C in order to achieved the desired grain sizes. Prior to film deposition, Si (0 0 1) substrates were cleaned in acetone

and methanol followed by etching in buffered hydrofluoric acid to remove native silicon oxide layer on surface.

For sample 1 and 2, a TiN seed layer of about 100 nm was first deposited on silicon substrate to grow epitaxial cubic TiN/MgO nanolayers. A 400 nm of MgO was grown on the TiN seed layer as Sample 1 as shown in Fig. 19 (a), while Sample 2 consists of 40 nm of TiN or MgO grown alternatively on the TiN seed layer as shown in Fig. 19 (b). Sample 3 consists of ZrN/MgO multilayers with different MgO layer thicknesses, *i.e.* 20 nm, 40 nm, and 130 nm, while keeping the ZrN 10 nm as in Fig. 19 (c). The total thickness was controlled to be 500 nm including the TiN seed layer for all sets. The samples were then irradiated at room temperature with Kr^{2+} ions to a fluence up to 1.56×10^{15} cm^{-2} at 1 MeV at Argonne National Lab. Microstructural evolution was characterized by high resolution TEM (HRTEM) using a JEOL 2010 analytical electron microscope with a point-to-point resolution of 0.23 nm and an accelerating voltage of 200 kV. All TEM samples were prepared under the same conditions (including a final ion polishing step with 3 keV Ar^{+} beam for less than 1 h). Ion milling damage induced by the TEM sample preparation is minimal as seen from the minimal amorphous edge from the TEM sample and the amount of damage is comparable in all the samples.

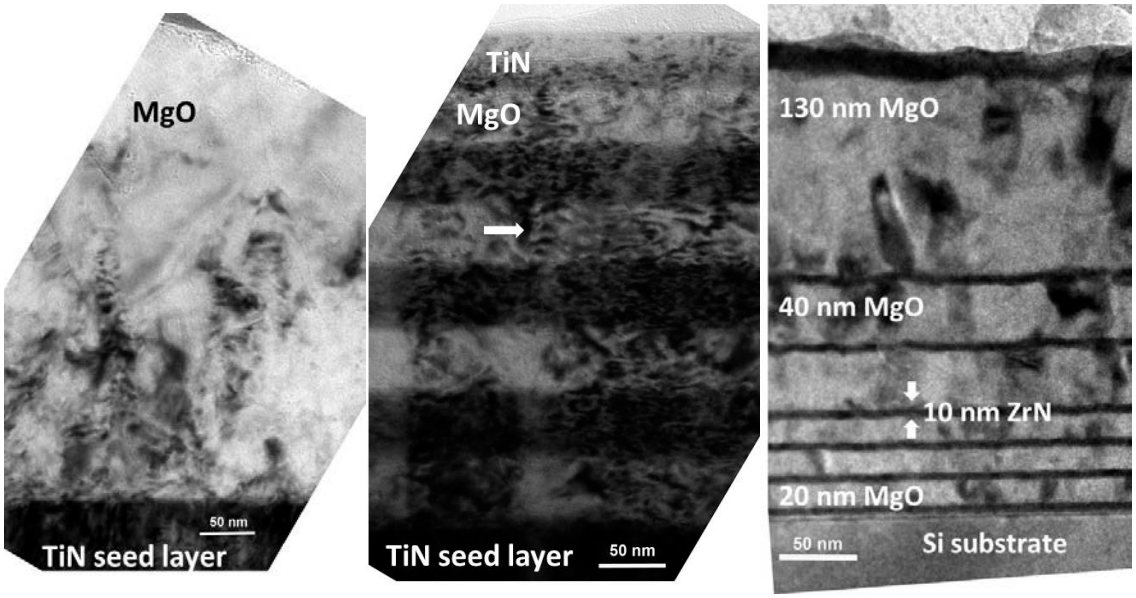

(a) (b) (c)

Figure 19 (a) Epitaxial MgO on TiN, (b) epitaxial MgO/TiN multilayers with layer thickness of about 40 nm, (c) polycrystalline MgO/ZrN multilayer samples with MgO of 20 nm, 40 nm, and 130 nm while ZrN is 10 nm, the terminating layer is ZrN of about 20 nm.

5.4 Results and Discussion

5.4.1 Defects Evolution and Removal by Interface in the Epitaxial MgO Layers

In sample 2 as shown in Fig 19 (b), there is a high density of horizontal pre-existing defects, likely being introduced by the deposition process. Under the irradiation, these pre-existing defects were quickly annihilated by interfaces with TiN, and vacancies in the interior of the films. The pre-existing defects lie on the {100} planes, and glide with a <100> burger's vector towards interfaces. As discussed in Chapter III, the misfit dislocation on the TiN/MgO interfaces act as defect sinks, those unstable pre-existing

defects frozen by the deposition were activated by the energy deposited by the irradiation, and quickly move to the nearby defects sinks, either towards the interfaces or the vacancies in the film. As shown in Fig. 20. Though the defects have aligned on the {100} planes, the moving was not always on the same rate. It is surprising that the mobility of these pre-existing defects is high under the low irradiation dose, 0.001 dpa. The mobility is 1.5 nm/s. The movement was also seen towards the other interfaces on an opposite direction as shown in Fig. 20, the mobility is ~ 1.1 nm/s. The defects mobility decreases rapidly as the unstable amount of pre-existing defects quickly annihilated.

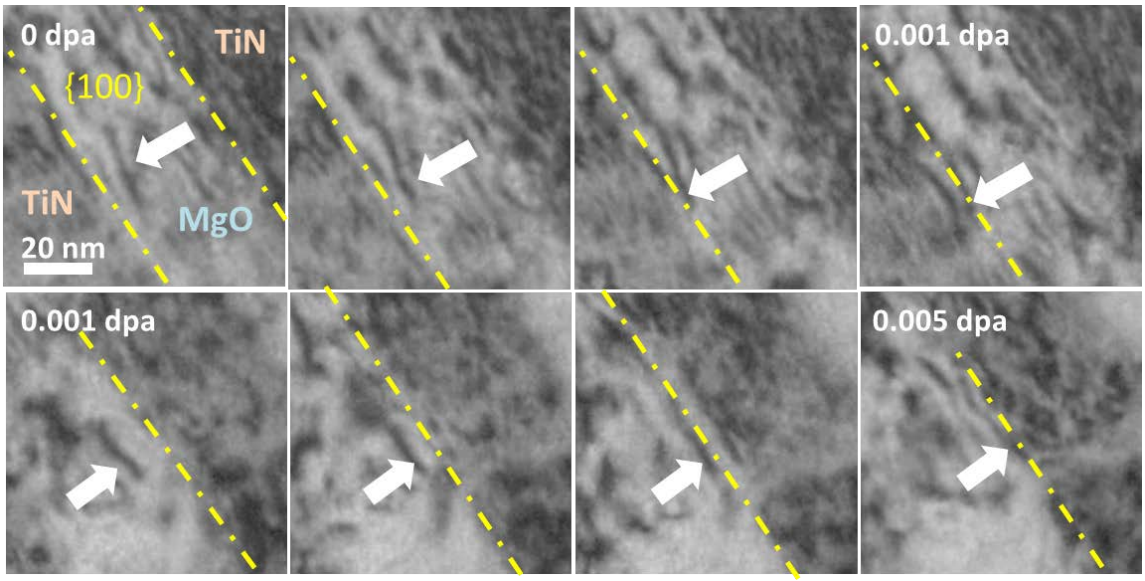

Figure 20 Pre-existing defects moving towards MgO/TiN epitaxial layer interfaces

The pre-existing defects were quickly removed by either interfaces or opposite defects in the film. As shown in Fig. 21 (a), most of the pre-existing defects were

removed around 0.016 dpa. At the same time, the radiation induced defects grow and develop. The radiation induced defects accumulate steadily after all the pre-existing defects were removed. And the defects induced by radiation were found to be relatively stable, with a mobility of around 0.3 nm/s towards the epitaxial MgO/TiN interfaces. As discussed in Chapter III that those defects are interstitial defect clusters as shown in Fig. 21 (b). The major difference from the pre-existing defects is the alignment of defects is along {110} planes, as it's the primary slip planes in NaCl crystal structure, with increasing the fluence, some of the aligned defects grow into clusters with greater diameters. In the last, a high density of defect clusters can be identified, while at the same dose, the single layer MgO sample was amorphized, as shown in Fig. 22. The mechanism is likely attributed to the strain from the TiN layers in the multilayer MgO/TiN, which increase the energy barrier for MgO in the multilayer to be amorphized, the similar mechanism was reported in Fe/Y_2O_3 before [106].

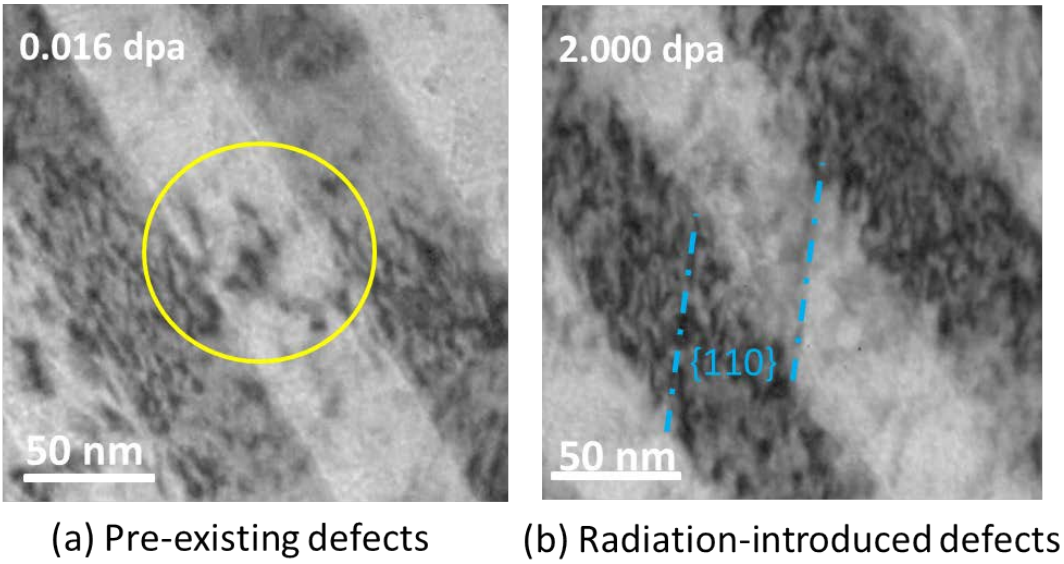

Figure 21 Low density of pre-existing defects remained at 0.016 dpa as in (a), the radiation induced defects start to accumulate as shown in (b).

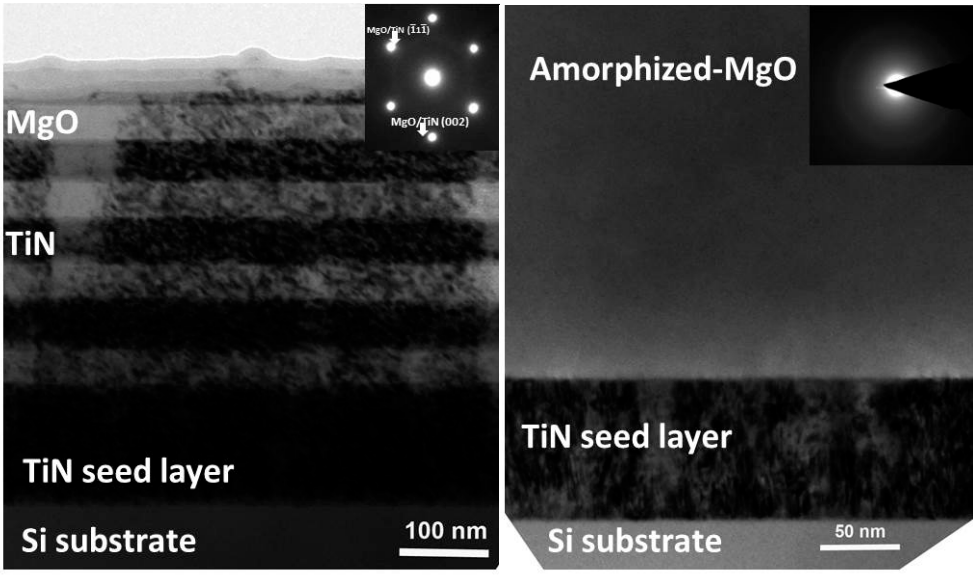

Figure 22 At the end of irradiation up to 0.64 dpa, the comparison between multilayer MgO/TiN (a), and the single layer MgO on TiN seed layer (b). A high density was observed in the multilayer, while single layer MgO was amorphized.

5.4.2 Cyclic Accumulation and Removal of Irradiation Introduced Damage in Polycrystalline MgO

High angle grain boundaries of MgO removes defects effectively via cyclic removal of radiation induced defects. The defects were first initiated around grain boundaries, since the formation energy of point defects are low due to the loose bonding on the grain boundaries. And then defects accumulate inside the grains, finally take up the whole interior of grain. It's surprising to see that, when the accumulation reached the maximum, the removal of defects was activated as shown in the Fig. 23. The mechanism can be explained in two folds: (a) the mutual influence between grain boundaries and defects, (b) the mobility change dependence on the evolution of defect clusters.

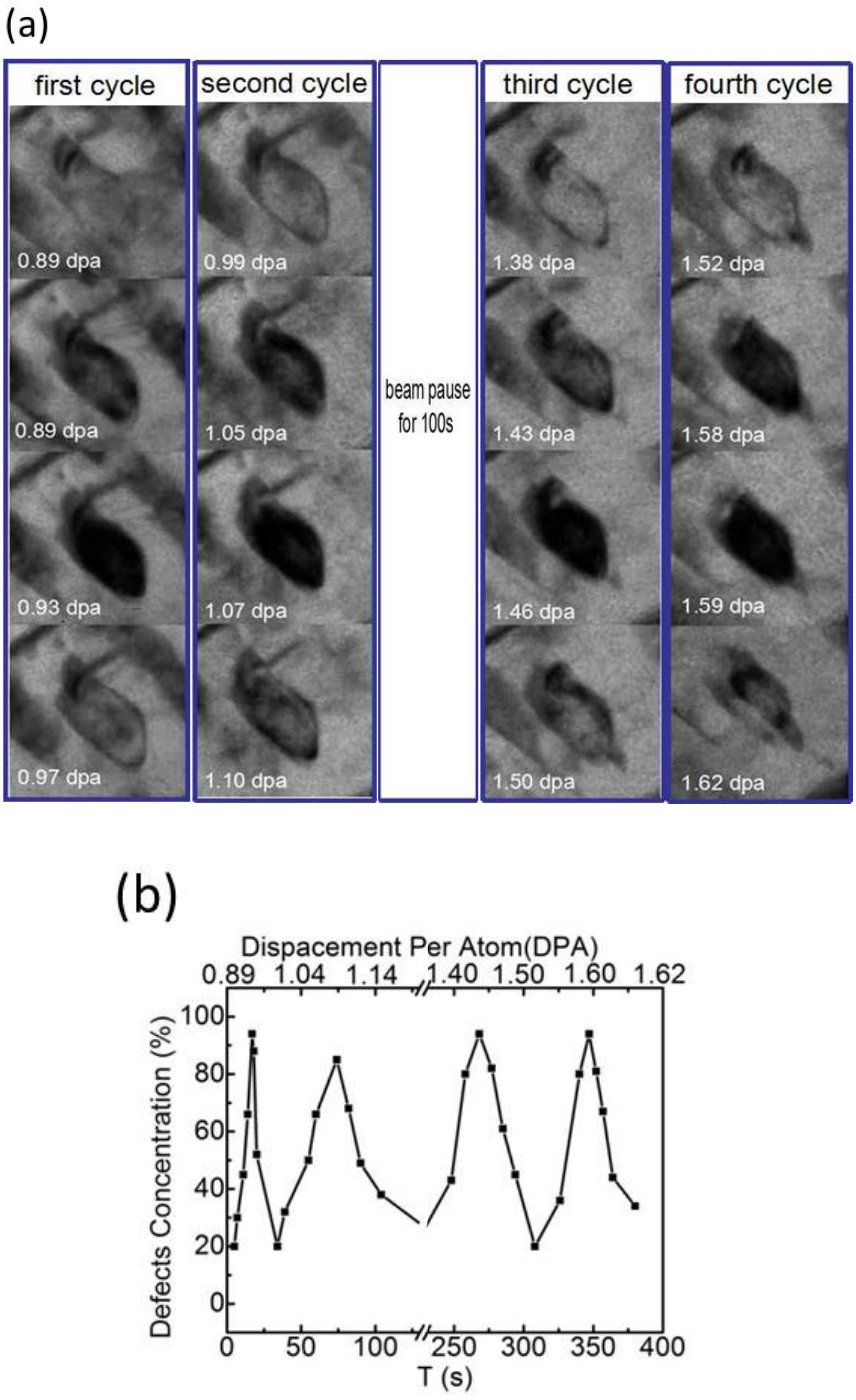

Figure 23 (a) Snapchat of cyclic accumulation and removal of defect clusters in polycrystalline MgO, (b) Illustration of defect concentration with time and dpa in the polycrystalline MgO.

On one hand, the evolution of grain boundaries is one factor in determining the cyclic behavior. With the damage accumulated in the grain boundaries, the formation energy for point defects is also changing, that at a typical point, the accumulation of defects would be reversed to removal of defects. More specifically, when grain boundaries were loaded with interstitials, the formation energy of vacancies on the grain boundaries is further reduced. And vacancies relatively far from the grain-boundary could be annihilated with the interstitials on the grain boundaries. These mechanism is called the interstitials-reemitting mechanism, was firstly reported in a simulation work on Cu. Moreover, vacancies close to grain boundaries have higher mobility, which can become mobile, given the fact that vacancies in MgO are considered immobile at room temperature.

The long-time evolution of irradiation damage in MgO has been obtained by a variety of simulation methods [66]. It is concluded that point defects and small defect clusters were formed under low energy, on the order of 1 keV, collision cascades, while over long times, interstitials annihilate with vacancies and aggregate with other interstitials to form large clusters. And a type of cluster consists of six atoms was found to have extremely high mobility. For example the diffusion barrier for isolated Mg interstitial is 0.32 eV, and 0.40 eV for O interstitials, the trend was found that the mobility decreases with increasing the size of clusters. However, a hexa-interstitial has an extremely low diffusion barrier even lower than half of that of the isolated interstitials. The cyclic movement could be explained that the diffusivity of interstitials is highly influenced by the evolution of defects. In the beginning, interstitials formed preferred at

the grain boundaries, due to the lower formation energy because of the loose bounds there, and when boundaries are damaged, it further reduces the formation energy for point defect. For example, when an O vacancy is created, the coordinated Mg atoms would be easier to displace from their original sites by irradiation collision. Therefore, the damage starts from the grain boundaries, and always accumulates or propagates from the front edge of the defective zoon, which caused the lattice distortion and forming the dark contrast under TEM. During the process of accumulation of point defects, the defective zoon occupies the whole interior of grains, and defects evolve at the same time, clusters with more interstitials formed. The mobility decreases with the size of clusters increase and finally become immobile, such as the tetra-interstitial clusters. They might initiate the interstitial loops there, however when clusters grow to a certain point, for example the hexa-interstitial cluster, the mobility maybe be improved significantly, that the immobile defects becomes mobile again, and therefore they tend to move to the closest defect sinks and annihilated there. It is worth noting that, some clusters may stop at the immobile status, and forming extended clusters or even loops locally, which explains at the last part, defect clusters were observed inside grains. In the case of the hexa-interstitials and octa-interstitials, the long range one dimensional diffusion along <110> in their metastable states could result in an experimentally detectable signature.

At the same time, the MgO grains undergoes lattice restoration via radiation induced diffusivity, and damaged grain boundaries were activated by loaded defects and latter drove defects back and annihilated there, latter resulting in grain growth. The diffusion of clusters towards grain boundaries assist the grain growth in the way that

they reside at a lower energy sites with the neighboring grains along their orientation which results in grain growth, as shown in Fig. 24 below. The grain growth is more obvious in the larger grains in 130 nm MgO layer.

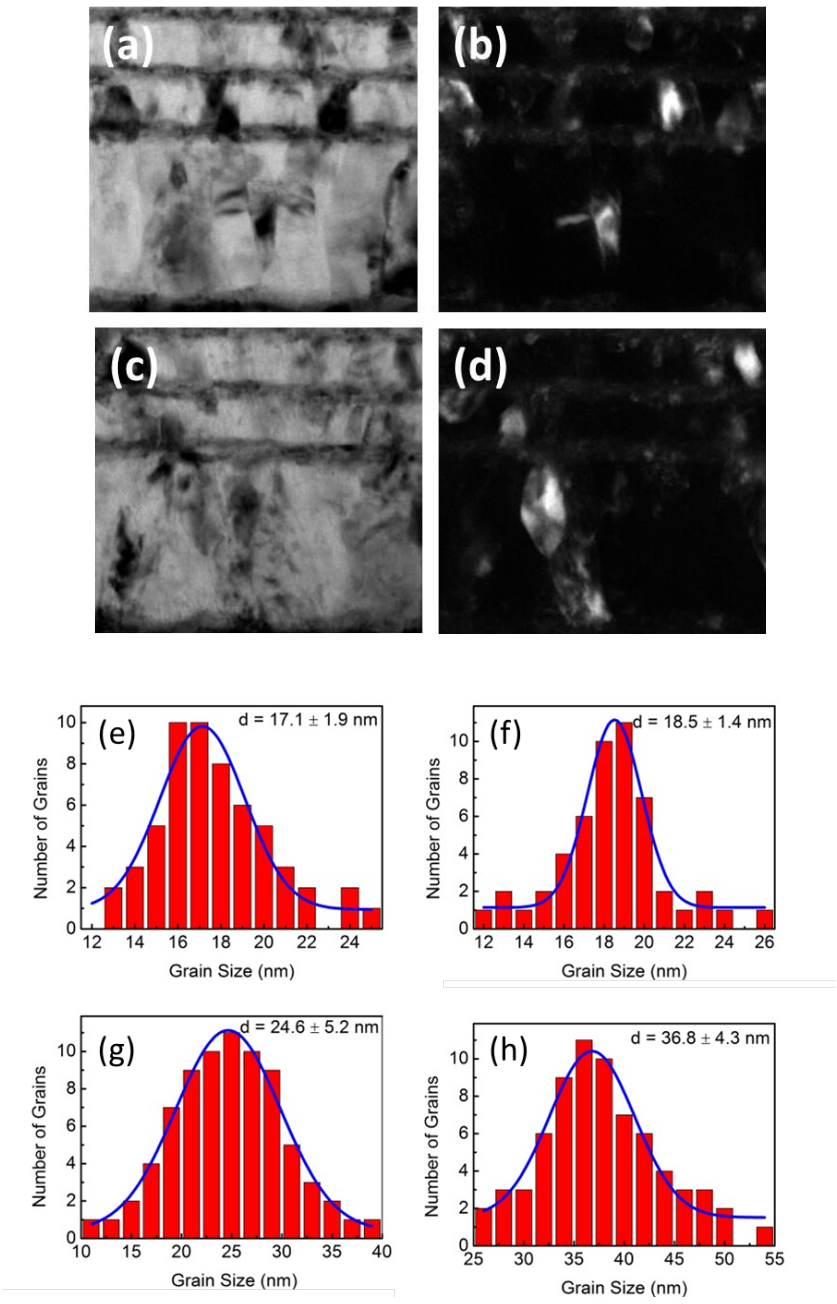

Figure 24 Grain growth before and after irradiation, (a) bright field TEM image of MgO multilayers before irradiation, (b) dark field image of the MgO multilayer before irradiation, (c) Bright field image of the same sample before irradiation, (d) Dark-field image of the MgO multilayer after irradiation, (e) MgO grain size in the thin layer before irradiation, (f) MgO grain size in the thin layer after irradiation, (g) MgO grain size in the thick layer before irradiation, (h) MgO grain size in the thick layer after irradiation.

5.5 Conclusion

The in-situ irradiation experiments on MgO based thin films revealed that, after a 1 MeV Kr^{2+} ion irradiation to a fluence of 1.56×10^{15} cm^{-2}, single layer MgO was amorphized, while epitaxial MgO/TiN remains crystallinity, with a high defects density observed. The defects irradiation induced defects in MgO/TiN case has a low mobility, and the defect density and size grow with irradiation dose. As comparison, in a polycrystalline MgO multilayer with thin ZrN film, high mobility of irradiation induced defects was observed. The initiated from grain boundaries and interfaces, and eventually annihilated in the grain boundaries and interfaces as defect sinks. Several clear cyclic defects accumulation and removal was identified. The surprising in-situ self-healing effects were firstly reported in this study.

REFERENCES

1. Lengauer, W., et al., *Solid state properties of group IVb carbonitrides.* Journal of Alloys and Compounds, 1995. **217**(1): p. 137-147.

2. Egeland, G.W., *Radiation damage and fission product release in zirconium nitride*, in *Materials and Metallurgical Engineering*. 2005, New Mexico Institute of Mining and Technology.

3. Sze, S.M., *Semiconductor devices, physics and technology*. 1985: Wiley.

4. Smith, B., *Ion implantation range data for silicon and germanium device technologies*. 1977: Research Studies Press.

5. Was, G.S., *Fundamentals of radiation materials science: metals and alloys*. 2007: Springer Berlin Heidelberg.

6. Kinchin, G.H. and R.S. Pease, *The displacement of atoms in solids by radiation.* Reports on Progress in Physics, 1955. **18**(1): p. 1.

7. Ziegler, J.F., M.D. Ziegler, and J.P. Biersack, *SRIM - The stopping and range of ions in matter (2010).* Nuclear Instruments and Methods in Physics Research, Section B: Beam Interactions with Materials and Atoms, 2010. **268**(11-12): p. 1818-1823.

8. Hocking, W.H., R.A. Verrall, and I.J. Muir, *Migration behaviour of iodine in nuclear fuel.* Journal of Nuclear Materials, 2001. **294**(1–2): p. 45-52.

9. Zhang, H.-R., R. Egerton, and M. Malac, *Electron irradiation damage and color centers of MgO nanocube.* Nuclear Instruments and Methods in Physics Research Section B: Beam Interactions with Materials and Atoms, 2013. **316**(0): p. 137-143.

10. Tan, C.Y., et al., *Sintering and mechanical properties of MgO-doped nanocrystalline hydroxyapatite.* Ceramics International, 2013. **39**(8): p. 8979-8983.

11. Petti, D., et al., *Chemical and electronic properties of Fe/MgO/Ge heterostructures for spin electronics.* Journal of Physics: Conference Series, 2011. **292**(1): p. 012010.

12. Parkin, S.S.P., et al., *Giant tunnelling magnetoresistance at room temperature with MgO (100) tunnel barriers.* Nat Mater, 2004. **3**(12): p. 862-867.

13. Monsma, D.J. and S.S.P. Parkin, *Spin polarization of tunneling current from ferromagnet/Al2O3 interfaces using copper-doped aluminum superconducting films.* Applied Physics Letters, 2000. **77**(5): p. 720-722.

14. Ikeda, S., et al., *Tunnel magnetoresistance of 604% at 300K by suppression of Ta diffusion in CoFeB ／MgO ／CoFeB pseudo-spin-valves annealed at high temperature.* Applied Physics Letters, 2008. **93**(8): p. 082508.

15. Dexin, W., et al., *70% TMR at room temperature for SDT sandwich junctions with CoFeB as free and reference Layers.* Magnetics, IEEE Transactions on, 2004. **40**(4): p. 2269-2271.

16. Zinkle, S.J. and C. Kinoshita, *Defect production in ceramics.* Journal of Nuclear Materials, 1997. **251**: p. 200-217.

17. Neeft, E.A.C., et al., *The EFTTRA-T3 irradiation experiment on inert matrix fuels.* Journal of Nuclear Materials, 2003. **320**(1–2): p. 106-116.

18. Croixmarie, Y., et al., *Fabrication of transmutation fuels and targets: the ECRIX and CAMIX-COCHIX experience.* Journal of Nuclear Materials, 2003. **320**(1–2): p. 11-17.

19. Chauvin, N., et al., *In-pile studies of inert matrices with emphasis on magnesia and magnesium aluminate spinel.* Journal of Nuclear Materials, 1999. **274**(1–2): p. 91-97.

20. Hough, A. and J.A.C. Marples, *The pseudo binary phase diagrams of PuO2 with alumina, beryllia and magnesia and the pseudo ternary PuO2-ThO2-BeO.* Journal of Nuclear Materials, 1965. **15**(4): p. 298-309.

21. Zhang, H., et al., *Melting behaviour of oxide systems for heterogeneous transmutation of actinides. I. The systems Pu Al O and Pu Mg O.* Journal of Nuclear Materials, 1997. **249**(2 – 3): p. 223-230.

22. Sugisaki, M., et al., *Phase equilibrium of UO_{2-x}-MgO system.* Journal of Nuclear Science and Technology, 1973. **10**(6): p. 387-389.

23. Epstein, L.F. and W.H. Howland, *Binary mixtures of UO2 and other oxides.* Journal of the American Ceramic Society, 1953. **36**(10): p. 334-335.

24. Medvedev, P.G., et al., *Dual phase MgO–ZrO2 ceramics for use in LWR inert matrix fuel.* Journal of Nuclear Materials, 2005. **342**(1–3): p. 48-62.

25. Economos, G., *Behavior of refractory oxides in contact with metals at high temperatures.* Industrial & Engineering Chemistry, 1953. **45**(2): p. 458-459.

26. Tolksdorf, E. and E. Tolksdorf, *Corrosion behaviour of new Zr alloys.* Journal of Nuclear Materials, 1974. **51**(3): p. 330-336.

27. Livey, D.T. and P. Murray, *The stability of beryllia and magnesia in different atmospheres at high temperatures.* Journal of Nuclear Energy (1954), 1956. **2**(3–4): p. 202-212.

28. Abriou, D. and J. Jupille, *Self-inhibition of water dissociation on magnesium oxide surfaces.* Surface Science, 1999. **430**(1–3): p. L527-L532.

29. Kurina, I.S., A.M. Dvoryashin, and L.S. Gudkov, *Production and investigation of thorium-containing fuel compositions.* Atomic Energy, 2000. **88**(5): p. 362-367.

30. Kleykamp, H., *Selection of materials as diluents for burning of plutonium fuels in nuclear reactors.* Journal of Nuclear Materials, 1999. **275**(1): p. 1-11.

31. Kramer, D.A., *Magnesium compounds*, in *Kirk-Othmer Encyclopedia of Chemical Technology*. 2000, John Wiley & Sons, Inc.

32. Dawihl, W., *Transition metal carbides and nitrides.* Angewandte Chemie, 1972. **84**(19): p. 960-960.

33. Chase, M.W., S. National Institute of, and Technology, *NIST-JANAF thermochemical tables*. 1998, [Washington, D.C.]; Woodbury, N.Y.: American Chemical Society ; American Institute of Physics for the National Institute of Standards and Technology.

34. Medvedev, P., *Development of dual phase magnesia-zirconia ceramics for light water reactor inert matrix fuel*, in *Nuclear Engineering*. 2004, Texas A&M University: Texas A&M University.

35. Kroschwitz, J.I., *Kirk-Othmer Encyclopedia of Chemical Technology*. 2007: J. Wiley.

36. Soga, N. and O.L. Anderson†, *High-temperature elastic properties of polycrystalline MgO and Al2O3.* Journal of the American Ceramic Society, 1966. **49**(7): p. 355-359.

37. Rust, J.H., *Nuclear power plant engineering*. 1979: Haralson Publishing Company.

38. Nishida, A., T. Shimamura, and Y. Kohtoku, *Effect of grain size on mechanical properties of high-purity polycrystalline magnesia.* Journal of the Ceramic Society of Japan, 1990. **98**(1136): p. 412-415.

39. Evans, A.G., D. Gilling, and R.W. Davidge, *The temperature-dependence of the strength of polycrystalline MgO.* Journal of Materials Science, 1970. **5**(3): p. 187-197.

40. Evans, A.G. and R.W. Davidge, *The strength and fracture of stoichiometric polycrystalline UO2.* Journal of Nuclear Materials, 1969. **33**(3): p. 249-260.

41. Wick, O.J., *Plutonium handbook: a guide to the technology*. 1967: Gordon and Breach.

42. Park, B., W.J. Weber, and L.R. Corrales, *Molecular dynamics study of the threshold displacement energy in MgO.* Nuclear Instruments and Methods in Physics Research Section B: Beam Interactions with Materials and Atoms, 2000. **166–167**(0): p. 357-363.

43. Groves, G.W. and A. Kelly, *Neutron damage in MgO.* Philosophical magazine, 1963. **8**(93): p. 1437-1454.

44. Henderson, B., et al., *Radiation damage in magnesium oxide. II. Effect of pre-irradiation annealing in hydrogen.* Journal of Physics C: Solid State Physics, 1971. **4**(12): p. 1496.

45. Clinard Jr, F.W., G.F. Hurley, and L.W. Hobbs, *Neutron irradiation damage in MgO, Al2O3 and MgAl2O4 ceramics.* Journal of Nuclear Materials, 1982. **108–109**(0): p. 655-670.

46. Stevanovic, M. and J. Elston, *Effect of fast neutron irradiation on sintered alumina and magnesia.* Proc. Brit. Ceram. Soc., 1967. **7**(423-38): p. Medium: X.

47. Morgan, C.S. and D.H. Bowen, *Inert gas bubbles in neutron-irradiated magnesium oxide.* Philosophical Magazine, 1967. **16**(139): p. 165-180.

48. Wilks, R.S., *Gas formation by transmutation of MgO and A12O3.* Journal of Nuclear Materials, 1966. **19**(3): p. 351-353.

49. Duderstadt, J.J. and L.J. Hamilton, *Nuclear reactor analysis*. 1976: Wiley.

50. Wilks, R.S., *Neutron-induced damage in BeO, Al2O3 and MgO — a review.* Journal of Nuclear Materials, 1968. **26**(2): p. 137-173.

51. Cáceres, D., et al., *Nanoindentation on neutron irradiated MgO crystals.* Nuclear Instruments and Methods in Physics Research Section B: Beam Interactions with Materials and Atoms, 2002. **191**(1–4): p. 178-180.

52. Sambell, R.A.J. and R. Bradley, *The strength of irradiated magnesium oxide.* Philosophical Magazine, 1964. **9**(97): p. 161-166.

53. Davidge, R.W., *Irradiation damage and irradiation hardening in single crystal MgO after low neutron doses < 1018 nvt (>1 MeV).* Journal of Nuclear Materials, 1968. **25**(1): p. 75-86.

54. Elleman, T.S., R.B. Price, and D.N. Sunderman, *Fission fragment induced expansion in ceramic materials.* Journal of Nuclear Materials, 1965. **15**(3): p. 164-178.

55. Beauvy, M., et al., *Actinide transmutation: new investigation on some actinide compounds.* Journal of Alloys and Compounds, 1998. **271–273**(0): p. 557-562.

56. Treilleux, M., et al., *Observation of implantated potassium aggregates in MgO single crystals.* Physica Status Solidi (A) Applied Research, 1978. **48**(2): p. 425-430.

57. Perez, A., et al., *Spinel ferrite formation in iron implanted MgO crystals.* Nuclear Instruments and Methods. **182–183, Part 2**(0): p. 747-751.

58. Burnett, P.J. and T.F. Page, *Chemomechanical effect in ion-implanted magnesium oxide.* Journal of Materials Science Letters, 1985. **4**(11): p. 1364-1370.

59. Aoki, Y., et al., *Vickers hardness measurement of ion implanted MgO.* Nuclear Instruments and Methods in Physics Research Section B: Beam Interactions with Materials and Atoms, 1994. **91**(1–4): p. 247-251.

60. Horton, L.L., J. Bentley, and M.B. Lewis, *Radiation damage in ion-irradiated MgO.* Nuclear Instruments and Methods in Physics Research Section B: Beam Interactions with Materials and Atoms, 1986. **16**(2–3): p. 221-229.

61. Zinkle, S.J., *Microstructure of ion irradiated ceramic insulators.* Nuclear Instruments and Methods in Physics Research Section B: Beam Interactions with Materials and Atoms, 1994. **91**(1–4): p. 234-246.

62. Zinkle, S.J. and L.L. Snead, *Influence of irradiation spectrum and implanted ions on the amorphization of ceramics,* in *Nuclear Instruments and Methods in Physics Research Section B: Beam Interactions with Materials and Atoms*. 1996. p. 92-101.

63. Sonoda, T., et al., *Formation and growth process of defect clusters in magnesia under ion irradiation.* Nuclear Instruments and Methods in Physics Research

Section B: Beam Interactions with Materials and Atoms, 1997. **127–128**(0): p. 176-180.

64. Uberuaga, B.P., et al., *Dynamical simulations of radiation damage and defect mobility in MgO.* Physical Review B, 2005. **71**(10): p. 104102.

65. Popov, A.I., et al., *Dynamics of F-center annihilation in thermochemically reduced MgO single crystals.* Solid State Communications, 2001. **118**(3): p. 163-167.

66. Uberuaga, B.P., et al., *Exploring long-time response to radiation damage in MgO.* Nuclear Instruments and Methods in Physics Research Section B: Beam Interactions with Materials and Atoms, 2005. **228**(1–4): p. 260-273.

67. Uberuaga, B.P., et al., *Point defect–grain boundary interactions in MgO: an atomistic study.* Journal of Physics: Condensed Matter, 2013. **25**(35): p. 355001.

68. Burghartz, M., et al., *Some aspects of the use of ZrN as an inert matrix for actinide fuels.* Journal of Nuclear Materials, 2001. **288**(2–3): p. 233-236.

69. Streit, M., et al., *Zirconium nitride as inert matrix for fast systems.* Journal of Nuclear Materials, 2003. **319**(0): p. 51-58.

70. Adachi, J., et al., *Thermal and electrical properties of zirconium nitride.* Journal of Alloys and Compounds, 2005. **399**(1): p. 242-244.

71. Baker, T., *The coefficient of thermal expansion of zirconium nitride.* Acta Crystallographica, 1958. **11**(4): p. 300.

72. Odén, M., H. Ljungcrantz, and L. Hultman, *Characterization of the induced plastic zone in a single crystal TiN(001) film by nanoindentation and transmission electron microscopy.* Journal of Materials Research, 1997. **12**(08): p. 2134-2142.

73. Li, P. and J.M. Howe, *Dislocation reactions in ZrN.* Acta Materialia, 2002. **50**(17): p. 4231-4239.

74. Kim, Y.S. and G.L. Hofman, *AAA fuels handbook*, in *Other Information: PBD: 27 Mar 2003*. 2003. p. Medium: ED; Size: 215 pages.

75. Kubaschewski, O., C.B. Alcock, and P.J. Spencer, *Materials thermochemistry*. 1993: Pergamon Press.

76. Arai, Y., et al., *Dependence of the thermal conductivity of (U, Pu) N on porosity and plutonium content.* Journal of Nuclear Materials, 1992. **195**(1–2): p. 37-43.

77. Gao, F., H.Y. Xiao, and W.J. Weber, *Ab initio molecular dynamics simulations of low energy recoil events in ceramics.* Nuclear Instruments and Methods in Physics Research Section B: Beam Interactions with Materials and Atoms, 2011. **269**(14): p. 1693-1697.

78. Yang, Y., C.A. Dickerson, and T.R. Allen, *Radiation stability of ZrN under 2.6 MeV proton irradiation.* Journal of Nuclear Materials, 2009. **392**(2): p. 200-205.

79. Janse van Vuuren, A., et al., *The effect of He and swift heavy ions on nanocrystalline zirconium nitride.* Nuclear Instruments and Methods in Physics Research Section B: Beam Interactions with Materials and Atoms, 2014. **326**(0): p. 19-22.

80. Egeland, G.W., et al., *Heavy-ion irradiation defect accumulation in ZrN characterized by TEM, GIXRD, nanoindentation, and helium desorption.* Journal of Nuclear Materials, 2013. **435**(1–3): p. 77-87.

81. Lu, F.Y., et al., *Displacive radiation-induced structural contraction in nanocrystalline ZrN.* Applied Physics Letters, 2012. **101**(4): p. 041904-4.

82. Perry, A.J., et al., *Residual stress and the effect of implanted argon in films of zirconium nitride made by physical vapor deposition.* Journal of Vacuum Science & Technology A, 1992. **10**(4): p. 1446-1452.

83. Janse van Vuuren, A., et al., *Radiation tolerance of nanostructured ZrN coatings against swift heavy ion irradiation.* Journal of Nuclear Materials, 2013. **442**(1-3): p. 507-511.

84. Zanghi, D., et al., *Structural characterization of ZrN implanted with high Co fluences.* Nuclear Instruments and Methods in Physics Research Section B: Beam Interactions with Materials and Atoms, 1999. **155**(4): p. 416-425.

85. Lackner, J.M., et al., *Structural, mechanical and tribological investigations of pulsed laser deposited titanium nitride coatings.* Thin Solid Films, 2004. **453–454**(0): p. 195-202.

86. Ferro, D., et al., *Pulsed laser deposited hard TiC, ZrC, HfC and TaC films on titanium: Hardness and an energy-dispersive X-ray diffraction study.* Surface and Coatings Technology, 2008. **202**(8): p. 1455-1461.

87. Craciun, V., D. Cracium, and I.W. Boyd, *Reactive pulsed laser deposition of thin TiN films.* Materials Science and Engineering: B, 1993. **18**(2): p. 178-180.

88. Willmott, P.R. and H. Spillmann, *Materials by design—exploiting the unique properties of pulsed laser deposition for the synthesis of novel hard materials and structures.* Applied Surface Science, 2002. **197–198**(0): p. 432-437.

89. Craciun, D., et al., *Thin and hard ZrC/TiN multilayers grown by pulsed laser deposition.* Surface and Coatings Technology, 2011. **205**(23–24): p. 5493-5496.

90. Craciun, D., et al., *Very hard TiN thin films grown by pulsed laser deposition.* Applied Surface Science, 2012. **260**(0): p. 2-6.

91. Rose, M., A.G. Balogh, and H. Hahn, *Instability of irradiation induced defects in nanostructured materials.* Nuclear Instruments and Methods in Physics Research Section B: Beam Interactions with Materials and Atoms, 1997. **127–128**(0): p. 119-122.

92. Ghosh, S., et al., *In situ monitoring of electrical resistance of nanoferrite thin film irradiated by 190 MeV Au14+ ions.* Nuclear Instruments and Methods in Physics Research Section B: Beam Interactions with Materials and Atoms, 2003. **212**(0): p. 510-515.

93. Wang, H., et al., *Ion irradiation effects in nanocrystalline TiN coatings.* Nuclear Instruments & Methods in Physics Research Section B-Beam Interactions with Materials and Atoms, 2007. **261**(1-2): p. 1162-1166.

94. Perry, A.J. and D.E. Geist, *On the residual stress profile developed in titanium nitride by ion implantation.* Nuclear Instruments and Methods in Physics Research Section B: Beam Interactions with Materials and Atoms, 1997. **127–128**(0): p. 967-971.

95. Perry, A.J., et al., *The smoothness, hardness and stress in titanium nitride following argon gas cluster ion beam treatment.* Surface and Coatings Technology, 2001. **140**(2): p. 99-108.

96. Perry, A.J., et al., *Effects of metal ion post-implantation on the near surface properties of TiN deposited by CVD.* Surface and Coatings Technology, 2000. **133-134**: p. 203-207.

97. Perry, A.J., et al., *On the residual stress and picostructure of titanium nitride films I: Implantation with argon or krypton.* Surface and Coatings Technology, 1992. **54–55, Part 1**(0): p. 180-185.

98. Bai, X.-M., et al., *Efficient annealing of radiation damage near grain boundaries via interstitial emission.* Science, 2010. **327**(5973): p. 1631-1634.

99. Han, W.Z., et al., *Effect of grain boundary character on sink efficiency.* Acta Materialia, 2012. **60**(18): p. 6341-6351.

100. Sun, C., et al., *In situ evidence of defect cluster absorption by grain boundaries in Kr ion irradiated nanocrystalline Ni.* Metallurgical and Materials Transactions A, 2013. **44**(4): p. 1966-1974.

101. Sun, C., et al., *In situ neutron diffraction study on temperature dependent deformation mechanisms of ultrafine grained austenitic Fe–14Cr–16Ni alloy.* International Journal of Plasticity, 2014. **53**(0): p. 125-134.

102. Yu, K.Y., et al., *Radiation damage in helium ion irradiated nanocrystalline Fe.* Journal of Nuclear Materials, 2012. **425**(1–3): p. 140-146.

103. Yu, K.Y., et al., *Superior tolerance of Ag/Ni multilayers against Kr ion irradiation: an in situ study.* Philosophical Magazine, 2013. **93**(26): p. 3547-3562.

104. Fu, E.G., et al., *Fluence-dependent radiation damage in helium (He) ion-irradiated Cu/V multilayers.* Philosophical Magazine, 2012. **93**(8): p. 883-898.

105. Zhang, X., et al., *Design of radiation tolerant nanostructured metallic multilayers.* Journal of Engineering Materials and Technology, 2012. **134**(4): p. 041010-041010.

106. Chen, Y., et al., *In situ studies of radiation induced crystallization in Fe/a-Y2O3 nanolayers.* Journal of Nuclear Materials, 2014. **452**(1–3): p. 321-327.

107. Jiao, L., et al., *Enhanced ion irradiation tolerance properties in TiN/MgO nanolayer films.* Journal of Nuclear Materials, 2013. **434**(1-3): p. 217-222.

108. Kim, I., et al., *Size-dependent radiation tolerance in ion irradiated TiN/AlN nanolayer films.* Journal of Nuclear Materials, 2013. **441**(1-3): p. 47-53.

109. Townsend, P.D., *Optical effects of ion implantation.* Reports on Progress in Physics, 1987. **50**(5): p. 501.

110. Kishimoto, N., et al., *Dose-rate dependence of negative copper ion implantation into silica glasses and effects on colloid formation.* Nuclear Instruments and Methods in Physics Research Section B: Beam Interactions with Materials and Atoms, 1998. **141**(1–4): p. 299-303.

111. Mignotte, C., et al., *EXAFS studies of thermal annealing effects on the local environment of erbium implanted in LiNbO3.* Nuclear Instruments and Methods

in Physics Research Section B: Beam Interactions with Materials and Atoms, 1996. **120**(1–4): p. 81-83.

112. Lian, J., et al., *In situ TEM of radiation effects in complex ceramics.* Microsc Res Tech, 2009. **72**(3): p. 165-81.

113. Bufford, D., et al., *In situ TEM ion irradiation and implantation effects on Au nanoparticle morphologies.* Chemical Communications, 2014. **50**(57): p. 7593-7596.

114. Fultz, B. and J.M. Howe, *Transmission electron microscopy and diffractometry of materials*. 2012: Springer Berlin Heidelberg.

115. Tench, A.J. and M.J. Duck, *Radiation damage in oxides. I. Defect formation in MgO.* Journal of Physics C: Solid State Physics, 1973. **6**(7): p. 1134.

116. Burnett, P.J. and T.F. Page, *Changing the indentation behaviour of MgO by ion implantation.* MRS Online Proceedings Library, 1983. **27**: p. null-null.

117. Savoini, B., et al., *Optical and mechanical properties of MgO crystals implanted with lithium ions.* Journal of Applied Physics, 2004. **95**(5): p. 2371-2378.

118. White, C.W., et al., *Ion implantation and annealing of crystalline oxides.* Materials Science Reports, 1989. **4**(2): p. 41-146.

119. Chen, Y. and M.M. Abraham, *Evidence for suppression of radiation damage in Li-doped MgO.* Journal of the American Ceramic Society, 1976. **59**(3-4): p. 101-103.

120. Fu, E.G., et al., *Size dependent enhancement of helium ion irradiation tolerance in sputtered Cu/V nanolaminates.* Journal of Nuclear Materials, 2009. **385**(3): p. 629-632.

121. Zhang, X., et al., *Nanostructured Cu/Nb multilayers subjected to helium ion-irradiation.* Nuclear Instruments & Methods in Physics Research Section B-Beam Interactions with Materials and Atoms, 2007. **261**(1-2): p. 1129-1132.

122. Li, N., et al., *He ion irradiation damage in Fe/W nanolayer films.* Journal of Nuclear Materials, 2009. **389**(2): p. 233-238.

123. Li, N., et al., *He ion irradiation damage in Al/Nb multilayers.* Journal of Applied Physics, 2009. **105**(12): p. -.

124. Shen, T.D., *Radiation tolerance in a nanostructure: Is smaller better?* Nuclear Instruments & Methods in Physics Research Section B-Beam Interactions with Materials and Atoms, 2008. **266**(6): p. 921-925.

125. Misra, A., et al., *The radiation damage tolerance of ultra-high strength nanolayered composites.* Jom, 2007. **59**(9): p. 62-65.

126. I. Kim, M.S.M., L. Shao, X. Zhang, J. G. Swadener, Y. Q. Wang and H. Wang, *Suppression of Amorphization in Ion Irradiated TiN/AlN Nanolayer Film.* 2012.

127. Ziegler, J.F., *The stopping powers and ranges of hydrogen and helium ions.* Radiation Effects and Defects in Solids, 1997. **141**(1-4): p. 455-455.

128. Schut, H., et al., *Annealing behaviour of defects in helium implanted MgO.* Nuclear Instruments and Methods in Physics Research, Section B: Beam Interactions with Materials and Atoms, 1999. **147**(1-4): p. 212-215.

129. Hobbs, L.W., *Application of transmission electron microscopy to radiation damage in ceramics.* Journal of the American Ceramic Society, 1979. **62**(5-6): p. 267-278.

130. Norton, M.G., et al., *Transmission-electron microscopy study of ion-beam implanted single-crystal ceramics.* Nuclear Instruments and Methods in Physics Research Section B: Beam Interactions with Materials and Atoms, 1991. **59–60, Part 2**(0): p. 1215-1218.

131. Zinkle, S.J., *Ion irradiation studies of oxide ceramics*. 1988. Medium: ED; Size: Pages: 24.

132. Kinoshita, C., K. Hayashi, and S. Kitajima, *Kinetics of point defects in electron irradiated MgO.* Nuclear Instruments and Methods in Physics Research Section B: Beam Interactions with Materials and Atoms, 1984. **1**(2–3): p. 209-218.

133. van Veen, A., et al., *Nanocavity formation processes in MgO(1 0 0) by light ion (D, He, Li) and heavy ion (Kr, Cu, Au) implantation.* Nuclear Instruments and Methods in Physics Research Section B: Beam Interactions with Materials and Atoms, 2002. **191**(1–4): p. 610-615.

134. Chu, X. and S.A. Barnett, *Model of superlattice yield stress and hardness enhancements.* Journal of Applied Physics, 1995. **77**(9): p. 4403.

135. Misra, A., et al., *The radiation damage tolerance of ultra-high strength nanolayered composites.* JOM Journal of the Minerals, Metals and Materials Society, 2007. **59**(9): p. 62-65.

136. Zhang, R.-Q., et al., *A first-principles study of ultrathin nanofilms of MgO-supported TiN*. Physical Chemistry Chemical Physics, 2012. **14**(7): p. 2462-2467.

137. Zhuo, M.J., et al., *Radiation damage at the coherent anatase interface under Ne ion irradiation.* Journal of Nuclear Materials, 2012. **429**(1–3): p. 177-184.

138. International Atomic Energy, A., *Viability of inert matrix fuel in reducing plutonium amounts in reactors.* 2006.

139. Bai, X.-M., et al., *Role of atomic structure on grain boundary-defect interactions in Cu.* Physical Review B, 2012. **85**(21): p. 214103.

140. Kaoumi, D., A.T. Motta, and R.C. Birtcher, *A thermal spike model of grain growth under irradiation.* Journal of Applied Physics, 2008. **104**(7): p. -.

141. Qi, Z.B., et al., *The inverse Hall–Petch effect in nanocrystalline ZrN coatings.* Surface and Coatings Technology, 2011. **205**(12): p. 3692-3697.

142. Meng, Q.N., et al., *Influence of the residual stress on the nanoindentation-evaluated hardness for zirconiumnitride films.* Surface and Coatings Technology, 2012. **206**(14): p. 3250-3257.

143. Zhang, X., et al., *Thermal stability of sputter-deposited 330 austenitic stainless-steel thin films with nanoscale growth twins.* Applied Physics Letters, 2005. **87**(23): p. -.

144. Zhang, X., et al., *Effects of deposition parameters on residual stresses, hardness and electrical resistivity of nanoscale twinned 330 stainless steel thin films.* Journal of Applied Physics, 2005. **97**(9): p. -.

145. Mayadas, A. and M. Shatzkes, *Electrical-resistivity model for polycrystalline films: the case of arbitrary reflection at external surfaces.* Physical Review B, 1970. **1**(4): p. 1382-1389.

146. Ivanov, O., O. Maradudina, and R. Lyubushkin, *Grain size effect on electrical resistivity of bulk nanograined Bi2Te3 material.* Materials Characterization, 2015. **99**: p. 175-179.

147. Barmak, K., et al., *Surface and grain boundary scattering in nanometric Cu thin films: A quantitative analysis including twin boundaries.* Journal of Vacuum Science and Technology A: Vacuum, Surfaces and Films, 2014. **32**(6).

148. Anderoglu, O., et al., *Significant enhancement of the strength-to-resistivity ratio by nanotwins in epitaxial Cu films.* Journal of Applied Physics, 2009. **106**(2): p. 024313-024313-9.

149. Chawla, J.S., X.Y. Zhang, and D. Gall, *Effective electron mean free path in TiN(001).* Journal of Applied Physics, 2013. **113**(6): p. -.

150. Chen, C.-S., et al., *Influence of the preferred orientation and thickness of zirconium nitride films on the diffusion property in copper.* Journal of Vacuum Science & Technology B: Microelectronics and Nanometer Structures, 2004. **22**(3): p. 1075-1083.